Metal Monolithic Amine-grafted Zeolite for CO_2 Capture

Technical Final Report

Start date:02/21/2007

End date:03/31/2011

Submitted by

Steven S C Chuang

Date report was issued (11/21/2011)

Department of Bio-Molecular and Chemical Engineering
The University of Akron
AKRON-OHIO-44325

1

DISCLAIMER

ABSTRACT

The solid amine sorbent for CO_2 capture process has advantages of simplicity and low operating cost compared to the MEA (monoethanolamine) process. Solid amine sorbents reported so far suffered from either low CO_2 capture capacity or low stability. The solid amine sorbent developed in this project exhibited more than 3.2 mmol/g and degraded less than 10% even after 500 cycles of heating and cooling in absence of steam. The presence of steam further enhanced CO_2 capture capacity. The cost of the sorbent is estimated to be less than $7.00/lb. This sorbent was developed using the results of in situ infrared spectroscopic study. Infrared results showed that CO_2 adsorbs on TEPA (tetraethylenepentamine)/PEG (polyethylene glycol) as carbamates and bicarbonates. The CO_2 adsorption capacity and oxidation resistance of the amine sorbent can be enhanced by the interactions between NH_2 of TEPA molecules with the OH group of PEG molecules. PEG was also found to be effectively disperse and immobilize the aromatic amines for SO_2 adsorption. The infrared study also showed that SiO_2 is a significantly better support than zeolites due to its proper hydrophobicity.

The results of this study led to the development of a high performance solid amine sorbent under simulated gas flow condition in a fixed bed, a fluidized bed, and a metal monolith unit. This study showed heat transfer could become a major technical issue in scaling up a fixed bed adsorber. The use of the fluidized bed and metal monoliths can alleviate the heat transfer issue. The metal monolith could be suitable for small scale applications due to the high cost of manufacturing; the fluidized bed mode would be most suitable for large scale applications. Preliminary economic analysis suggested that the Akron solid amine process would cost 45% less than that of MEA process.

Table of Contents

1   Executive summary

The objective of this project is to develop a highly efficient and low cost CO_2 capture system with solid (i.e., immobilized) amines. The solid amines developed in this project consist of the low cost organic amine, degradation inhibitor, and linker to bind organic amine on the surface of the porous oxides.   The cost of the sorbent is estimated to be less than $7.00/lb; the sorbent exhibited CO_2 capture capacity more than 3.2 mmol/g and degraded less than 10% after more than 500 cycles of heating and cooling in the absence of steam. The performance of this sorbent was further improved in an adsorber with more uniform temperature distribution and in the presence of water vapor in the CO_2 stream. The degraded sorbents can be reactivated with a low cost approach which involves removal of degraded amines and further impregnation of organic amines and binders. Preliminary techno-economic analysis showed that the solid amine CO_2 capture process cost less than 45% of the liquid amine process. The results of this study exceeded target performance set in the proposal.

This project involved basic, applied research, and prototype unit development. The basic research was focused on determining key factors governing the interaction between CO_2 and amine functional group by in situ infrared and mass spectroscopy. In situ infrared spectroscopic results showed that CO_2 adsorbs on TEPA (tetraethylenepentamine)/PEG (polyethylene glycol) as carbamates and bicarbonates. The CO_2 adsorption capacity and oxidation resistance of the TEPA sorbent can be enhanced by the interactions between NH_2 of TEPA molecules with the OH group of PEG molecules. The infrared study also showed that SiO_2 is a significant better support than zeolite due to its proper hydrophobicity. SO_2 is known to irreversibly adsorb on the aliphatic amine such as TEPA and was found to adsorb reversibly on 1,3-phenylenediamine/SiO_2 sorbent in the form of sulphite which disrupts the 1,3-phenylenediamine adsorbate layer on the SiO_2 surface. PEG was found to be effectively disperse and immobilize the aromatic amines during SO_2 adsorption. Both nitric oxide (NO) and hydrogen chloride (HCl) were found to irreversibly adsorb on the solid amine surface. The PEG addition was not effective in preventing the amine site from NO and HCl poisoning.

The results of basic research provided the scientific basis for applied research which involved (i) the fine-tuning our solid amine sorbent capacity and oxidation resistance and (ii) fabrication of sorbent pellets and metal monoliths. These efforts led to the development of durable and attrition resistance pellets for the large scale fluidized bed applications and the metal monoliths for the small applications. The sorbent powder particles and pellets developed were tested in a 5 gram fixed bed unit and a 10 gram fluidized bed unit. The addition of water vapor to the 10%-15% CO_2/air stream flowing through these units was found to increase the CO_2 capture capacity by 40-60%. H_2O could have a positive effect on the CO_2 capture capacity through promoting the formation of bicarbonate species, but excess H_2O could block the pore of the solid amine sorbent, decreasing the overall CO_2 capture capacity. Proper adjustment of the

surface hydrophobicity/hydrophilicity is needed to optimize the CO_2 capture capacity of the solid amine surface in the presence of 4-5% H_2O vapor.

The prototype unit development involves design, construction, and testing. The prototype unit consists of flow control, adsorber, condenser, CO_2 sensor, and computer interface and control, which allow automatic operation. Comparison of the results of fixed, fluidized bed, and metal monolith adsorber testing showed that (i) the major technical barrier in fixed bed is heat transfer, especially the time needed to heat sorbent bed to the desorption temperature and (ii) the metal monolith provides excellent heat transfer with concerns of high cost. The metal monolith could be suitable for small scale applications; the fluidized bed mode would be most suitable for large scale applications. Expanding the metal monolith from small scale to large scale applications requires lowering manufacturing cost of metal monoliths.

Energy needed for regeneration of the sorbent and solvent is the key contributor to the operating cost of the CO_2 capture process. Due to the use of low heat capacity and low CO_2 binding energy of solid amine compared with those of MEA (monoethanol amine), the energy needed for regeneration of solid amine is 45% less than that of MEA. Additional cost reduction of the solid amine process is expected to come from lowering (i) operating cost due to significantly low usage of water and (ii) capital cost due to use low corrosion resistance materials and decrease use of piping and pumps in the process.

2   Introduction

Carbon dioxide capture by solid sorbents is attractive for coal-fired power plants and closed environment applications such as submarines and space stations.[1-2] The solid sorbent CO_2 capture process possesses potential advantage of simplicity and low operating cost. This is because of (i) elimination of recirculation pumps to move the sorbent from one location to another, (ii) minimization of the equipment corrosion resulting liquid amine/ammonium, (iii) significantly lower energy needed for sorbent regeneration. The shortcoming of the present solid sorbent is its low CO_2 capture capacity.

Success Criteria:
(1) Develop an amine-grafted zeolite sorbent capable of capturing at least 1.5 mmol-CO_2/g-sorb. and 1.0 mmol-SO_2/g-sorb.
(2) Achieve sorbent capable of greater than 500 times regeneration with less than 5% performance degradation in terms of CO_2 and SO_2 capture capacity.

The success criteria were met. The results of this study showed that the solid amine CO_2 capture process developed by the University of Akron would cost less than 45% of the liquid amine process.

This project has resulted in the following publications and patent applications.

Publications:

1. 1. "In Situ Infrared Study of the Role of PEG in Stabilizing Silica-supported Amine for CO2 Capture," ChemSusChem, J. Tanthana and S.S. C. Chuang, 3, 957-964, 2010.

2. "Oxide-supported Tetraethylenepentamine for Carbon Dioxide Capture," J. C. Fisher II, J. Tanthana, and S. S. C. Chuang, Environmental Progress & Sust Energy, 28 (4), 589-598, 2009.

Patent Applications and Disclosures:

1. "Amine Absorber for Carbon Dioxide Capture and Processes for Making and Using the Same," UA 685 PCT CN, US, and EP. US Patent application. US 12/741,600

2. "Low Cost Immobilized Amine-Alcohol Sorbents for Sulfur Dioxide Capture," UA 812 PRV Provisional Patent US61/255,1786S

3. "Sulfur and Nitrogen Compound-Resistant Immobilized Amine Sorbents for CO2 capture," UA 815 PRV Provisional Patent US61/255,173.

4. "Low cost methods for fabrication of solid amine pellets," University of Akron patent disclosure. In progress.

3 Experimental methods

  The different solid amine sorbents prepared are screened for CO_2 capture and stability in different methods before it was finally tested in pilot scale. The different testing apparatus used in the project are shown in the flow chart below.

```
                    ┌──────────────────────┐
                    │  CO2 testing apparatus │
                    └──────────────────────┘
```

ATR/DRIFTS–MS (50 mg) Figure 3-1 & 3-2	Tubular reactor (1g) Figure 3-3	Mine Me reactor (5 g) Figure 3-4 & 3-5	Pilot scale (25 kg) Figure 3-6	Radiator monolith reactor Figure 3-7 & 3-8
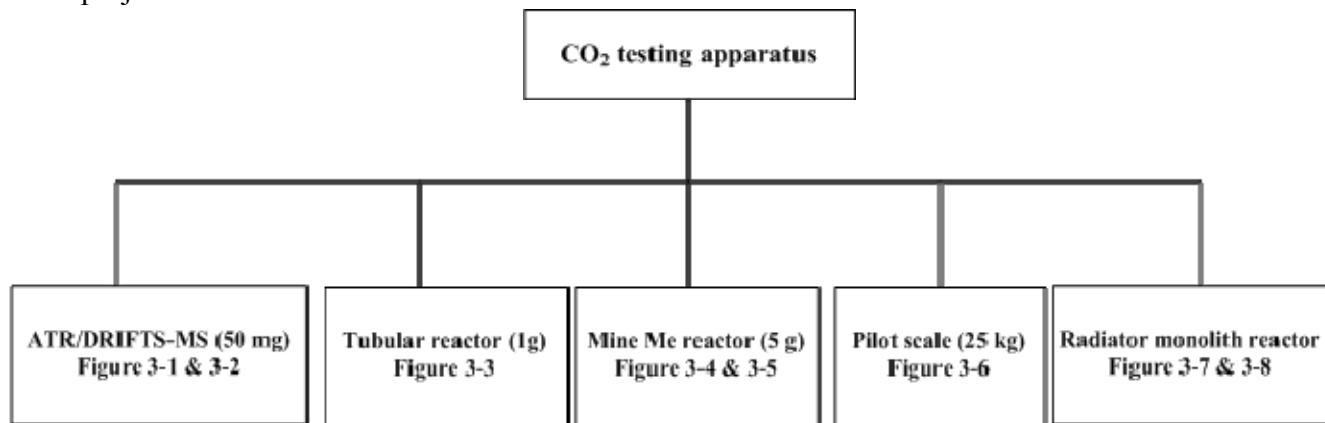
Flow chart of different stages of screening the sorbents

3.1 In Situ ATR-IR Reaction Studies

  The experimental apparatus, shown in Figure 3-1 consists of (i) a reactant metering system (Brooks Instrument 5850 mass flow controllers, (ii) a gas sampling section including a 4-port valve, (iii) a Attenuated Total Reflectance accessory (ATR-IR, Harrick Scientific) and a custom reactor manifold mounted to the ATR-IR top plate mounted inside an Fourier Transform Infrared Spectrometer (FTS6700 FTIR, Thermo-Nicolet), and (iv) a mass spectrometer (MS, Pfeiffer Omnistar^{TM}). The 4-port valve allows switching the inlet flow from 100% N_2 to 100 % CO_2 while maintaining a total flow rate of 100 cm^3/min over the liquid sorbent.

  The changes in the concentration of IR-observable adsorbates are monitored by FTIR. The IR absorbance spectrum of adsorbed and gaseous species is obtained by A=-log (P_o/P) [3], where P_o is the background IR single beam spectrum (32 co-added scans and resolution 4 cm^{-1}) of the catalyst under 100% N_2 flow and P is the IR single beam spectrum during the adsorption study. The MS responses corresponding to N_2 (m/e = 28), CO_2 (m/e = 44), and H_2S (m/e=34) are monitored for the changes in the ATR-IR reactor effluent concentrations.
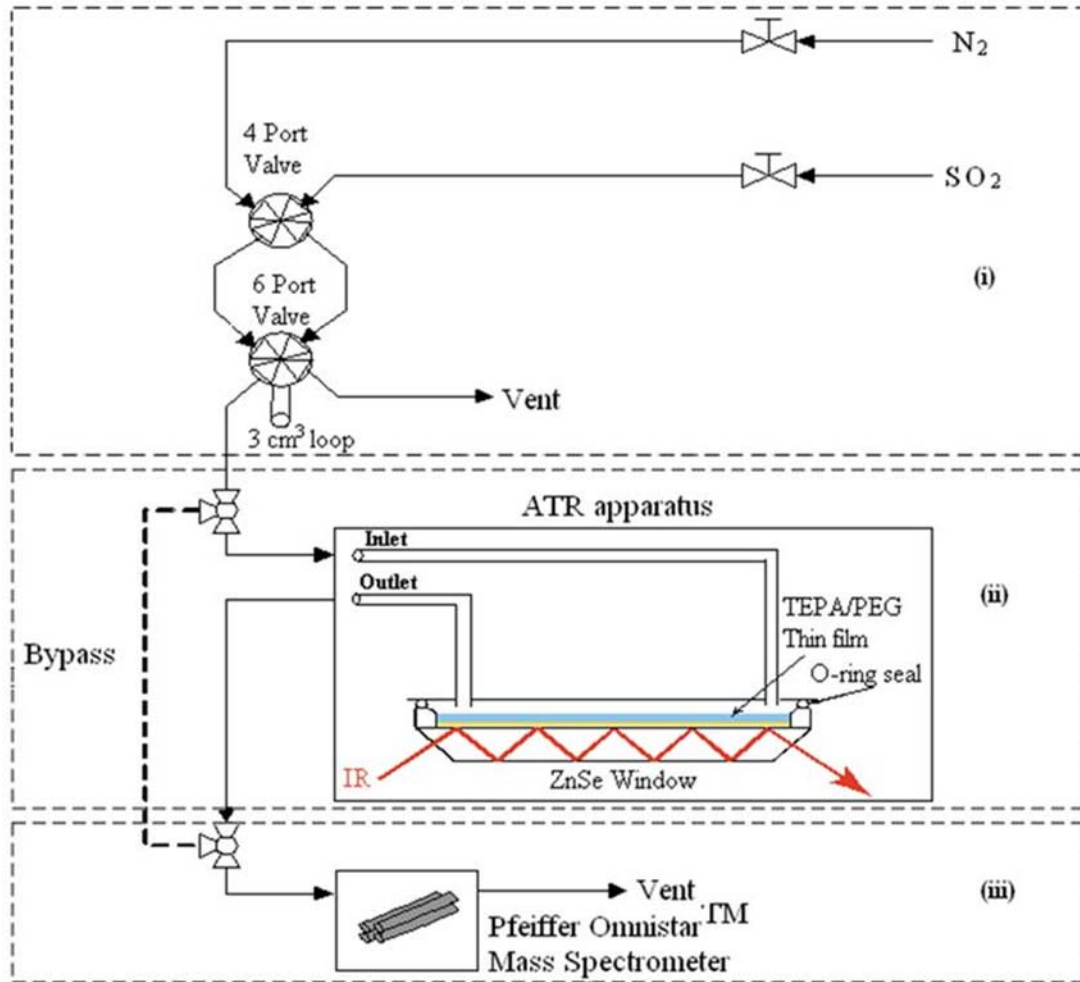
Figure 3-1   Experimental apparatus for In-situ ATR experiments for liquids

3.2   In-situ DRIFTS apparatus for cyclic CO_2 capture studies

The experimental apparatus, shown in Figure 3-2, consists of (i) a gas manifold with mass flow controllers, H_2O saturator, a 4-port valve, and a 6-port valve, (ii) a DRIFT (Diffuse Reflectance Infrared Fourier Transform, Spectra-Tech) cell filled with 70 mg of the sorbent, (iii) a Nicolet 6700 FT-IR bench (IR), (iii) a Pfeiffer QMS 200 quadruple mass spectrometer (MS), and (iv) a signal input-output module for controlling the 4-port, 6-port valve position, DRIFT cell temperature, and heating rate. The gaseous stream flowed through the 70 mg sorbent bed in the DRIFT cell from the top to the bottom. The in-house computer user interface and control codes were developed using Labview (National Instrument) software.

CO_2 capture cyclic studies on $TEPA/SiO_2$ and $PEG/TEPA/SiO_2$ consist of the following steps: (i) exposing to 150 cm^3/min of Ar for pretreatment at 55 ^oC , (ii) flowing 150 cm^3/min of CO_2/H_2O/air (15 vol% CO_2, 4 vol% H_2O, and balance air) over the sorbent at 55 ^oC for 5 min for CO_2 adsorption, (iii) switching back to Ar flow to remove the weakly adsorbed CO_2, and (iv)

10

performing temperature programmed desorption at a heating rate of 20 $^{\circ}$C/min in 150 cm^3/min of flowing Ar. The structure of adsorbed CO_2 species and their intensities were determined by DRIFT. Single beam spectra were taken at a scanning mode with 32 co-adding scan and resolution of 4 cm^{-1} at a rate of 6 scans/min. The absorbance spectrum were obtained by the equation: Abs. = log(I_0/I) where I is single beam spectrum of interest and I_0 is the reference single beam spectrum. The composition of the DRIFT cell effluent was monitored by MS. The MS CO_2 profile (m/e=44) was calibrated by pulse injection of 3 cm^3 and 5 cm^3 via 6-port valve. The calibration factor was calculated by dividing the area under the CO_2 profile and the amount of CO_2 injected.
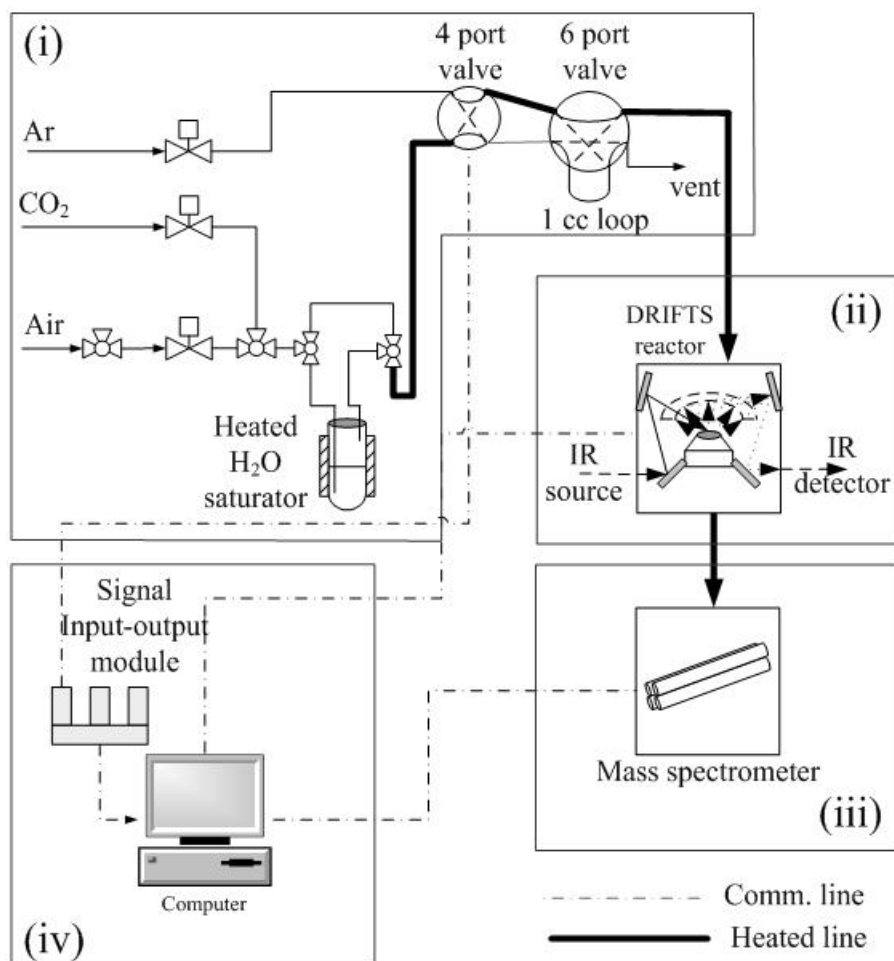
Figure 3-2   Experimental apparatus for In-situ DRIFTS used in cyclic CO_2 capture study.

3.3 CO_2 capture study by tubular adsorber (1 g system)

Testing apparatus: The experimental apparatus, shown in Figure 3-3, consists of (i) a gas manifold with mass flow controllers, a 4-port valve, and a 6-port valve, (ii) a tubular reactor with movable heating jacket, (iii) a Pfeiffer QMS 200 quadruple mass spectrometer (MS), and (iv) a signal input-output module for controlling the 4-port, 6-port valve position, DRIFT cell

temperature, and heating rate. The in-house computer user interface and control codes were written with Labview (National Instrument) software.
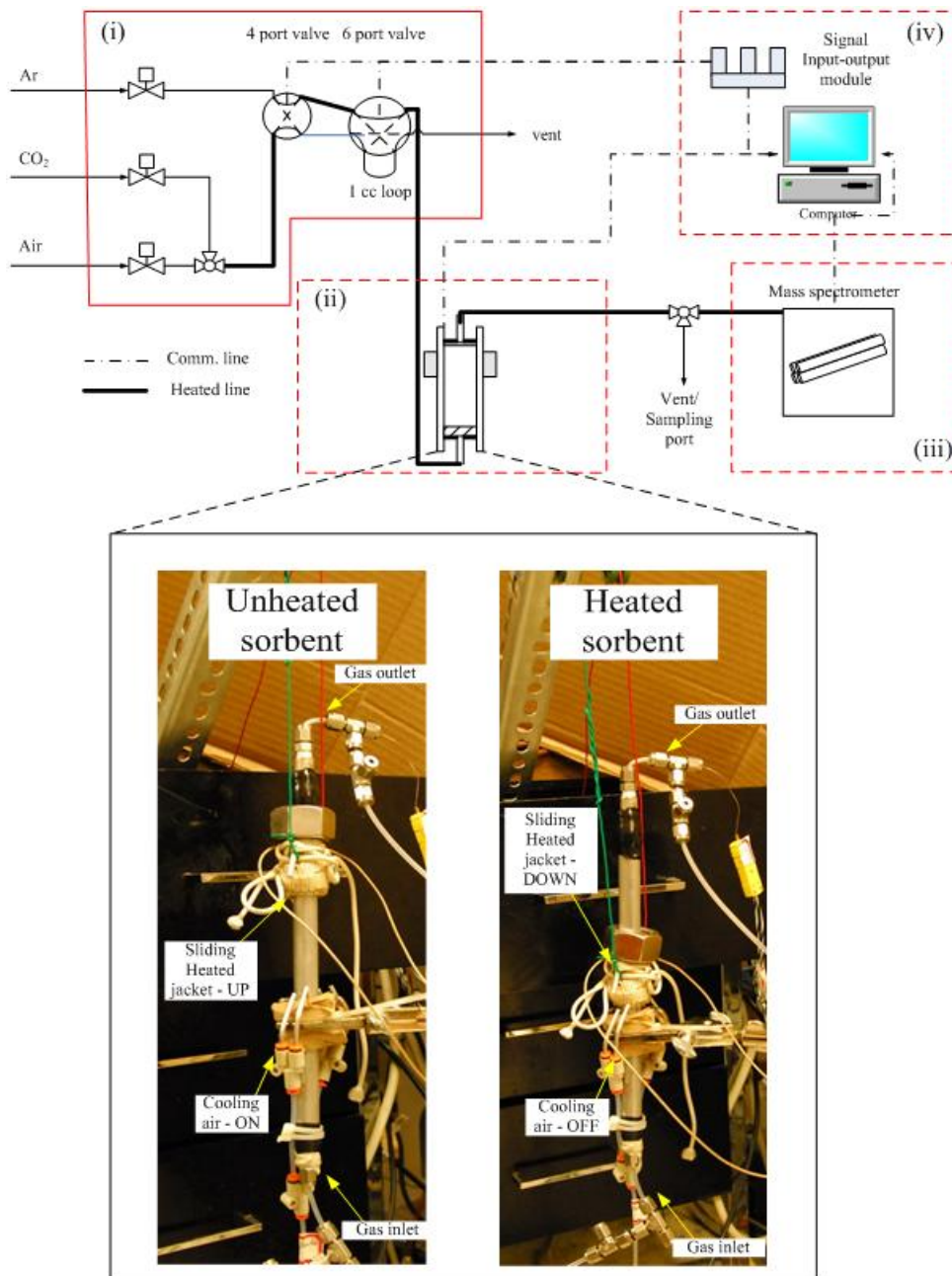
Figure 3-3   Experimental apparatus for CO_2 capture study by tubular adsorber.

Cyclic CO_2 adsorption/desorption studies: One gram of solid sorbent was placed in the tubular reactor. Adsorption of CO_2 on the sorbent was carried out at 40 °C by switching the reactor inlet flow from Ar at 150 cm^3/min to a 15 vol% CO_2 in air (CO_2/air) at 100 cm^3/min for 3 min and back to Ar using a 4-port valve for 2 min to purge out residue CO_2. The sorbent was heated to 100 °C at 5 °C/min and held constant at desorption temperature for 2 min. The temperature was

12

then decreased to 40 $^{\circ}$C at 10 $^{\circ}$C/min to complete one CO_2 adsorption/desorption cycle. The reactor effluent composition was monitored by MS and CO_2 profile (m/e=44) was calibrated by pulse injection of 3, 5, and 10 cm^3 via 6-port valve. The responding (i.e., calibration factor) was calculated by dividing the area under the CO_2 profile and the amount of CO_2 injected.

3.4 Mini Me adsorber (5 g system)

The Mini Me adsorber was loaded with 5.00 g of pelletized sorbent RB-M. The sorbent is contained within the unit by steel meshes at the bottom and top of the bed. A thermocouple is introduced into the bed to monitor the temperature at the middle of the sorbent, (approximately 1 cm above the steel mesh). The loaded adsorber is then reconnected to the utility and gas lines to perform CO_2 capture cycling. The present experiment was performed in two parts, the first operated with a dry gas stream for 100 cycles while the second operated with the CO_2 gas stream flowing through a water saturator at 55°C for 100 cycles. The details of each part are given below.

Figure 3-4   Process schematic of the Mini Me experimental apparatus.

3.4.1 Dry Cycles

Cycling is performed automatically via LabView software under two conditions. The first condition incorporates a 100% CO_2 purge and the second condition utilizes a dry air purge. The program comprises of 8 segments allowing for quick programming adjustments. The first 2
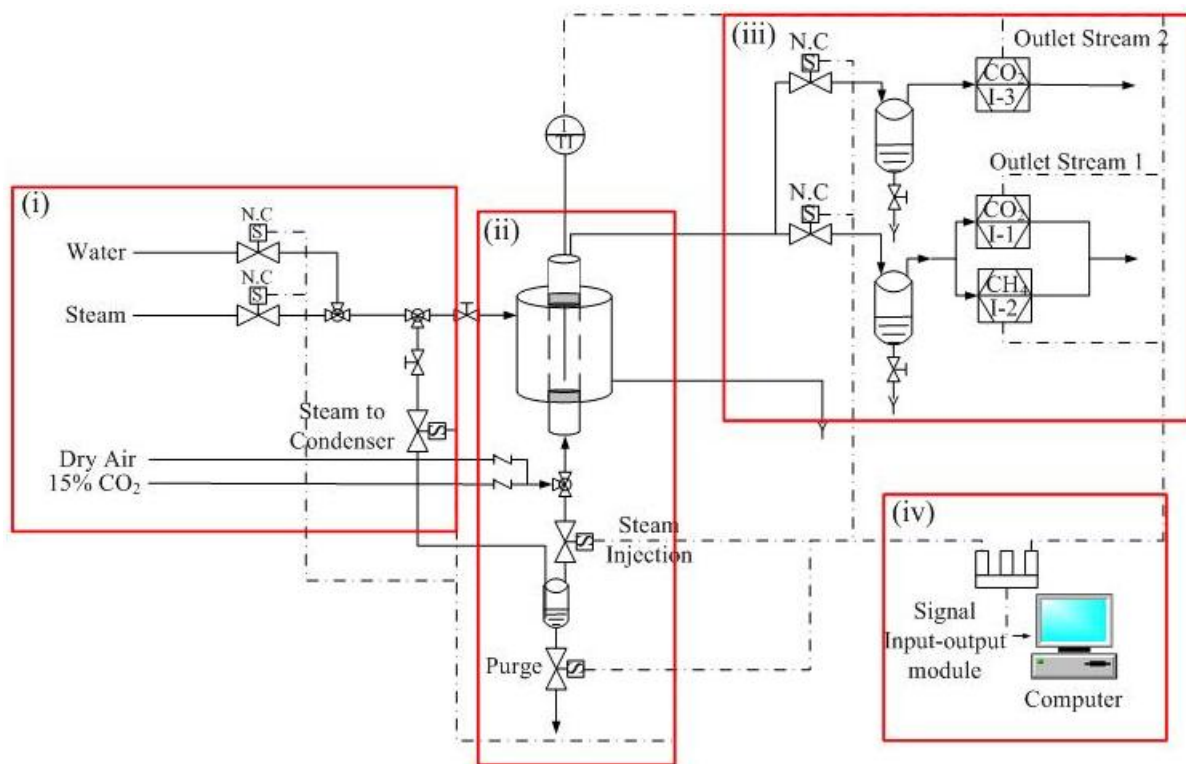
segments are pretreatment steps for desorbing and purging residual CO_2 that may have been adsorbed during sorbent storage. The pretreatment steps are performed once at the beginning of dry cycling process. The remaining 6 segments are designated as the following: cycle step 1 (Cooling), cycle step 2 (CO_2 Adsorption), cycle step 3 (Bed Purge 1), cycle step 4 (Unit Heating), cycle step 5 (Steam Regeneration), cycle step 6 (Bed Purge 2). Cycle step 1 cools the bed down to $50^{\circ}C$ by passing cooing water through a heat exchange jacket for 60 seconds, while keeping the bed inlet and outlet closed. CO_2 adsorption takes place in step 2 by flowing 3 L/min of 15% CO_2, (balanced by air) with a 2-3% CH_4 tracer gas, through the sorbent bed for 5 minutes. The exiting gas is directed to outlet stream 1, refer to Figure 3-4, where the inline CO_2 sensor (I-1) monitors the CO_2 concentration and inline CH_4 sensor (I-2) simultaneously monitors the CH_4 concentration.

Cycle step 3 has been added to the operation to purge the bed under two conditions: (1) flush the bed with 100% CO_2 and (2) replace CO_2 with dry air. Condition (1) flushes the bed with 100% CO_2 flowing at 3 L/min for 10 seconds. The CO_2 purge exits the adsorber through outlet stream 2. The pure CO_2 purge is used to reduce oxidative degradation of the sorbent pellets by removing the residual air from the adsorber; however, the drawback is the generated desorption peak contains CO_2 that had been adsorbed by the pellets and CO_2 occupying the dead space in the adsorber. Therefore, the area of the desorption peaks under the CO_2 purge condition cannot be used to determine the CO_2 capture capacity. To circumvent this problem, cycle step 3 is switched to condition (2) where the 100% CO_2 is replaced with dry air; thus, the CO_2 desorption peak profile consists of only adsorbed CO_2. This peak is used to evaluate the capture capacity.

Cycle step 4 begins by simultaneously closing the inlet and outlet to the bed and opening the steam line into the bed jacket. The steam is also routed to the steam injection vessel to purge for the duration of the step. The unit heating step increases the temperature of the sorbent bed to $100^{\circ}C$. This cycle step lasts for 5 minutes. Cycle step 5 (steam regeneration) is performed by opening outlet stream 2 and the steam injection valve for 5 to 7 seconds. This is done under constant heating through the jacket. The steam travels out of the bed and into outlet stream 2, where it enters a condenser for water removal. The gas concentration of outlet stream 2 is continuously monitored by inline CO_2 sensor I-3. The process finishes the cycle by purging the bed with 3 L/min dry air for 3 minutes. The bed purging is also done under constant heating to prevent water condensation in the bed.

3.4.2   Wet Cycles

The CO_2 capture cycling for the wet cycles are conducted in the same sequence and timing as described above for the dry cycles, including the two conditions of the Bed Purge 1. The difference is 15% CO_2 gas to pass through a water saturator held at 55°C before entering the adsorber during cycle step 2. It is important to point out however, that the dry air line did not pass through the saturator at anytime. By having only the 15% CO_2 gas pass through the

14

saturator and only during the adsorption step, the amount of water accumulation inside the adsorber was regulated. The modified apparatus is shown in Figure 3-5.
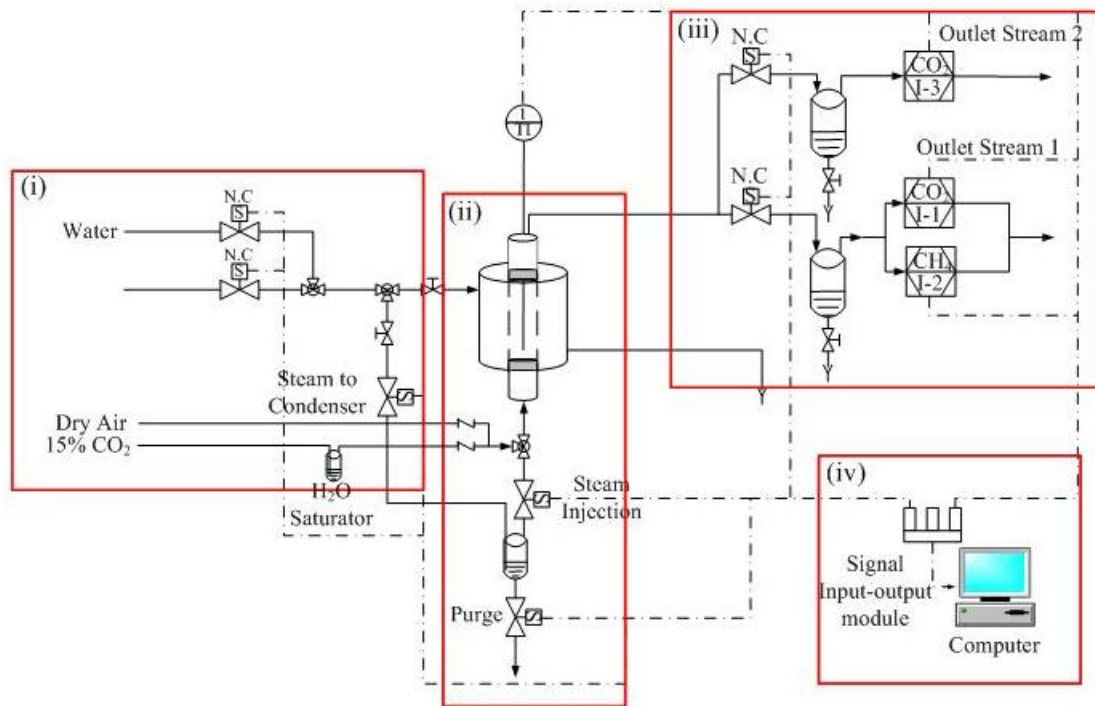
Figure 3-5. Process schematic of the Mini Me experimental apparatus with water saturator.

3.5 CO_2 capture study by pilot scale (25 kg) adsorber

The objective of this experiment is to determine the time required to (i) heat the 25 kg adsorber to an internal temperature of 100°C from RT and (ii) cool the 25 kg adsorber to an internal of 40°C from 100°C.

The schematic of the 25 kg CO_2 adsorption unit is shown in Figure 3-6. The experiment is performed in two sections; pretreatment and CO_2 capture cycling. Pretreatment consists of the following two segments: adsorber heating and bed purging. Adsorber heating increases the temperature of the bed to 100°C, where it is held for 10 minutes. Bed purging is accomplished with dry air at 23 L/min for 5 minutes. The CO_2 capture cycle consists of eight segments; steam to water switch, cooling, CO_2 adsorption, water to steam switch, desorption A, desorption B, dry air purge with heating, and dry air purge without heating. The steam to water switch is a 20 second duration segment where there is no flow of any gas, steam, or cooling water. This segment allows the adsorber heating lines to drain before flowing cooling water. Cooling is achieved by passing water through the inner and outer annular jackets to reduce the internal temperature of the adsorber to 55°C. In the CO_2 adsorption segment, a mix of 15% CO_2 and 2.5% CH_4 pass into the adsorber unit at a volumetric gas flow rate of 23 L/min for 15 minutes.

The outlet gas concentrations are monitored by two inline sensors; I-1, I-3. I-1 is a CO_2 gas sensor, (Guardian Plus), with a range of 0-30 vol% and I-3 is a CH_4 gas sensor, (Guardian Plus), with a range of 0-5 vol%. Steam is introduced into the inner and outer annular jackets of the adsorber in desorption A to increase the internal temperature of the adsorber to $100^{\circ}C$. This temperature is maintained for 10 minutes to desorb the captured CO_2 and regenerate the sorbent. During desorption A the inlet and outlet of the adsorber are closed. The desorbed CO_2 gas is forced from the adsorber via a direct steam pulse through the bed in desorption B. The CO_2 concentration of the exiting gas is monitored by sensor I-2, (Scientific Sensor Controls) throughout the duration of the step. In this experiment, two steam pulse times of 8 seconds and 15 seconds were used. The adsorber is purged with dry air, under constant heating at a volumetric flow rate of 23 L/min for 3 minutes. The steam is shut off and the unit continues to purge for 5 more minutes. The CO_2 concentration of the exiting gas during both purging segments is monitored by sensors I-1 and I-3.
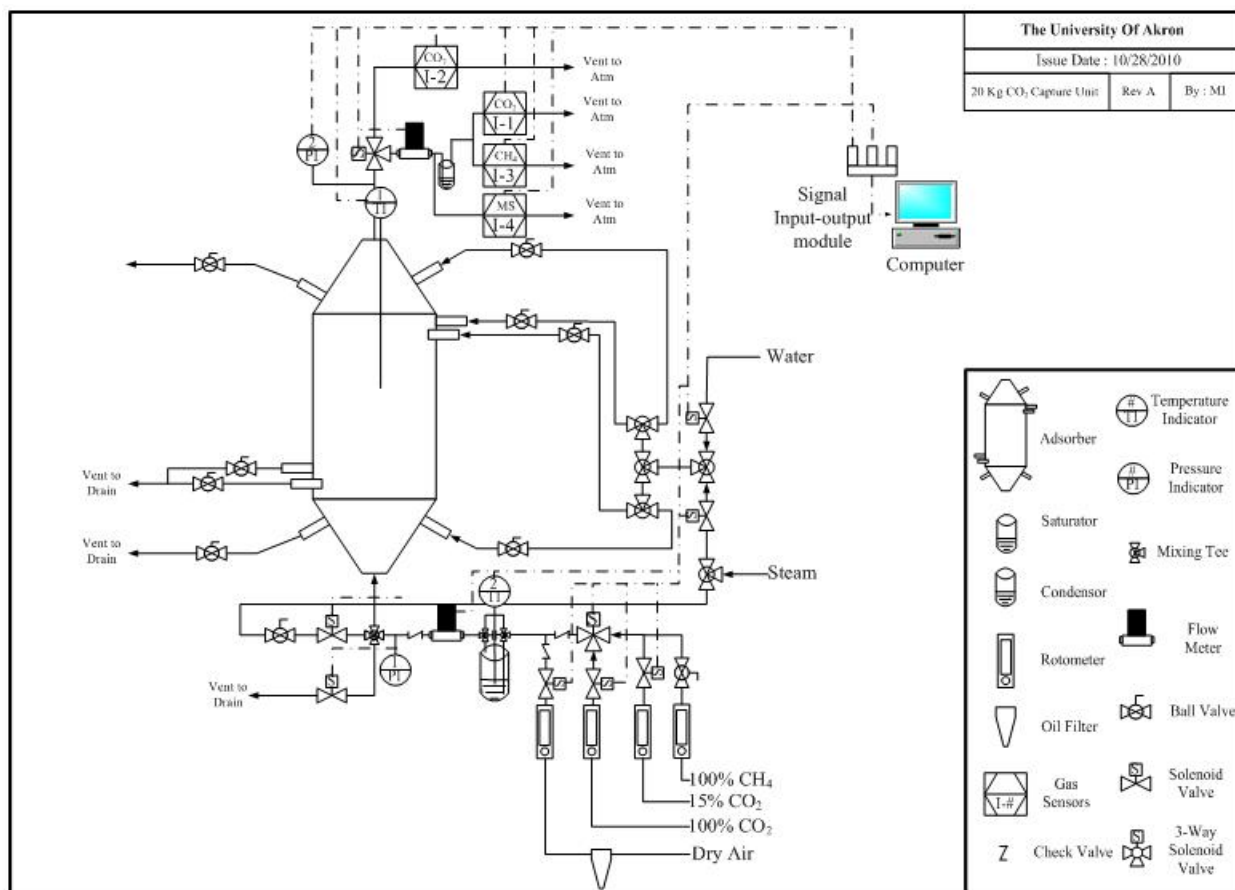

Figure 3-6   Schematic of the 25 kg CO_2 adsorption unit.

The 25 kg adsorber was loaded with 6 kg of pelletized sorbent. A thermocouple was placed 0.5" deep into the top of the sorbent bed. Thermocouples were placed within the entering and exiting steam lines to measure the inline temperature of the steam. The maximum steam

flow rate was calculated between 150 and 210 L/min. The cooling water flow rate was calculated to be 140 L/min. The adsorber was heated through an external and internal jacket. The steam flow was interrupted once during the heating cycle for 5 minutes. The outlet valves of the steam lines were closed during the steam interruption to allow the pressure to build to 5 psi within the steam lines. The heating cycled continued until the adsorber obtained an internal temperature greater than 90°C. The cooling cycle was performed by passing cooling water through the same external and internal jacket used in the heating cycle. The cooling cycle continued, uninterrupted, until the internal temperature of the adsorber dropped to 40°C.

Table 3-1   Summary of experimental conditions

Segment Label	Segment Description	Media Flow Rate	Media	Conc. (vol%)	Adsorber Temperature (^{o}C)	Sensor	Hold Time
-1	PT-Heating	≈180 L/min	Steam	Sat	100	I-2	10 min
0	PT-Purge	23 L/min	Air	100%	100	I-2	5 min
1	St→Wt Switch	N/A	N/A	N/A	100	I-1, I-3	20 sec
2	Cooling	≈140 L/min	Water	N/A	40-55	I-1, I-3	3 min
3	CO_2 Ads	23 L/min	CO_2, CH_4	15%, 2.5%	40-55	I-1, I-3	15 min
4	Wt→St Switch	N/A	N/A	N/A	40-55	I-2	20 sec
5	Des A (through jackets)	≈180 L/min	Steam	Sat	100	I-2	10 min
6	Des B (through bed)	≈180 L/min	Steam	Sat	100	I-2	(i) 8 sec (ii) 15 sec
7	Heated Air Purge	23 L/min	Air	100%		I-2	3 min
		≈180 L/min	Steam	Sat	100		
8	Air Purge	23 L/min	Air	100%	40-55	I-1, I-3	5 min

3.6   CO$_2$ Capture with Radiator Monolith Adsorber

The monolith adsorber was prepared by coating a standard motorcycle radiator with approximately 200 g of sorbent slurry. The radiator has dimensions of 12"W x 9"H x 2"D. The slurry was dried to the outer fin surface of the monolith (radiator) by passing steam through the inner chamber. The drying process resulted in 150 g of sorbent coating the monolith. A container was built around the monolith to allow for a gas inlet and outlet. The monolith divided the container so that gas entered on side, where it was forced to diffuse through the monolith and exit out the other side of the container. Figure 3-7 shows the digital images of the monolith adsorber.
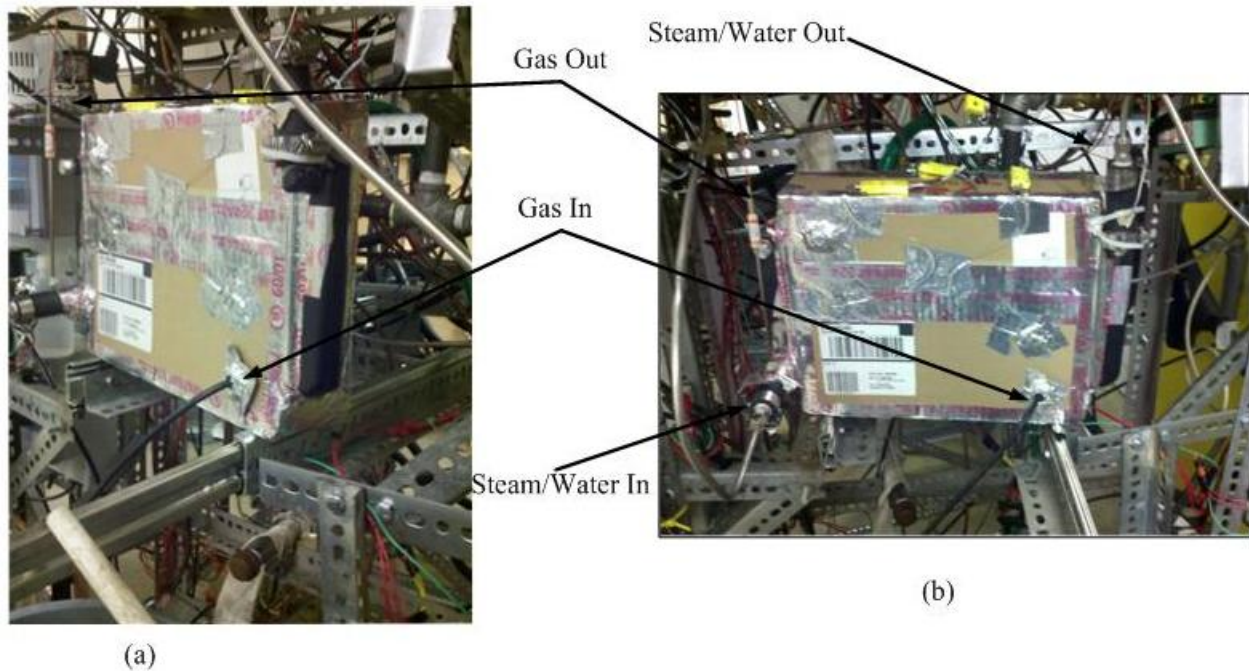
Figure 3-7 (a) side and (b) front images of the monolith adsorber.

The process schematic of the experimental apparatus is shown in Figure 3-8. Cycling is performed automatically via LabView software. The program comprises of 7 segments allowing for quick programming adjustments. The first 2 segments are pretreatment steps for desorbing and purging residual CO$_2$ that may have been adsorbed during sorbent storage. The pretreatment steps are performed once at the beginning of cycling process. The remaining 5 segments are designated as the following: cycle step 1 (Cooling), cycle step 2 (CO$_2$ Adsorption), cycle step 3 (Adsorber Purge 1), cycle step 4 (Desorption 1:Heating), and cycle step 5 (Adsorber Purge 2).

Cycle step 1 cools the monolith surface down to 20 $^{\circ}$C by passing cooing water through an internal heat exchange jacket for 120 seconds, while flowing 5 L/min of dry air. CO$_2$ adsorption follows in step 2 by flowing 5 L/min of 15% CO$_2$, (balanced by air) through the monolith for 600 seconds. The exiting gas is directed to outlet stream, refer to Figure 3-8, where

the inline CO_2 sensor (I-3) continuously monitors the CO_2 gas concentration. Cycle step 3 is the first adsorber purge step. The adsorber purge is done using dry air to flush any uncaptured gas phase CO_2 from the monolith container for 600 seconds. The bed purging facilitates measuring accurate and distinct CO_2 gas concentration peaks during the desorption cycle steps. The desorption cycle step (cycle step 4) heats the monolith surface to 100 °C via passing steam through the internal heat transfer chamber. The monolith heating cycle step lasts for 180 seconds under no gas flow. While maintaining the monolith surface temperature at 100 °C, the dry air is passed into the monolith container for an additional 600 seconds. The dry air pushes the desorbed CO_2 through the outlet stream where the gas concentration is continuously monitored by inline CO_2 sensor I-3. The dry air purge step concludes the full CO_2 capture cycle and the program repeats cycle steps 1 through 5 until the conclusion of the experiment.
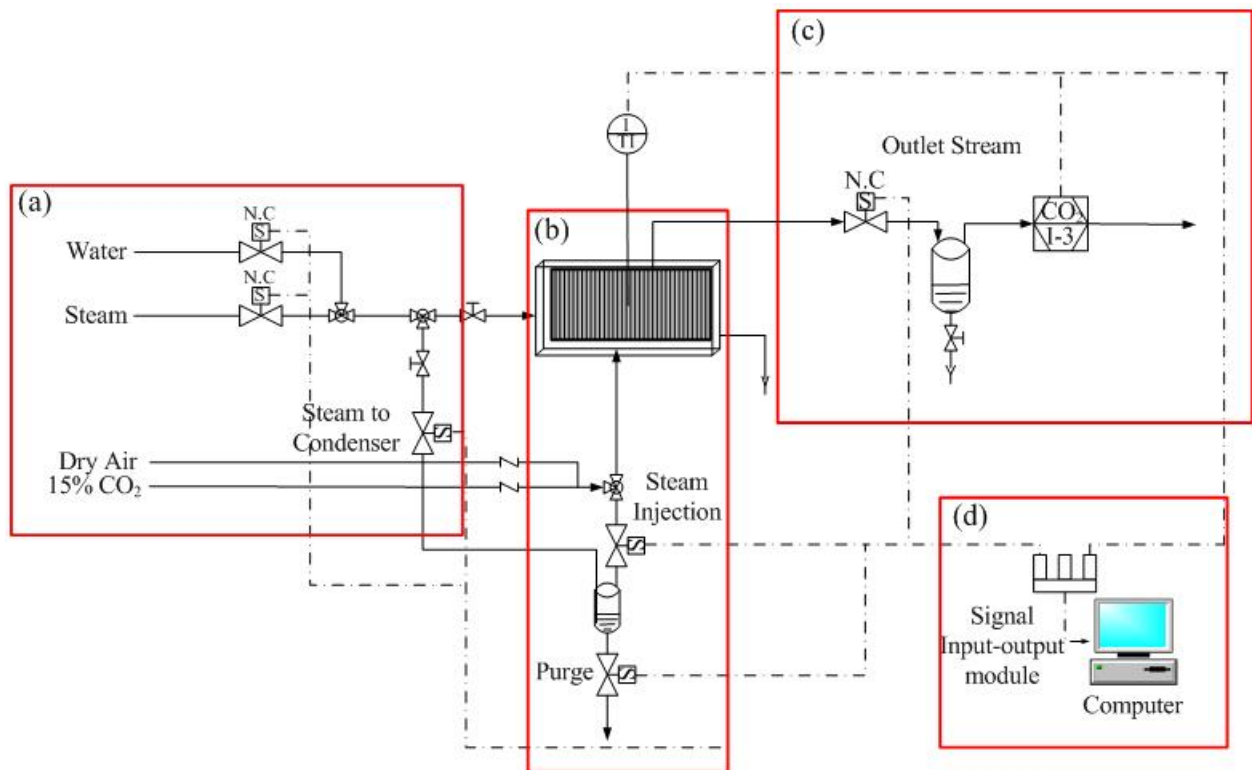

Figure 3-8. Process schematic of the monolith adsorber experimental apparatus.

4 Results and discussion

4.1 The effect of PEG on the CO_2 capture of TEPA

The objective of this study is to determine the effect of the OH functional group in the PEG on the CO_2 capture capacity of TEPA. The study showed that the concentration of PEG can serve as an adjustable parameter to fine-tuning the CO_2 capture capacity of TEPA and CO_2 desorption temperature. The results of this study were used to design the sorbent with desired CO_2 capture capacity and desorption temperatures.

4.1.1 Interactions between TEPA and PEG

Figure 4-1 shows the single beam IR spectra for the pure PEG, TEPA and the blended TEPA/PEG liquid layers. The PEG layer, shown in Figure 4-1(a), exhibit characteristic IR absorption bands for –OH at 3421 cm^{-1}, aliphatic C-H symmetric stretch vibration at 2869 cm^{-1}, C-C-O vibration at 1296 cm^{-1}, and the C-O vibration at 1121 cm^{-1}. The TEPA layer, shown in Figure 4-1 (b), show characteristic bands which can be ascribed to the well known group frequencies [4]. The NH_2 group gives a band due to the antisymmetric vibration at 3353 cm^{-1} and symmetric vibration at 3278 cm^{-1}. The IR adsorption at 1574, 1673, and 3187 cm^{-1} are assigned to the NH_2 deformation and overtone vibrations respectively. The C-C-N stretch vibration occurs at 1128 cm^{-1} [4].

Figure 4-1 (c-g) compare the IR spectra for 9.1, 16.7, 23.0, 29.0, and 33.3 wt % PEG + TEPA blended liquid layers at 323 K. Blending 9.1% PEG into TEPA, shown in Figure 4-1 (c), results in the formation of three distinct N-H absorption bands at 3354, 3282, and 3211 cm^{-1} along with the appearance of an absorption band at 1672 cm^{-1} that is assigned to the NH_2 bending mode as compared to the TEPA only in Figure 4-1 (b).
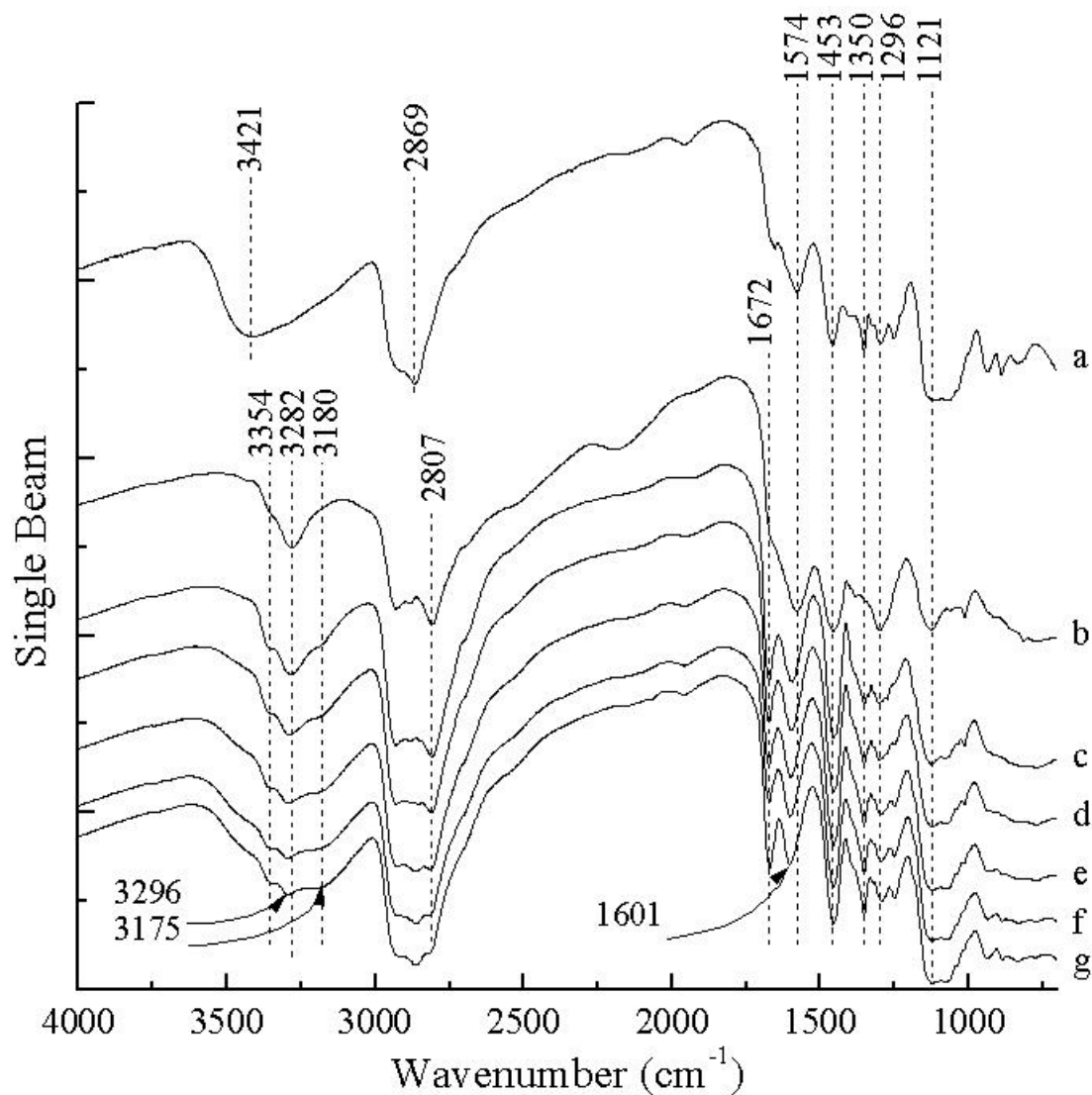
Figure 4-1   IR single beam spectra, effect of PEG on the 4 micron TEPA liquid layer. The PEG Loading: (a) 100 wt% PEG, (b) 100 wt% TEPA, (c) 9.1 wt% PEG/TEPA, (d) 16.7 wt% PEG/TEPA, (e) 23.0 wt% PEG/TEPA, (f) 29.0 wt% PEG/TEPA, (g) 33.3 wt% PEG/TEPA at 323 K.
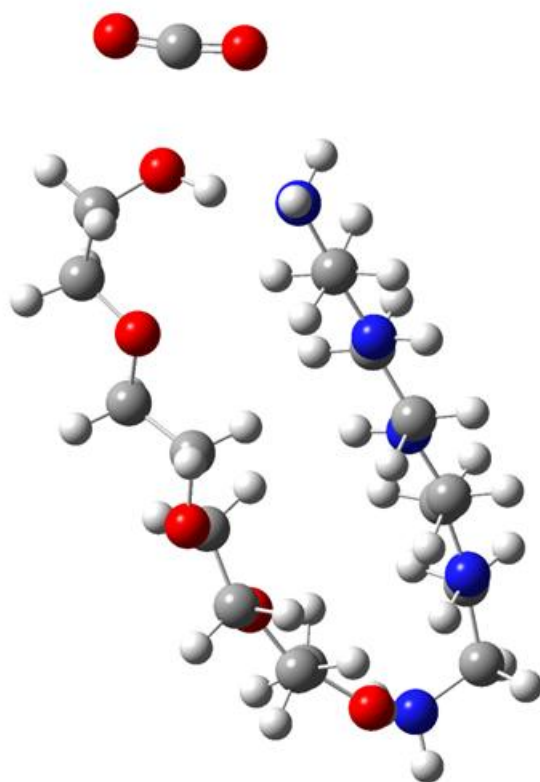
Figure 4-2   Geometry of TEPA/PEG and CO_2 at the optimized B3LYP/6-31++G* level.

The hydroxyl group from the PEG interacts with the amine group through hydrogen bonding consisting of (hydroxyl group of PEG donating hydrogen) $O-H \cdots N$ (nitrogen of the amine accepting hydrogen). The hydroxyl-amine interaction is confirmed from the optimized structure at the B3LYP/6-31++G* level shown in Figure 4-2 Increasing the concentration of PEG in the TEPA liquid layer resulted in the appearance of the NH_2 bending vibration at 1672 cm^{-1} and results from PEG dispersing the TEPA molecules on the ZnSe window. Increasing the PEG concentration on TEPA further broadens the N-H stretching region. Table 4-1 shows the calculated binding energies for adsorbed species at the B3LYP/6-31++G* and B3LYP/6-31G optimized level.

Table 4-1. Calculated binding energies for adsorbed species at the B3LYP/6-31++G* and B3LYP/6-31G optimized level.

Basis set	PEG + CO_2 (kJ/mol)	TEPA + CO_2 (kJ/mol)	TEPA +PEG + CO_2 (kJ/mol)	TEPA + H_2S (kJ/mol)	TEPA + PEG + H_2S (kJ/mol)
6-31++G*	-4.81	-23.19	-15.07	-19.86	-17.71

(6-31G)	(-15.05)	(-45.71)	(-47.23)	(-55.38)	(-36.04)

4.1.2 CO2 adsorption

4.1.2.1 TEPA

Figure 4-3 shows the difference IR spectra of the molecular and adsorbed species during CO_2 adsorption over the TEPA liquid layer at 323 K. Exposure of TEPA to the CO_2 flow led to an increase in IR intensity at 3302 cm^{-1} for N-H stretch, the formation of a broad IR band centered at 2580 cm^{-1} for hydrogen bonding and the formation of carbamate species in the 1600 – 1200 cm^{-1} region. Positive IR peaks for the carbamate species include (i) a shoulder at 1630 cm^{-1} for the R-$NH_2CO_2^-$ symmetric stretch [5], (ii) the NCO_2^- asymmetric stretch at 1567 cm^{-1} and, (iii) the monodentate bicarbonate asymmetric vibration at 1463 and symmetric vibration at 1297 cm^{-1} [6-9]. Increasing IR intensities for the carbamate species, the N-H stretch vibration at 3302 cm^{-1} and the broad band at 2580 cm^{-1} indicate the carbamate species is participating in the IR observable hydrogen bonding effect. Increasing the CO_2 exposure time from 0.00 to 11.13 min did not shift the wavenumber of the IR observable species but caused a variation in IR intensities as a result of greater or lesser amounts of products formed on the TEPA layer.
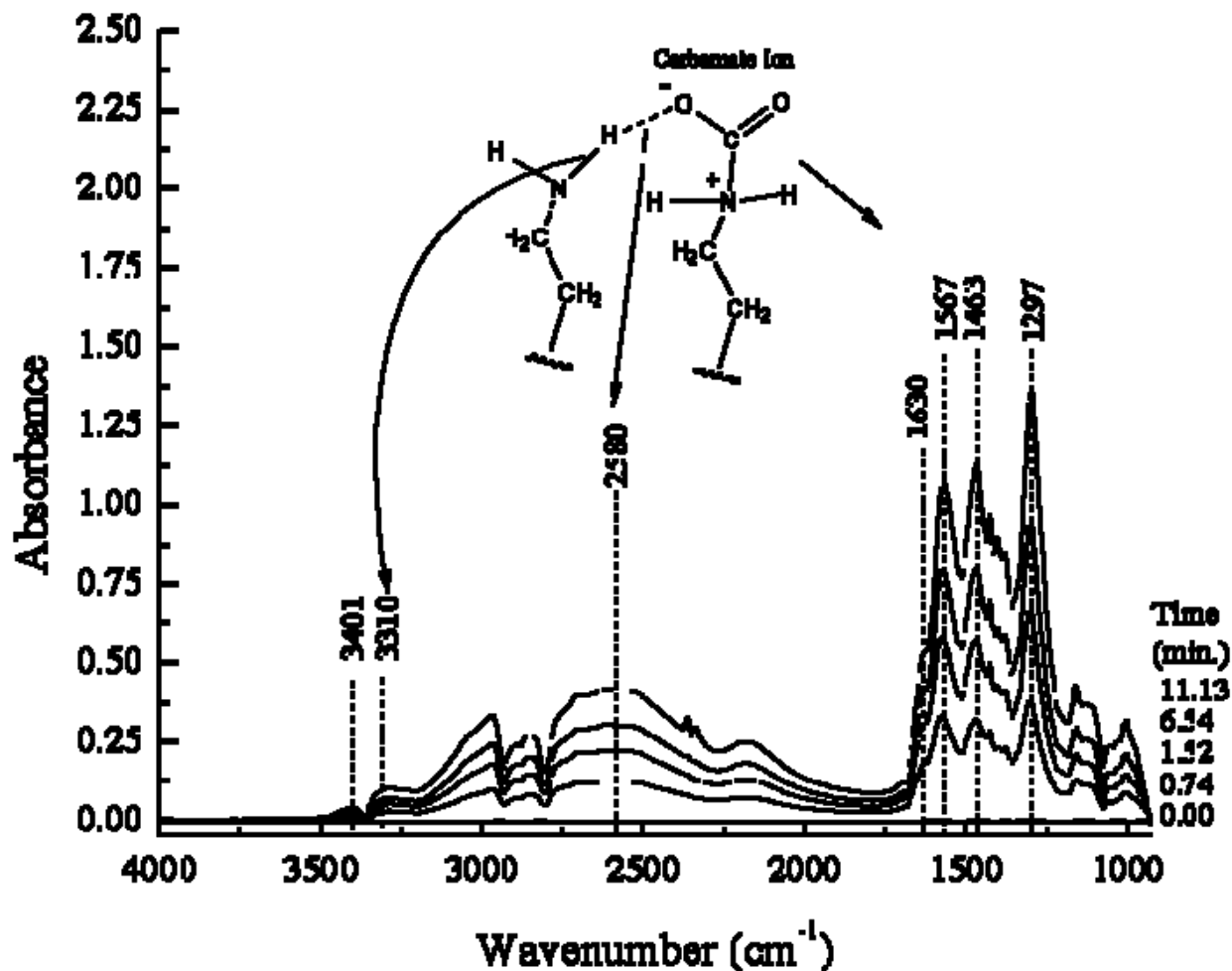
Figure 4-3   IR absorbance spectra sending CO_2 over the 4 micron TEPA liquid layer at 323 K.

Figure 4-4 shows the difference IR spectra while sending isotopic 13CO2 over TEPA liquid layer at 323 K. The presence of isotopic 13CO2 shows an isotopic shift in the carbamate vibrational frequencies, the NCOO vibration shifted from 1567 cm-1 to 1542 cm-1, and the NCOO skeletal vibration shifted from 1463 cm-1 to 1418 cm-1. The shift in the IR frequencies of carbamates indicates CO2 is adsorbing at the amine adsorption site. The broad band absorption at 2580 cm-1, attributed to hydrogen bonding of the carbamate species, did not exhibit the isotopic shift effect.
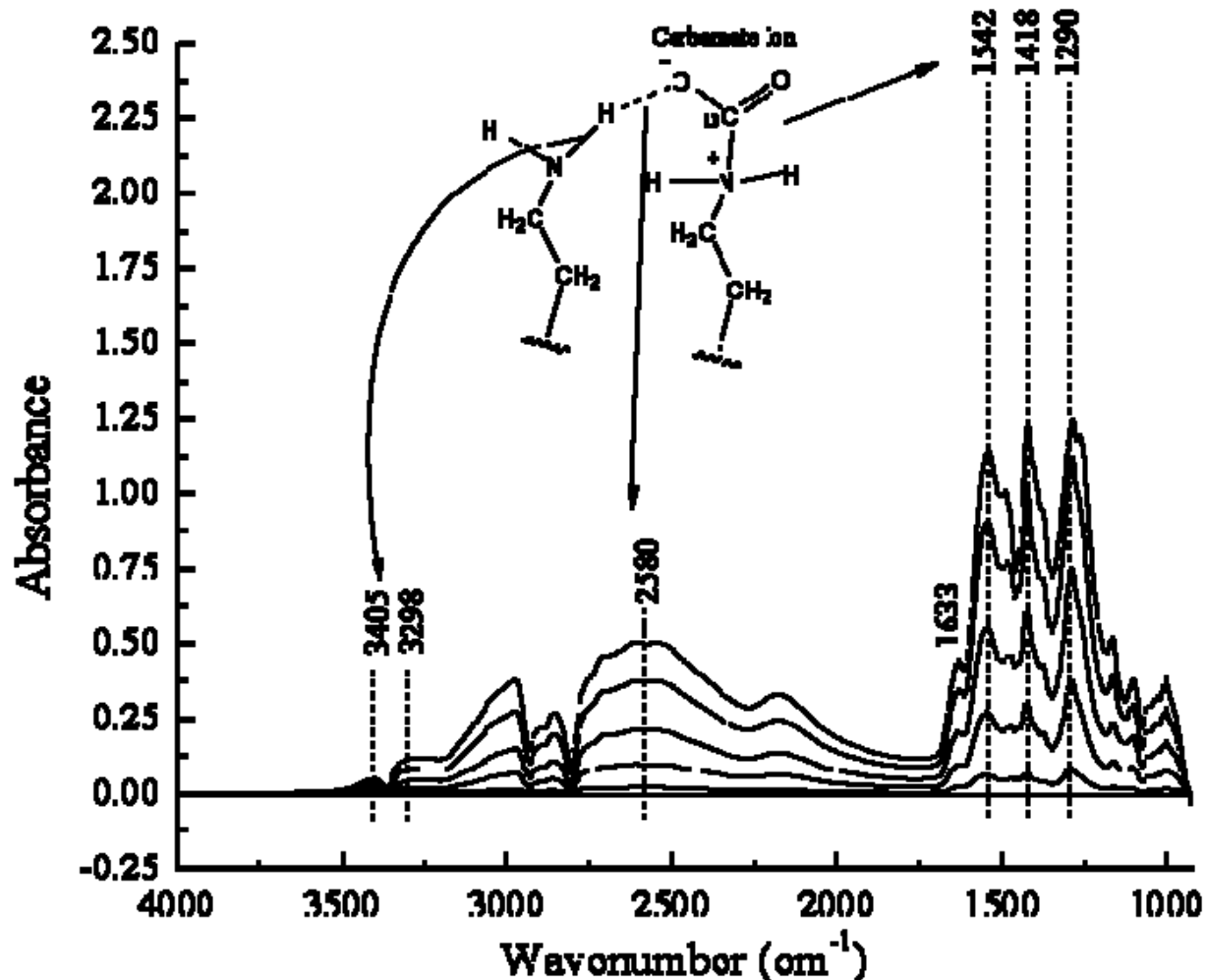
Figure 4-4   IR absorbance spectra sending $^{13}CO_2$ over the 4 micron TEPA liquid layer at 323 K.

4.1.2.2   PEG liquid layer

Figure 4-5 show the IR absorbance spectra during CO_2 adsorption over PEG liquid layer at 323 K. Exposure of PEG to CO_2 flow caused an increase in IR intensity for (i) the R-$CH_2OHCO_2^-$ symmetric stretch at 1635 cm^{-1} and asymmetric stretch at 1565 cm^{-1}, (ii) the monodentate carbonate asymmetric stretch at 1409 cm^{-1} [10], and (iii) the R-CH_2-OH wagging at 1290 cm^{-1}. The interaction of CO_2 with PEG also causes spectral changes in the γ_3 anti-symmetric stretching region producing an intense band at 2338 cm^{-1} similarly to CO_2 adsorption on polymethyl methacrylate (PMMA) [11].
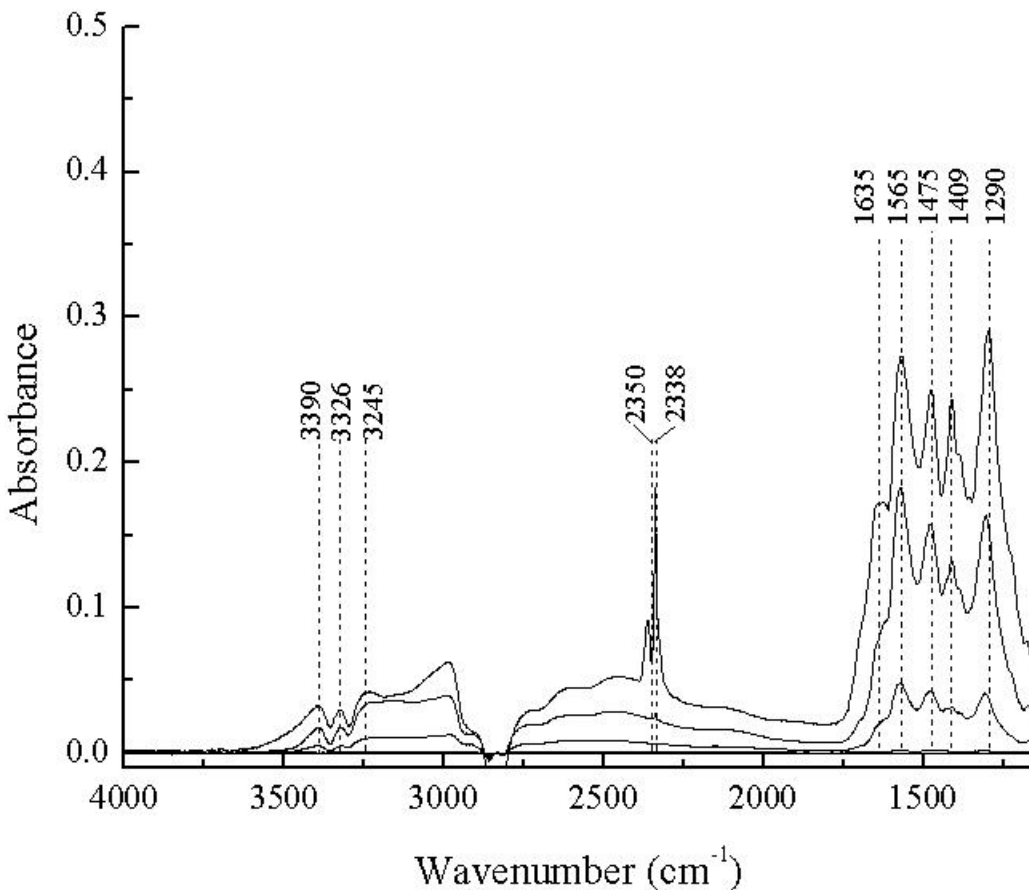
Figure 4-5   IR absorbance spectra sending CO_2 over PEG (MW 200) liquid layer at 323 K.

The IR adsorption bands at 3390, 3326, and 3245 cm^{-1} result from the formation of a hydrogen bonded $CO_2 \cdots O-H$ complex [12]. Switching the inlet flow to N_2 from CO_2, causes the complete desorption of CO_2 from the PEG layer at 323 K; the weakly adsorbed CO_2 results in a lower IR intensity (5 times weaker) than that over TEPA.

4.1.2.3 Blended TEPA and PEG liquid layers

Figure 4-6 show the IR difference spectra during CO_2 adsorption over the blended TEPA and PEG liquid layers at 323 K. Increasing the PEG loading from 9.1 wt% to 33.3 wt%, results in the formation of an immiscible PEG layer indicated by the spectral features, at 23.0 wt% PEG loading, by the formation of (i) the 1409 cm^{-1} band for CO_2 adsorption on –OH (the –OH bending mode appears), (ii) the appearance of the v3 anti-symmetric band at 2338 cm^{-1}, (iii) the changing IR spectral region of the aliphatic C-H stretching region to resemble that of PEG and (iv) the formation of a hydrogen bonding complex similar to that shown in Figure 4-5.

The TPD study of CO_2 adsorption over the TEPA/PEG blended sorbent suggests the optimum PEG loading occurs at 16.7 wt% PEG and TEPA corresponding to 12.83 μmol CO_2 adsorbed and a CO_2/TEPA ratio of 2.24, shown in Table 4-2. The most important spectral

feature during CO_2 adsorption at 16.7 wt % PEG loading occurs at the 1409 cm^{-1} which suggest the slight CO_2 adsorption at the –OH site. The weak binding energy for CO_2 and PEG (-4.81 kJ/mol) along with the spectral evidence for PEG forming an immiscible layer over TEPA suggests that PEG offers the unique ability to adjust the CO_2 desorption temperature.

Figure 4-6   IR absorbance spectra during CO_2 adsorption over (a) TEPA, (b) 9.1 wt% PEG/TEPA, (c) 16.7 wt% PEG/TEPA, (d) 23.0 wt% PEG/TEPA, (e) 29.0 wt% PEG/TEPA, (f) 33.3 wt% PEG/TEPA at 323 K.
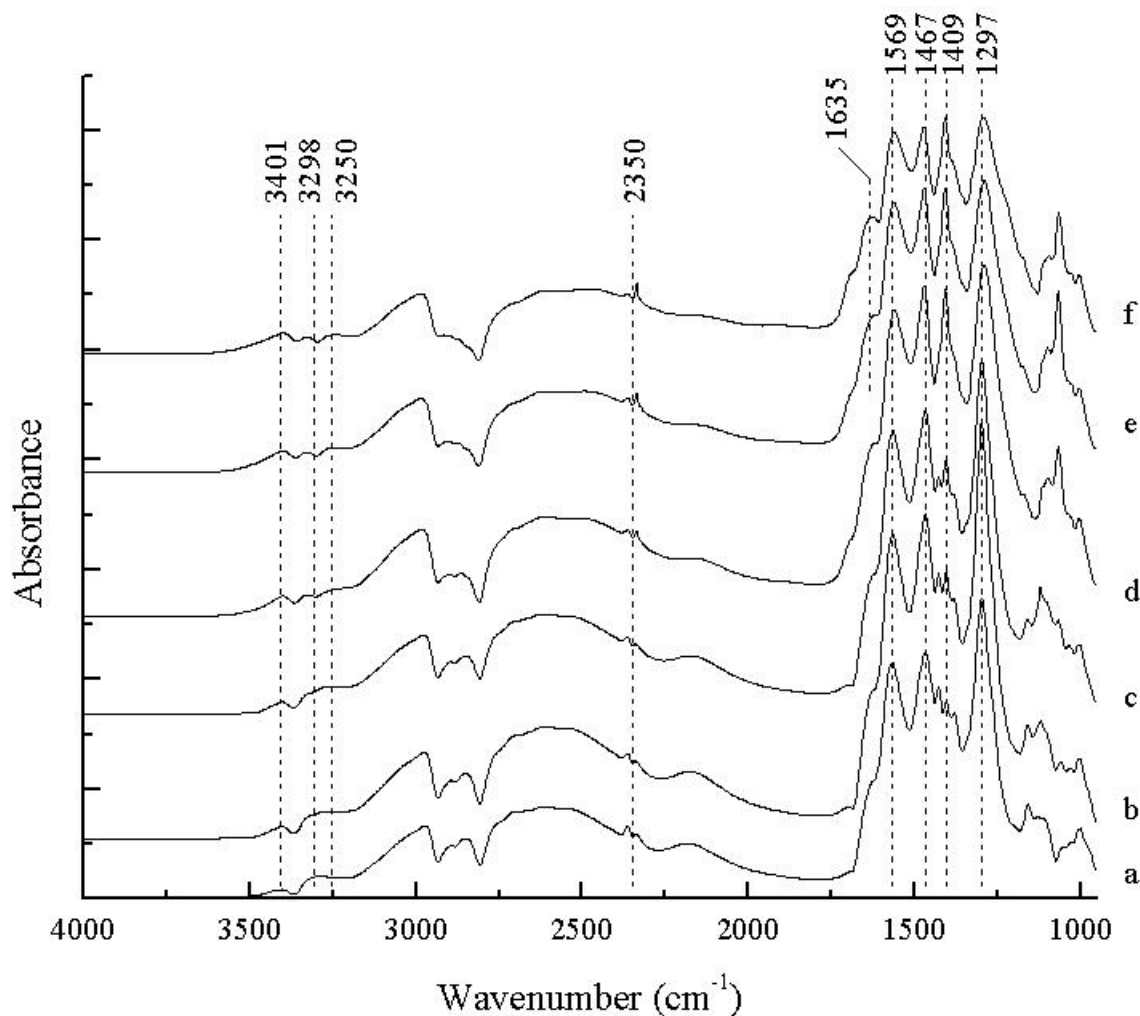
Table 4-2 CO_2 and H_2S Temperature Programmed Desorption over TEPA + PEG liquid layer.

PEG Loading (wt%)	PEG (μmol)	CO_2 (μmol)	$\dfrac{CO_2\,(\mu mol)}{TEPA\,(\mu mol)}$	H_2S (μmol)	$\dfrac{H_2S\,(\mu mol)}{TEPA\,(\mu mol)}$
0.0	0.0	6.84 (373 K)	1.19	0	0
9.1	0.537	8.13 (373 K)	1.41	2.72 (373 K)	0.51
16.7	1.146	12.83 (353 K)	2.24	5.08 (373 K)	0.95
23	1.719	6.41 (343 K)	1.12	32.22 (363 K)	6.00
29	2.292	0.49 (323 K)	0.09	9.56 (343 K)	1.78
33.3	2.865	0.41 (323 K)	0.07	4.76 (343 K)	0.89

Figure 4-7 shows the IR absorbance spectrum during H_2S adsorption on 23.0 wt% PEG-TEPA layer at 323 K. Exposure of the PEG-TEPA layer to H_2S flow caused an increase in IR intensity (i) at 3222 cm^{-1} assigned to the N-H deformation of the NH_3^+ 4 and 1563 cm^{-1} for the symmetric NH_3^+ deformation 13, (ii) at 1549 and 1481 cm-1 assigned to the asymmetric and symmetric bending of the TEPA amine (-NH2) respectively, and (iii) the 1609 cm-1 is assigned to the bending of secondary amines 14. The increase in IR intensity at 1302 cm^{-1} is assigned to the formation of a amine-sulfide structure (-N-S….O-) from the interaction of –NH2, -OH, and gaseous H2S. Interestingly, increasing the PEG loading (to 16.7 and 23.0 wt %), the –CH2– wagging at 1100 cm^{-1} and –CH2-NH2-SH2 rocking at 980 cm-1 become very strong (Figure 4-8) suggesting that PEG disperses the TEPA molecule increasing the number of –NH2 active sites for H_2S adsorption.

The TPD study of H_2S capture over the TEPA/PEG blended sorbent indicates the optimum PEG loading occurs at 23.0 wt% PEG loading on TEPA corresponding to 32.22 µmol

H$_2$S adsorbed and an H$_2$S/TEPA ratio of 6.00, shown in Table 4-2. Interestingly, the PEG loading needed to be increased to 23.0 from 16.7 wt % for H$_2$S (pKa = 6.89) as compared to that for CO$_2$ (pKa = 6.35) capture even though H$_2$S is a little more basic than CO$_2$. The binding energy for the TEPA/PEG-H$_2$S (-17.71 kJ/mol) did not decrease as significantly as that for the TEPA/PEG-CO$_2$ (-15.07 kJ/mol) system.
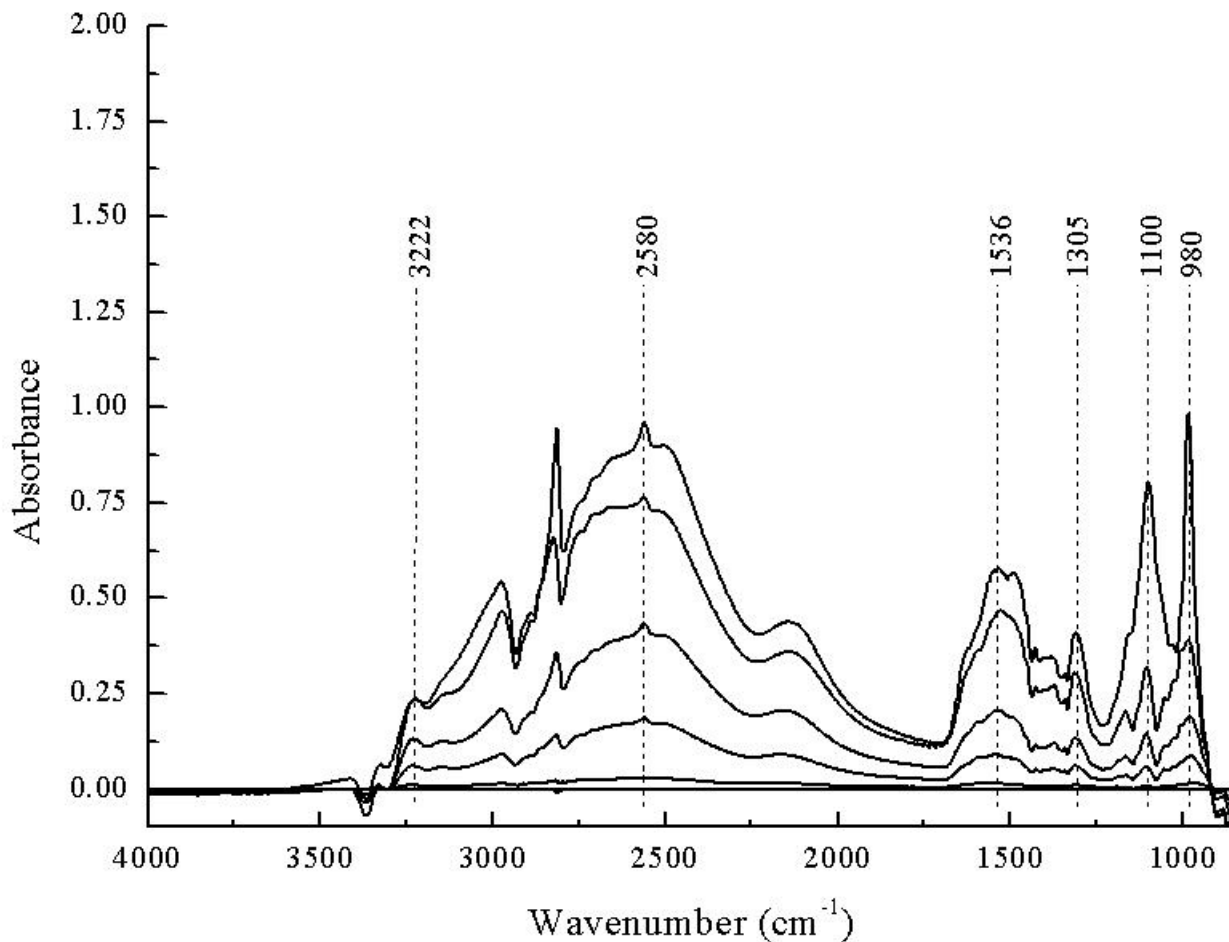
Figure 4-7   IR absorbance spectra sending H$_2$S adsorption over the TEPA + 23.0 wt% PEG liquid layer at 323 K.
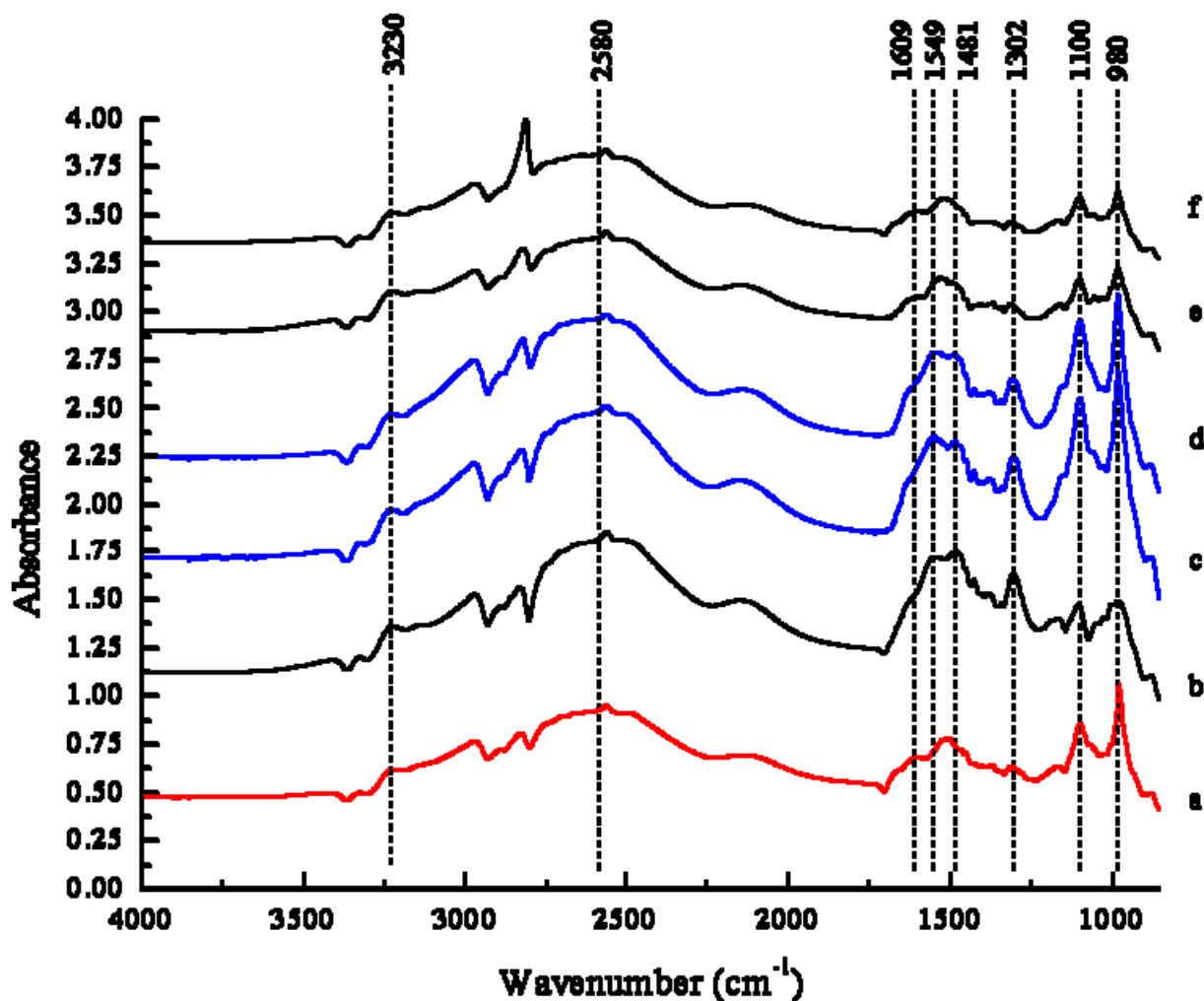
Figure 4-8   IR absorbance spectra during H_2S adsorption over (a) TEPA, (b) 9.1 wt% PEG/TEPA, (c) 16.7 wt% PEG/TEPA, (d) 23.0 wt% PEG/TEPA, (e) 29.0 wt% PEG/TEPA, (f) 33.3 wt% PEG/TEPA at 323 K.

4.1.3   Discussion

CO_2 capture by amine based solid sorbents has been extensively studied [2,6,15-22] and vibrational spectroscopy can provide evidence for the various forms of adsorbing CO_2 species [23]. The IR absorbance spectrum presented in Figure 4-3 and Figure 4-4 suggests that CO_2 adsorbs on TEPA, in the absence of H_2O, as carbonate and bicarbonate species. The reaction pathway on the formation of these various species formed from the reaction of CO_2 with the amine functional groups has been understood to occur by a predominant pathway based upon the concentration of available amine sites [24]. In the absence of H_2O, the predominant reaction believed to account for CO_2 removal is the carbamate formation (see Figure 4-3 and Figure 4-4) according to the reaction step (1).

$$CO_2 + 2R_2NH \quad\quad \leftrightarrow R_2NH_2^+ + R_2NCOO^- \quad\quad\quad\quad (1)$$

30

For every one mole of amine only 0.5 mole of CO_2 is removed, in Step (1), is generally agreed upon in the literature [15,20-22]. The formation of bicarbonate species is known to occur in the presence of H_2O according to reaction steps (2-4).

$$CO_2 + H_2O \quad\quad \leftrightarrow \quad\quad H_2CO_3 \quad\quad\quad\quad\quad\quad (2)$$

$$CO_2 + OH^- \quad\quad \leftrightarrow \quad\quad HCO_3^- \quad\quad\quad\quad\quad\quad (3)$$

$$H_2CO_3 + OH^- \quad\quad \leftrightarrow \quad\quad HCO_3^- + H_2O \quad\quad\quad\quad\quad (4)$$
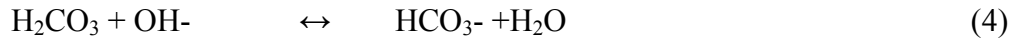
The bicarbonate species may also form directly from the amine plus CO_2 water reaction shown in Eq. (5) and (6).

$$R_2NCOO^- + 2H_2O + CO_2 \quad\quad \leftrightarrow \quad\quad R_2NH_2^+ + 2HCO_3^- \quad\quad\quad (5)$$

$$CO_2 + R_2NH + H_2O \quad\quad \leftrightarrow \quad\quad R_2NH_2^+ + HCO_3^- \quad\quad\quad (6)$$
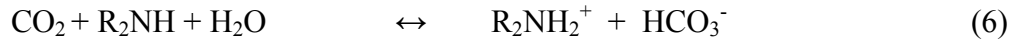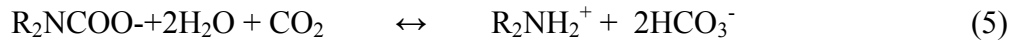
If reaction step (2) is favorable, in the presence of water, one mole of amine is effective in removing two moles of CO_2. Reaction on the surface in the presence of H_2O allows more of the active sites of the material to be available for CO_2 removal. Carbamate formation consumes amine and CO_2 at a stoichiometric ratio of 2:1, whereas bicarbonate formation has a stoichiometry of 1:1. Therefore, systems where carbamate formation dominate will have loadings that are not much higher than 0.5 whereas systems with only bicarbonate formation can have loadings close to 1. Interestingly, in this study, the addition of PEG causes an improvement in the stoichiometric ratio of CO_2 to TEPA in the absence of H_2O.
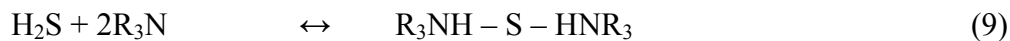
H_2S capture has been studied primarily for desulfurization through the formation of an M-S species on metal oxides and then its oxidation to SO_2 [25-30] and only a few studies have utilized amine based sorbents [13,31] for H_2S removal. Under dry conditions, the main reactions between amine and H_2S are shown in Eq. (7) – (9).

$$H_2S + 2RNH_2 \quad\quad \leftrightarrow \quad\quad RH_2NH - S - HNH_2R \quad\quad\quad (7)$$

$$H_2S + 2R_2NH \quad\quad \leftrightarrow \quad\quad R_2HNH - S - HNHR_2 \quad\quad\quad (8)$$

$$H_2S + 2R_3N \quad\quad \leftrightarrow \quad\quad R_3NH - S - HNR_3 \quad\quad\quad (9)$$
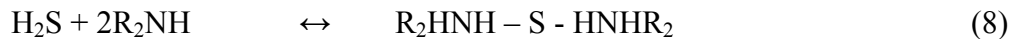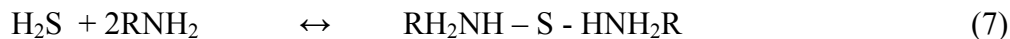
The reaction of H_2S with the amine site, shown in Eq. (7) thru (9), suggests each H_2S molecule requires two amine sites for its adsorption. The stoichiometry of the reaction indicates for every one mole of amine 0.5 mole of H_2S is removed (step (7)). These reactions for H_2S adsorption on the amine active sites have been confirmed by the computational studies [18]. Interestingly, the formation of the amine-sulphide complex, in-7 and Figure 4-8, suggest that the –OH role in the H_2S adsorption process effectively frees up the amine sites for adsorption and increases the stoichiometric ratio to 2:1.

CO$_2$ adsorbs on PEG, shown in Figure 4-5 very weakly at -4.8 kJ/mol and readily desorbs upon flowing N$_2$ over the PEG film. Comparing Figure 4-3 and Figure 4-5, the ratio of the IR intensity in the carbonate region is 5 times weaker on PEG to that on TEPA spectroscopically verifies the theoretical binding energies for PEG-CO$_2$ (-4.81 kJ/mol) and TEPA-CO$_2$ (-23.19 kj/mol) also having a ratio of 5. The experimental IR and theoretical results suggest blending the TEPA and PEG it is possible to lower the binding energy in a TEPA/PEG-CO$_2$ system. The increased CO$_2$ and H$_2$S capacity and lower desorption temperature on addition of PEG supports theoretical investigation on the interaction of TEPA/PEG-CO$_2$ and TEPA/PEG-H$_2$S. The binding energy for TEPA/PEG-CO$_2$ (-15.07 kJ/mol) is in between that of TEPA-CO$_2$ (-23.19 kJ/mol) and PEG-CO$_2$ (-4.81 kJ/mol). Similarly, PEG addition to TEPA lowers the binding energy for the H$_2$S-TEPA adsorption from -19.86 kJ/mol to -17.71 kJ/mol.

Blending PEG with TEPA results in dispersion of the of the TEPA molecule indicated by the IR spectra shown in Figure 4-1. The most striking spectral feature indicating the dispersing effect of PEG occurs on the initial 9.1 wt % PEG loading and the appearance of the –CH$_3$-NH$_2$ wagging vibration at 1672 cm^{-1} suggests PEG frees the amine active site for adsorption of CO$_2$ or H$_2$S molecules. The hydrogen bonding broadening effect on the N-H bands at 3282 and 3180 cm^{-1} further supports the dispersing effect of PEG.

According to these results two different factors have to be taken into account, (i) the molecular mass for an optimal dispersion of the TEPA molecule on the substrate and (ii) the nature and concentration of the active sites suitable for CO$_2$ capture. The effect of the addition of PEG is to enhance the stability of the overall material through the intermolecular interaction with the TEPA molecule, while enhancing the dispersion effect and the reason for the choice of the 200 MW PEG having approximately the same molecular length as the TEPA molecule.

The dispersion of TEPA by addition of PEG can be attributed to a hydrophilic surfactant effect which explains the immiscible layer formation and could result from a sort of micelle formation around the TEPA molecule. Based upon the results of the IR spectra in Figure 4-1 and during CO$_2$ adsorption in Figure 4-6 the dispersion phenomena may be interpreted as PEG forming between the TEPA molecules. The hydrogen bonding of the –OH with the –NH$_2$ active site, the dispersion mechanism can be schematically represented as shown in Figure 4-9.

The weakly bound H$_2$S and CO$_2$ on PEG offers the unique ability for adjusting the adsorption capacity and desorption temperature by modifying the TEPA/PEG blend composition. Thus it is feasible to increase the adsorption capacity and decrease the desorption temperature of CO$_2$ from the TEPA sorbent by controlling the amine active sites through dispersion effects using a hydroxylated polymer such as PEG.
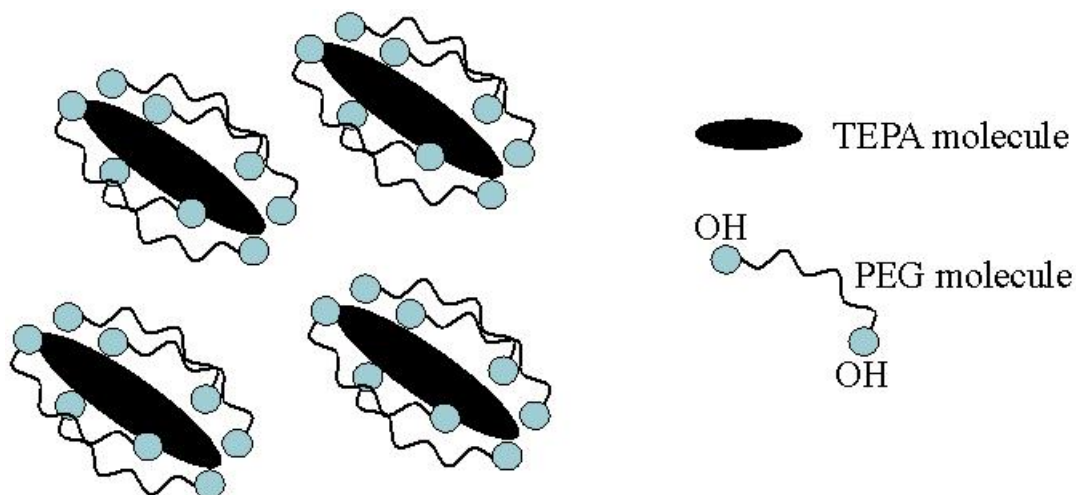
Figure 4-9   Dispersion mechanism of TEPA and PEG system.

4.1.4   Conclusion

CO$_2$ adsorbs on the TEPA/PEG system as carbonates and bicarbonates, while H$_2$S adsorbs as –NH$_2$-SH$_2$ and amine-sulphide (-N-SH$_2$…O-H) complex.   The CO$_2$ adsorption capacity of the TEPA sorbent was doubled by the addition of PEG and increased by a factor of twelve for the H$_2$S adsorption.   H$_2$S adsorption is increased by the formation of the amine-sulphide complex (N-S…O-H) by freeing one of the amine adsorption sites for another H$_2$S molecule.   Dispersion of the TEPA molecule is important during both CO$_2$ and H$_2$S adsorption processes.   PEG disperses the amine adsorption sites enabling more CO$_2$ and H$_2$S molecules to adsorb.   A temperature-programmed desorption study of the TEPA/PEG system showed that PEG offers the unique ability for adjusting the adsorption capacity and desorption temperature (i.e. to 353 K) by modifying the TEPA/PEG blend concentration.   The desorbing temperature was lowered by lowering the binding energy for between TEPA and CO$_2$ and H$_2$S to -15.07 and -17.71 kJ/mol respectively.   These results are attributed to the interactions between the TEPA and PEG additive and CO$_2$ and H$_2$S via hydrogen bonding as verified by IR spectroscopy and ab initio quantum chemistry.   The experimental findings demonstrate that additives including amine and hydroxyl group are suitable for modifying and amine based sorbent for CO$_2$ and H$_2$S removal.

33

4.2   NO and SO_2 adsorption over 1,3-phenylenediamine/SiO2

NO and SO_2 from the flue gas of a coal-fired power can strongly bind with aliphatic amine such as TEPA irreversibly, poisoning the solid amine prepared with aliphatic amine precursors. This study shows that aromatic amine is capable of reversibly with SO_2. Coating immobilized aromatic amine on the solid amine could protect the solid amine from SO_2 poisoning.

4.2.1   NO Adsorption on 1,3-phenylenediamine

Figure 4-10 shows the IR absorbance spectrum during NO adsorption over 1,3-phenylenediamine/SiO$_2$ sorbent. Flowing gaseous NO over the sorbent results in the formation of a nitrosamine species from the interaction of NO with 1,3-phenyelediamine [32-34]. Exposure of NO to 1,3-phenylenediamine results in an increase in IR intensity for (i) N-H vibration at 3442, (ii) deformation band for –NH_2 at 3141 cm^{-1}, (iii) di-nitrosyl (N_2O_4) species at 2117 cm^{-1} [35-36], (iv) adsorbed nitryl NO_2^- at 1662 and 1540 cm^{-1} for γ_{as} and γ_s vibrations [32] respectively, and (v) -CH_2NH_2NO vibration at 1436 cm^{-1} [34]. The appearance of the overtone deformation vibration at 3141 cm^{-1} suggests the IR adsorption at 1662 cm^{-1} may also be assigned to that of –NH_2 deformation during adsorption. The formation sequence of N_2O_4, NO_2^-, and nitrosamine species suggest the NO adsorption process follows the following reaction steps.

$$NO\ (g) + M\text{-}O \qquad \rightarrow \qquad NO_2^- \text{-} M \qquad\qquad\qquad (1)$$

$$NO_2^- \text{-} M \qquad\qquad \rightarrow \qquad M + NO_2 \qquad\qquad\qquad\quad (2)$$

$$NO_2^- \text{-} M \qquad\qquad \rightarrow \qquad 2M + N_2O_4 \qquad\qquad\qquad (3)$$

$$NO_2^- \text{-} M + \text{-}NH_2 \qquad \rightarrow \qquad M + NO_2^- \text{-} NH_2 \text{-} \qquad\qquad\ (4)$$
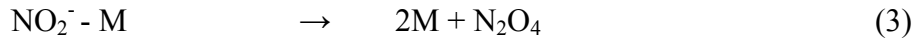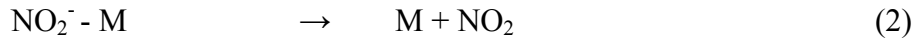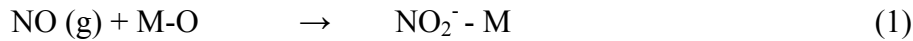
Gaseous NO adsorbs on the oxide surface and is oxidized to adsorbed nitryl NO_2^- in step (1). Adsorbed NO_2^- then desorb to gaseous NO_2 (step 2) or combine to form N_2O_4 species in step (3). Adsorbed NO_2^- may further react with an amine active site to form the nitrosamine species in step (4). The formation of NO_2^- and N_2O_4 suggest SiO_2 support plays an important role in the NO adsorption process. NO adsorption and formation of NO_2^- suggest the amine sites are more reactive for the nitryl species than that of gaseous NO.
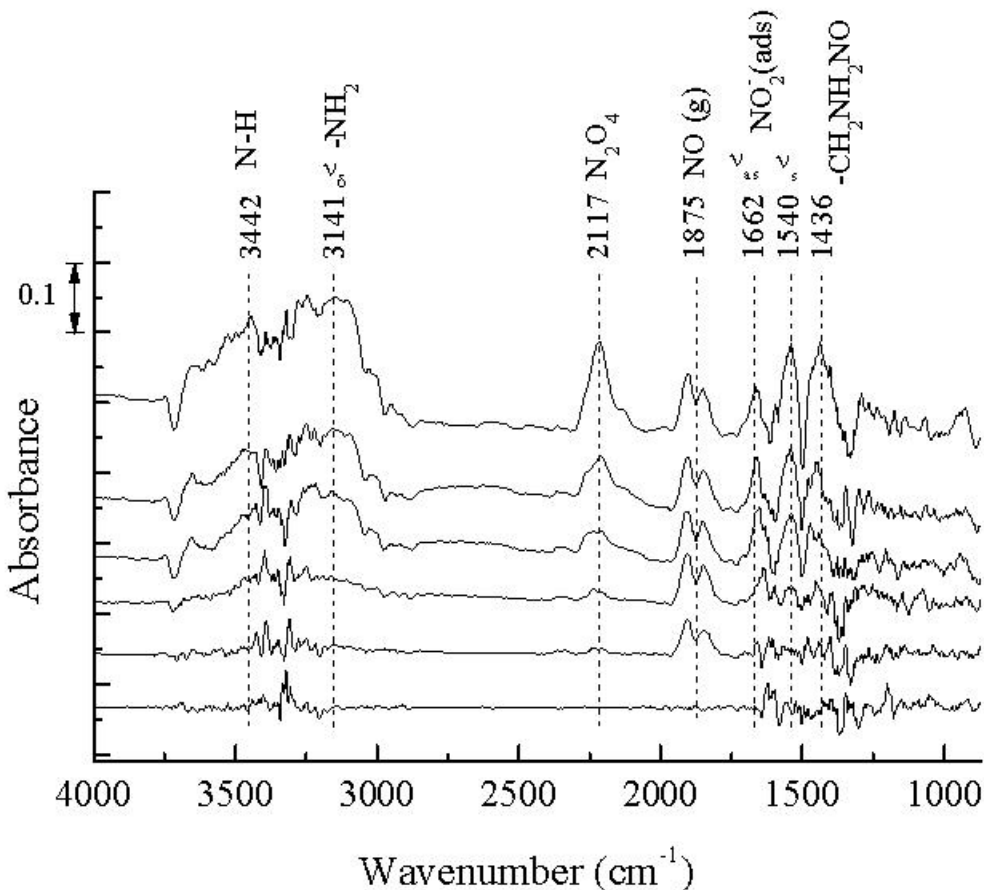
Figure 4-10   IR absorbance spectra during NO adsorption on 1,3-phenylenediamine/SiO2 at 323 K.

4.2.2   SO$_2$ adsorption over 1,3-phenylenediamine/SiO$_2$

Figure 4-11 show the IR absorbance spectra during SO$_2$ adsorption over 1,3-phenylenediamine thin film and 1,3-phenylenendiamine/SiO$_2$ at 323 K. Exposure of SO$_2$ flow to the 1,3-phenylenediamine thin film, in Figure 4-11(a), result in (i) a decrease in IR intensity for N-H vibration at 3420 and 3334 cm^{-1} and the overtone for –NH$_2$ deformation at 3210 cm^{-1}, (ii) a increase in IR intensity for hydrogen bonding broadband in the 3200 – 2000 cm^{-1} region centered at 2905 cm^{-1}, and (iii) a increase in IR intensity at 1531 cm^{-1} for –NH$_2$ deformation vibration. SO$_2$ interacts with the amine functional group at 1408 cm^{-1}, adsorbed sulfite at 1277 cm^{-1}, gaseous sulfite at 1098 cm^{-1}, and monodentate sulfate at 1000 and 941 cm^{-1} [37-38]. The assignment of adsorbed SO$_2$ as sulfite structure is in agreement with adsorption on Y-type zeolites at around 1240 cm^{-1} and on Al$_2$O$_3$ at 1070 cm^{-1} [39].

35
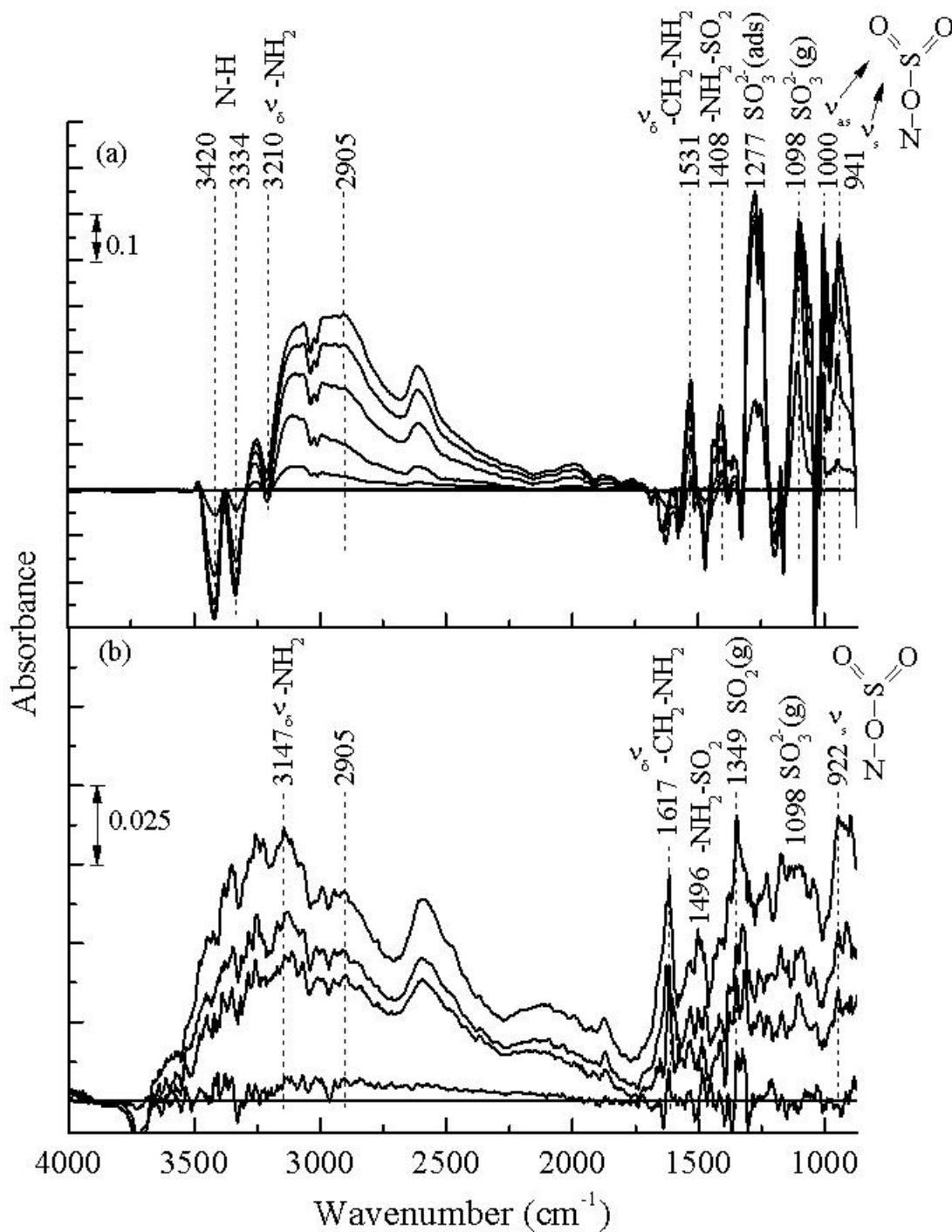
Figure 4-11   SO₂ adsorption over (a) 1,3-phenylenediamine thin film (ATR-IR) and (b) 1,3-phenylenediamine/SiO₂ (DRIFTS) at 323 K.

Figure 4-11(b) shows the IR absorbance spectra during SO₂ adsorption over 1,3-phenylenediamine/SiO₂ supported sorbent at 323 K. Introduction of SO₂ over the sorbent results in an increase in IR intensity at 3147, 1617, and 922 cm⁻¹ indicating the SO₂ adsorption on the

36

amine adsorption site similar to that in Figure 4-11 (a). The adsorption band at 1349 cm^{-1} is assigned to the asymmetric vibration for gaseous SO_2 [40]. The sulfite adsorbate species are weakly adsorbed at 1089 cm^{-1}. SO_2 adsorption on 1,3-phenylenediamine/SiO_2 sorbent proceeds by the following reaction steps.

$$SO_2 \text{ (g)} + \text{M-O} \quad \rightarrow \quad SO_3^{2-}\text{—M} \quad\quad\quad (5)$$

$$SO_2 \text{ (g)} + \text{M-OH} \quad \rightarrow \quad HSO_3^-\text{M} \quad\quad\quad (6)$$

$$SO_3^{2-}\text{—M} + :NH_2 \quad \rightarrow \quad \text{M} + SO_3^{2-}\text{-}NH_2\text{-} \quad\quad\quad (7)$$

$$HSO_3^-\text{M} \quad \rightarrow \quad \text{M} + HSO_3^-\text{-}NH_2\text{-} \quad\quad\quad (8)$$

SO_2 reacts with oxygen on the oxide surface to form sulfite SO_3^{2-} and bisulfate HSO_3^- products [41-42], steps (5) and (6), followed by adsorption to the amine active site in steps (7) and (8). The reaction scheme is in agreement with that observed during the NO adsorption study, the surface oxidation of NO to NO_2^- with the appearance N_2O_4 followed by absorption at the amine active site ($NO_2^-NH_2$-).

4.2.3   UV-Vis Spectra of 1,3-phenylenediamine

Figure 4-12 presents the UV-Visible diffuse reflectance spectra of (a) ethanol, (b) 2 vol % 1,3-phenylenediamine, and (c) 10 vol % 1,3-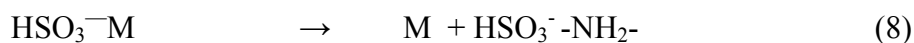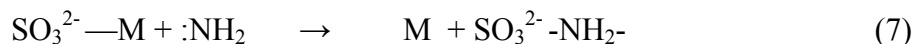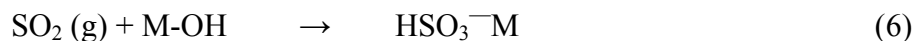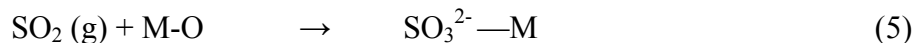phenylenediamine solution. A broadband at 400-550 nm, in the visible region, for the 2 vol % 1,3-phenylenediamine solution is due to π electron conjugation in adjacent aromatic molecules [43-45]. The 10 vol % solution shows an increase in the broadband absorbance intensity, in Figure 4-12(c), corresponding to a greater amount of conjugated π electrons in solution. The linear increase in absorbance intensity shows the proportionality of intensity to concentration and can be used as a measure for the presence of a highly conjugated molecular structure [46].

Figure 4-13 shows the UV-Visible diffuse reflectance spectra during the adsorption of CO_2, NO, and SO_2 gases on 1,3-phenylenediamine/SiO_2 sorbent at 323 K. The UV-Visible absorbance spectrum was placed in Kubelka-Munk units to investigate the changes in the adsorbate surface concentrations during the adsorption process [47]. The basis for the choice of the Kubelka-Munk function is to highlight the changes in surface concentration of an "adsorbate on a solid" system which would have otherwise not visible in the UV-Visible diffuse reflectance absorbance spectrum.
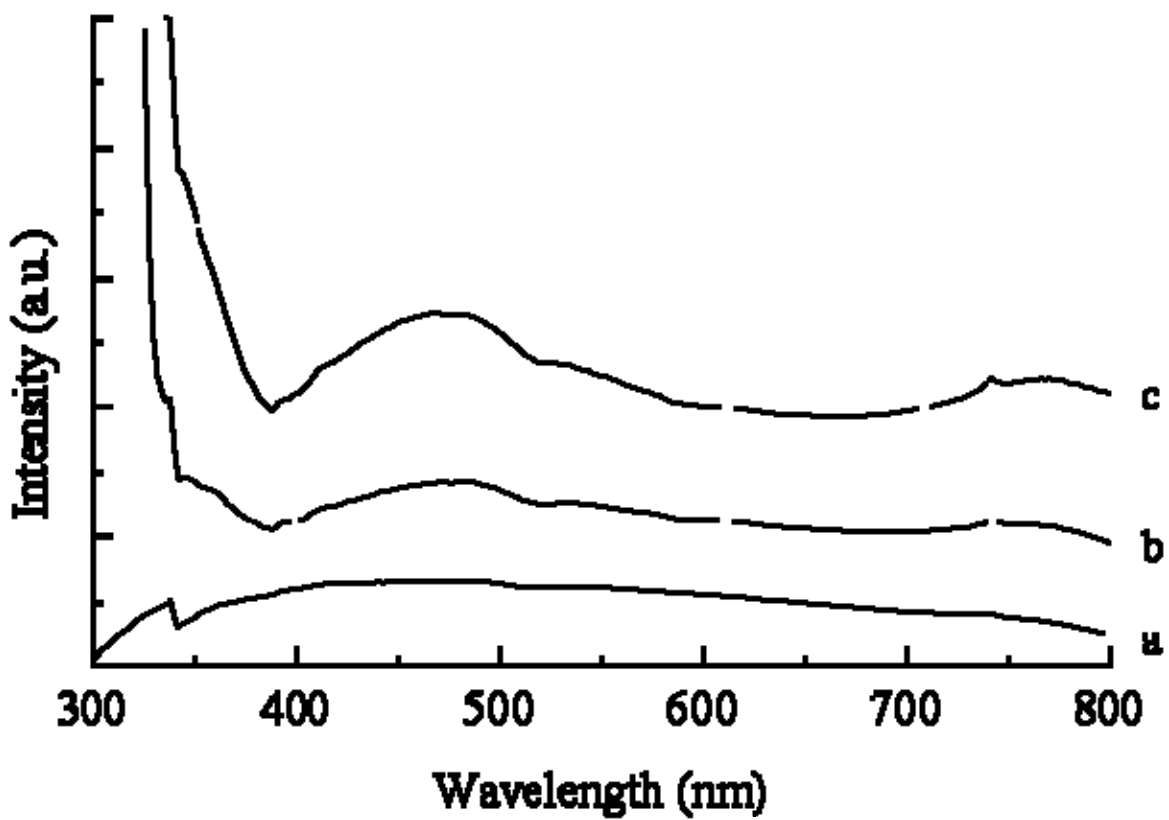
Figure 4-12   UV-Visible diffuse reflectance spectra of (a) ethanol, (b) 2 vol % 1,3-phenylenediamine/ethanol solution, and (c) 10 vol % 1,3-phenylenediamine/ethanol solution.
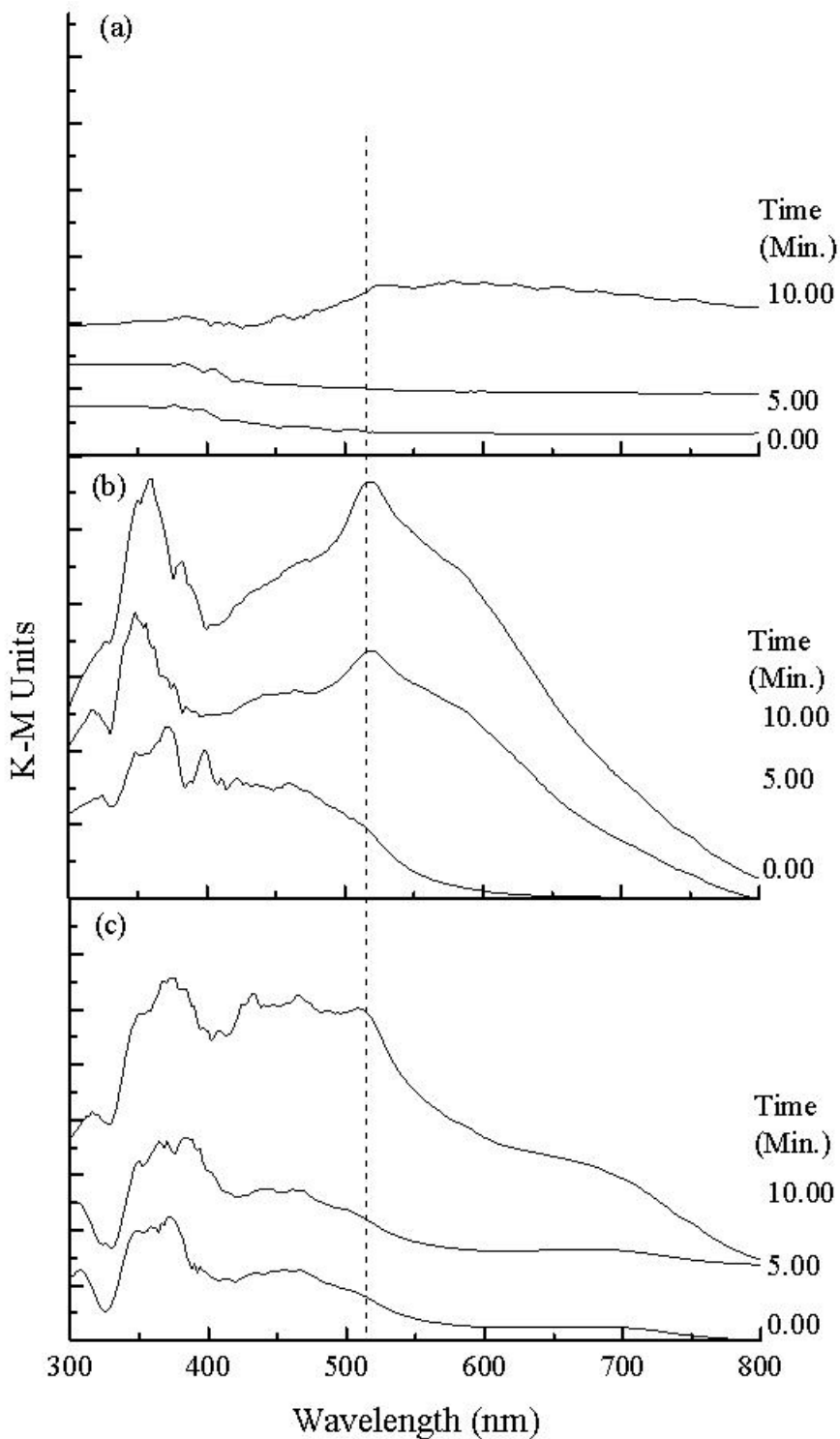
Figure 4-13 UV-Visible diffuse reflectance spectra of 1,3-phenyelediamine/SiO_2 during adsorption of (a) CO_2, (b) NO, and (c) SO_2 at 373 K.
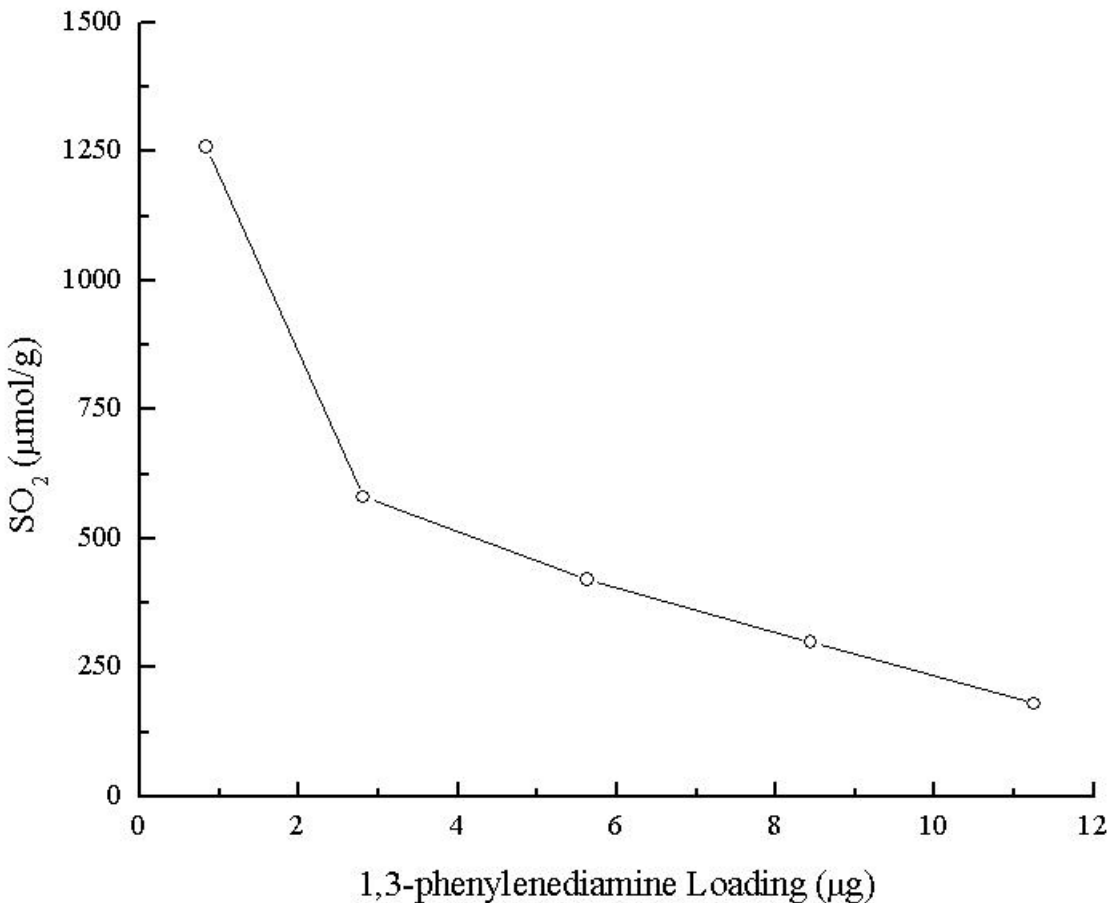
Figure 4-14   Analysis of SO_2 adsorption capacity based on 1,3-phenylenediamine loading on SiO_2.

Flowing CO_2 (pK_a = 6.35) over the sorbent, in Figure 4-13(a), results in a slight increase in K-M absorbance intensity. The slightly lower reflectivity (i.e. increase in K-M absorbance intensity) is attributed to weak CO_2 and 1,3-phenylenediamine interaction on the SiO_2 surface. Flowing gaseous NO and SO_2 (pK_a = 1.81) over the sorbent results in a strong broadband adsorption between 400-650 nm after 5 min exposure time to gaseous NO and 10 min exposure to SO_2. The increase in absorbance intensity and broadening is attributed to the effects of adsorption (cation formation) and a higher concentration of 1,3-phenylenediamine on the SiO_2 surface from agglomeration of newly formed adsorbate surface species [48]. Adsorbing NO exhibits a higher rate of agglomeration evidenced by the large and broader intensity after 5 min exposure time in comparison to SO_2 shown in Figure 4-13 b-c. The observations suggest the 1,3-phenylenediamine sorbent becomes mobile on the SiO_2 surface in the cationic state in the presence of an acidic reactant gas.

The adsorption of aromatic amine on SiO_2 result from the interactions of the π-electrons with the terminal SiO_2 silanol groups thus heterocyclic molecules such as 1,3-phenylenediamine are bound less strongly on silica than on alumina [49]. The heat of adsorption of aromatic hydrocarbons is decreased with increasing adsorbate loading [50] and at the higher 1,3-phenylenediamine loading, observed 1,3-phenylenediamine behavior in the presence of gaseous NO and SO_2 suggest the adsorbate layer becomes mobile through agglomeration. Low adsorbate coverage minimizes adsorbate-adsorbate interactions and thus adsorbate mobility is reduced.

The 0.0026 wt % 1,3-phenylenediamine/SiO_2 sorbent adsorbed 1260 mol/g of SO_2, shown in Figure 4-13. Interestingly, increasing the amine loading on SiO_2 results in a decrease in adsorption capacity; the limitation in SO_2 adsorption may be related to the (i) low surface area of the support material and poor dispersion of 1,3-phenylenediamine, and (ii) deactivation by SO_2 poisoning. The poisoning effects were investigated using ATR-IR spectroscopy by depositing 4 μm amine thin film on a ZnSe window. The SO_2 TPD study show for each adsorption/desorption cycle there is a decrease in SO_2 capture capacity from 16.0 to 8.52 μmol SO_2 after the fourth cycle, shown in Table 4-3. Re-dissolving the amine thin film in ethanol resulted in an increase in adsorption capacity to 14.6 μmol SO_2 (see Table 4-3). The enhancement effect on SO_2 capture by ethanol suggests that the 1,3-phenylenediamine is re-dispersed on the ZnSe window. The apparent poisoning effect on SO_2 adsorption may be the result of agglomeration of the amine active sites deactivating the adsorption capacity of the sorbent.

Regeneration of the 1,3-phenylenediamine thin film and SiO_2 supported sorbent resulted in deactivation of the SO_2 adsorption capacity, shown in Table 4-3 and Figure 4-14 respectively, as a result of agglomeration of the 1,3-phenylenediamine molecules. The addition of PEG to the 1,3-phenylenediamine/SiO_2 sorbent enhanced SO_2 adsorption capacity. In the presence of PEG, increased 1,3-phenylenediamine loading resulted in an increase in SO_2 adsorption capacity, shown in Table 4-4. Increasing the PEG content from 0.1 to 3.3 wt % increased SO_2 adsorption capacity from 0.26 to 2.22 mmol/g, a factor of 8.5 times.

SO_2 liberation from an absorbent as well as SO_2 capture is an important step for SO_2 management by adsorption in the power generation sector. PEG limits the migration area providing a barrier to the preferential migration mechanism for agglomeration and resulting deactivation. The sorbents capture capacity increased during PEG addition; PEG effectively disperses the 1,3-phenylenediamine on the SiO_2 surface as depicted in Figure 4-15.

Table 4-3   SO$_2$ adsorption on 4 µm think film of 1,3-phenylenediamine

Cycle	SO$_2$ (µmol)	SO$_2$(µmol)/ Amine(µmol)
1	16.0	0.82
2	14.2	0.73
3	10.1	0.58
4	8.52	0.42
Add ethanol	14.6	0.75

Table 4-4   SO$_2$ adsorption on 1,3-phenylenediamine+PEG/SiO$_2$ sorbent.

1,3-phenylenediamine (wt %)	PEG (wt %)	SO2 (mmol/g)
10	0.1	0.26
30	0.1	0.67
50	0.1	0.80
10	3.3	2.22
30	3.3	2.10
50	3.3	2.30

(a)

(b)
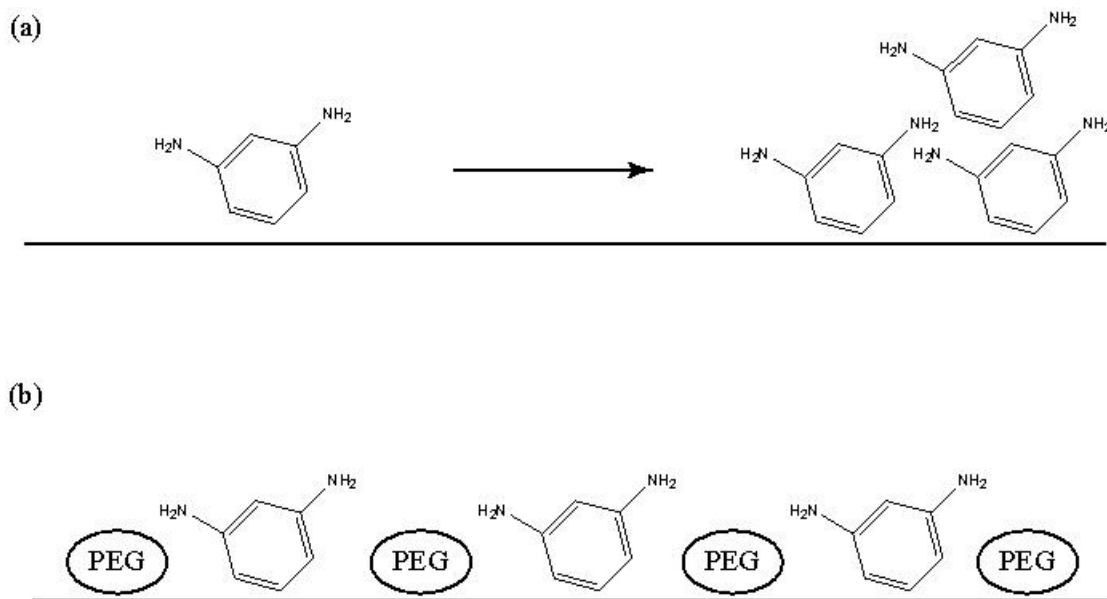
Figure 4-15   Proposed (a) agglomeration of aromatic amine and (b) immobilization of aromatic amine by polyethylene glycol.

4.2.4   Conclusion

Changes in the adsorbate layer by agglomeration of the aromatic amine molecules were observed during SO_2 adsorption process.   Under high amine loadings, agglomeration of the amine active sites results in a decrease in SO_2 adsorption capacity.   The optimum SO_2 sorbent preparation with the 1,3-phenylenediamine on SiO_2 is achieved by dispersing and immobilizing the amine active sites.   Improving the 1,3-phenylenediamine sorbent is achieved by preventing agglomeration of the amine active sites by the use of PEG as an effective dispersing agent.

4.3   In-situ IR study of the role of PEG in stabilizing silica-supported amine for CO_2 capture

This study shows that that the OH of PEG disperses the TEPA molecule on the SiO_2 surface, slowing down the oxidative degradation.

4.3.1 Results and discussion
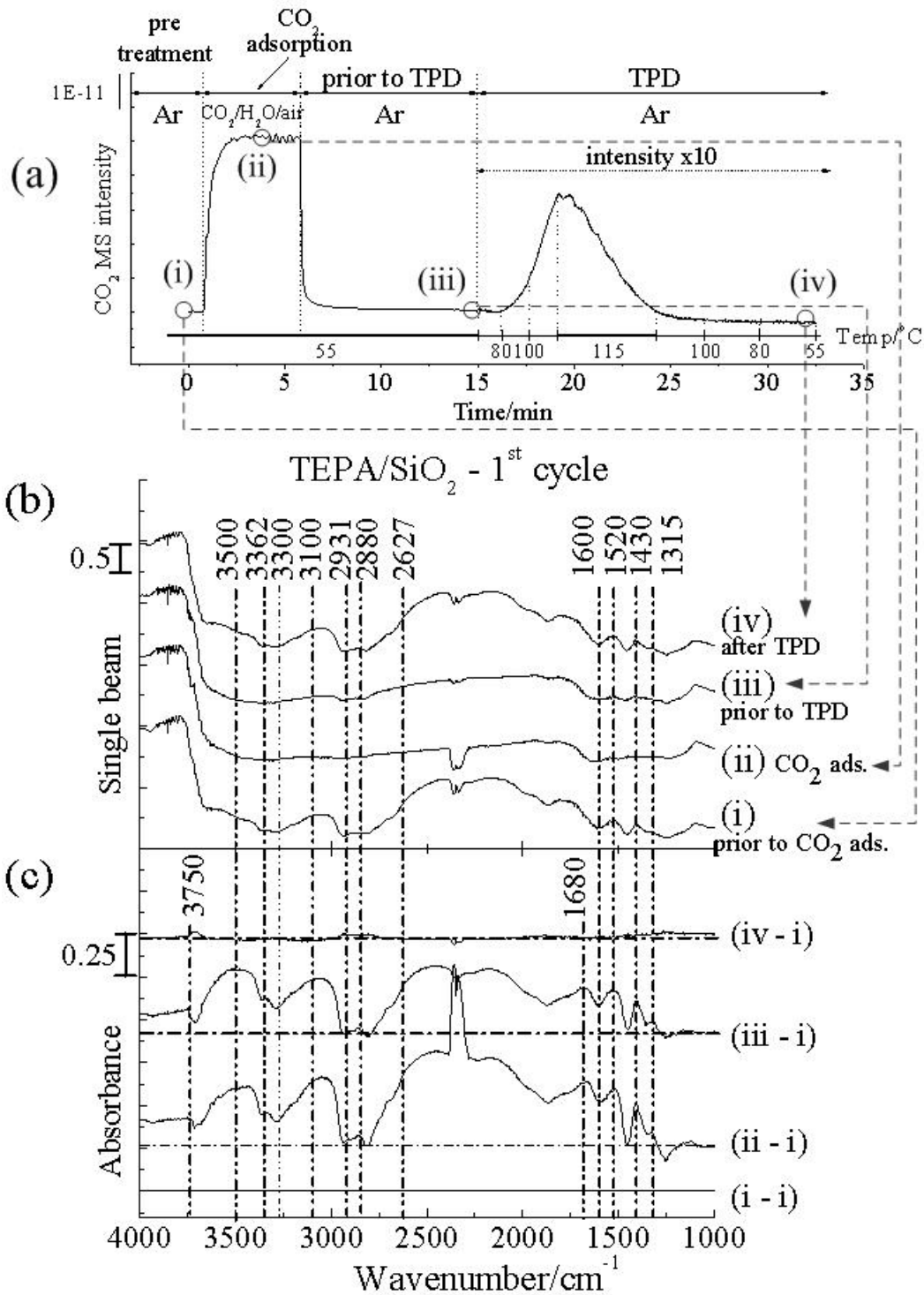
Figure 4-16(a) shows the CO_2 MS profile of the 1st CO_2 capture cycle consisting of (i) pretreatment of TEPA/SiO$_2$ by exposing to 150 cm^3/min of Ar flow at 115 ^{o}C and cooling down to 55 ^{o}C, (ii) CO_2 adsorption by flowing over the sorbent with 150 cm^3/min of CO_2/H$_2$O/air (15

vol% CO_2, 4 vol% H_2O, and balance air) at 55 ^{o}C for 5 min, (iii) removing weakly adsorbed CO_2 by switching back to Ar flow, and (iv) performing TPD (i.e., temperature-programmed desorption) and holding at 115 ^{o}C for 5 min to regenerate the sorbent by removing strongly adsorbed CO_2.
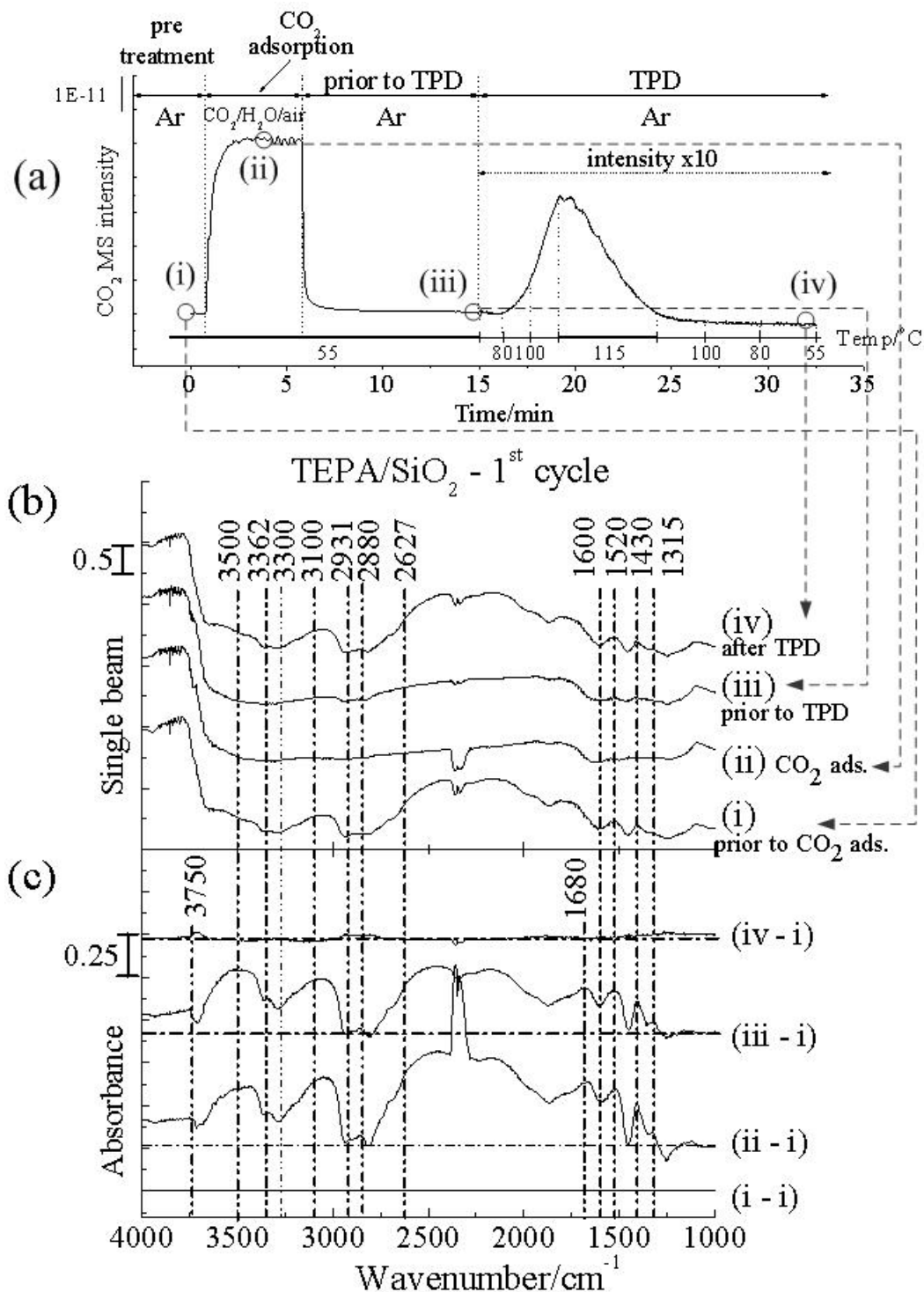
Figure 4-16 (b) shows the IR single beam taken at the specific steps during the 1st CO_2 capture cycle. The single beam spectra obtained from DRIFT are equivalent to the transmission IR spectra. The single beam of TEPA/SiO_2, spectrum (i) in Figure 4-16 (b), prior to CO_2 adsorption exhibited IR characteristics of TEPA and SiO_2. The key features of this spectrum are N-H stretching vibration bands at 3362 and 3300 cm^{-1}, C-H stretching band at 2931 and 2880 cm^{-1}, N-H deformation of primary amine at 1600 cm^{-1} and the sharp absorption at 3750 cm^{-1} due to unassociated Si-OH of SiO_2. The single spectrum in the 3750 cm^{-1} exhibited a sharp decrease in absorbance, followed by a gradual decrease in the 3500 cm^{-1} region. These features are characteristics of SiO_2 which contain surface OH and H_2O.[51] Table 4-5 summarizes IR band assignments presented in this work.

Flowing CO_2/H_2O/air over the TEPA/SiO_2 caused (i) CO_2 MS intensity in Figure 4-16 (a) to increase and (ii) strong IR absorption in 3700 to 3000 and 1500 to 1300 cm^{-1} regions shown in the single beam spectrum (ii) in Figure 4-16 (b), indicating the adsorption of CO_2 occurred on TEPA/SiO_2. The changes in single beam spectra can be discerned by the absorbance spectra shown in Figure 4-16 (c) which were obtained using the spectrum taken prior to CO_2 adsorption as the background spectrum. Absorbance spectrum during CO_2 adsorption, (ii-i) in Figure 4-16 (c), exhibits strong absorbance intensity in 1500 to 1300 cm^{-1} region. Absorbance spectra reveal an additional band at 1680 cm^{-1} which could be assigned to C=O stretching for carbamic acid.[52]

Figure 4-16   (a) CO_2 MS profile during the 1st cycle of CO_2 over TEPA/SiO_2 (b) IR single beam spectra and (c) corresponding IR absorbance. Absorbance is obtained by Abs. = $\log(I_0/I)$ = $-(\log(I) - \log \log(I_0))$, where I is single beam spectra taken at different stage during CO_2 capture and I_0 is single beam taken prior to CO_2 adsorption.

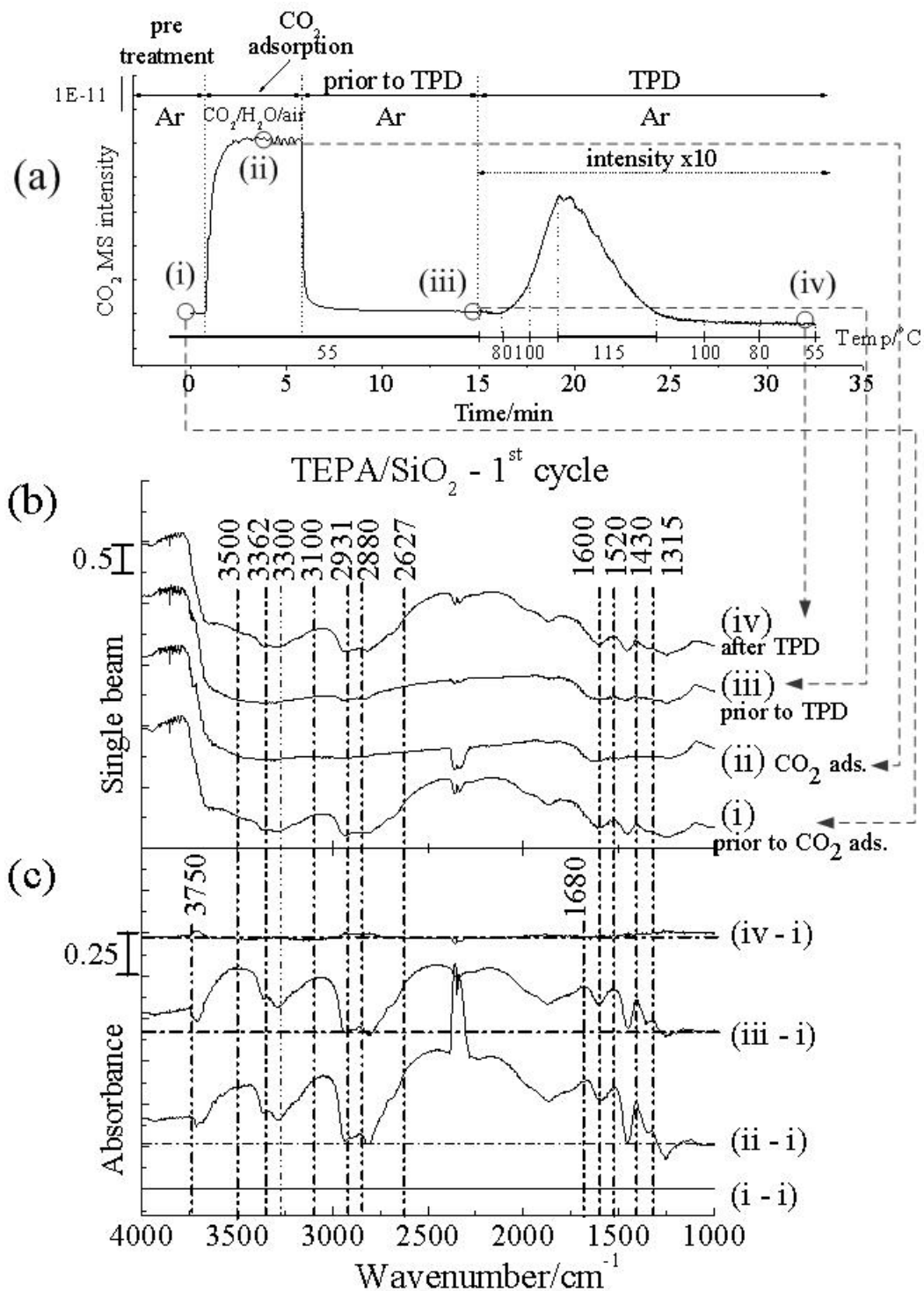A small increase in the intensity of the 3750 cm^{-1} region along with those in 3500 cm^{-1} in Figure 4-16 (c) indicates the H_2O content of the sorbent particle increased upon flowing $CO_2/H_2O/air$. The IR band around 3500 cm^{-1} region can be attributed to the O-H stretching; the band around 3100 cm^{-1} to N-H stretching; the broad band at 2627 cm^{-1} to NH_2-O. These bands which arose from CO_2 adsorption are closely related to hydrogen bonding between an O of CO_2 and H of NH_2 of the amine. The strong IR band at 1520 cm^{-1} could be assigned to carbamate; the 1430 cm^{-1} band to carboxylate species; the 1315 cm^{-1} band to $NCOO^-$. The presence of these bands indicate the formation of both carbamate and carboxylate species. Carbamate and carboxylate species have been known to be produced from the reaction between an amine and CO_2 in the presence of H_2O.[2,52-53]

Switching the flow from $CO_2/H_2O/air$ to Ar causes the CO_2 MS intensity to sharply drop to baseline. Corresponding single beam spectrum (iii) in Figure 4-16(b) and absorbance spectrum (iii-i) in Figure 4-16 (c) show more of a decrease in the NH_2-O band intensity than the carboxylate and carbamate band intensities, further confirming the presence of two different types of species[54]: (i) species adsorbed through hydrogen bonding, $-NH_2$-O_2C and (ii) carbamate and carboxylate species formed through N-C bond between N of amine and C of CO_2. The latter appears to have higher binding energy than the former.

The Temperature-Programmed Desorption (TPD) was performed by heating the DRIFT cell from 55 to 115 ^{o}C at 20 ^{o}C/min then held at 115 ^{o}C for 5 min and followed by cooling down to 55 ^{o}C at 10 ^{o}C/min under 150 cm^3/min of Ar. The CO_2 MS profile produced during TPD was magnified and plotted with its corresponding temperature in Figure 4-16 (a). The CO_2 MS profile began to rise at 70 ^{o}C, and continued to rise until reaching the maximum at 115 ^{o}C. CO_2 started to decrease after holding at 115 ^{o}C for 5 min and reach the baseline during the cooling down period, indicating the completion of CO_2 desorption. Single beam spectrum obtained after TPD, (iv) in Figure 4-16 (b), exhibits similar features to that of spectrum (i) in Figure 4-16 (b), suggesting the nearly complete removal of adsorbed CO_2 species from the sorbent. This is further verified by flat absorbance spectra (iv-i) presented in Figure 4-16 (c).

Figure 4-17 (a) shows the details of the normalized CO_2, N_2, and O_2 MS profiles during the switching from Ar to $CO_2/H_2O/air$, corresponding to CO_2 adsorption in the 1st cycle of CO_2 capture over TEPA/SiO_2 in Figure 4-16 (a). The immediate rise of O_2 and N_2 profiles upon switching suggests the absence of their adsorption onto the sorbent. Adsorption of CO_2 resulted in a small delay in the CO_2 MS profile. The concentration of CO_2 quickly rises to saturation after 2 min from the switching. This CO_2 breakthrough curve can be converted to the CO_2 uptake ($F_{uptake,CO2}$) by subtracting the contribution from flow pattern of N_2 and O_2. Since adsorption of N_2 and O_2 is negligible, N_2 and O_2 are the accurate representation of the residence time distribution of the species flowing through the DRIFT cell and its inlet and outlet lines. The inset shows the corresponding CO_2 uptake profile, which adsorption half time ($\tau_{0.5}$) was determined to be 0.28 min (16.8 s). Small adsorption half time suggests rapid kinetics of CO_2 adsorption[53,55-57] which allows high utilization of the sorbent.[58]

Table 4-5   IR band assignments

Wavenumber (cm^{-1})	Assignment	Species		Ref.
1315	NCOO vibration	carboxylate, carbamate		[13,53,59]
1430	COO$^-$ vibration	carboxylate		[52,59-61]
1520	C=O stretching	carbamate		[53,62]
1600	N-H deformation of primary amine	TEPA		[1,21]
1680	C=O stretching	carbamic acid		[52]
2627	NH-O stretching	CO_2-H_2N-		[63]
2880	C-H stretching	TEPA, PEG		[13,21]
2931	C-H stretching	TEPA, PEG		[13,21,52]
3100	N-H stretching	TEPA		[53]
3300	N-H stretching	TEPA		[13,21,64]
3362	N-H stretching	TEPA		[5,21,53,65]
3500	O-H stretching	carboxylate,	PEG, TEPA	[21,52-53]
3750	Unassociated Si-OH	SiO_2		[52,60]
3700-3000	hydrogen bonding	carboxylate,	PEG, TEPA	[52,56,58,60,64]
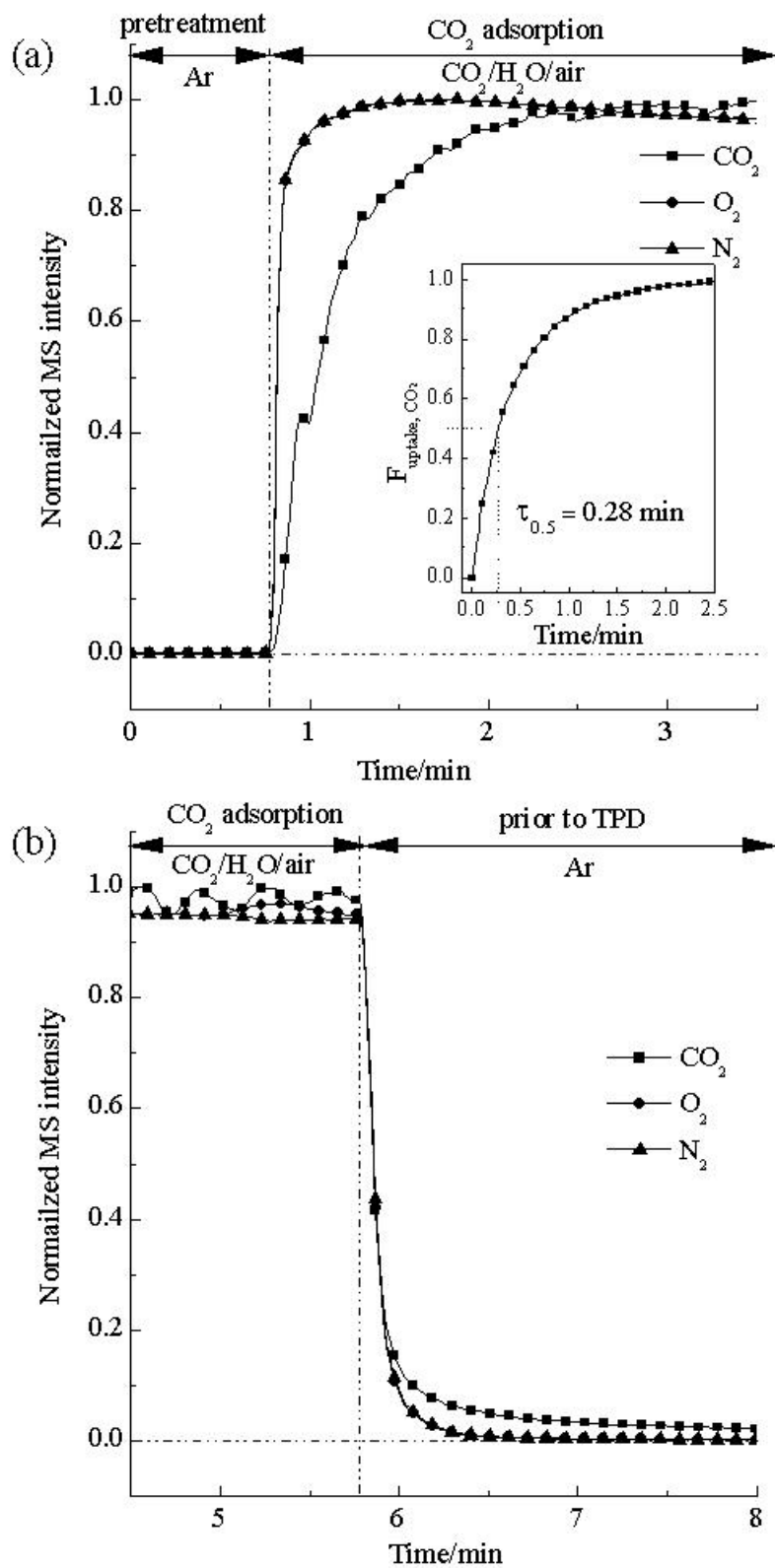
Figure 4-17　MS profiles of CO_2, N_2, and O_2 during the 1st cycle over TEPA/SiO$_2$ (a) switching from Ar to $CO_2/H_2O/air$ and (b) switching from $CO_2/H_2O/air$ to Ar.

Table 4-6 shows the corresponding adsorption half time obtained at the 1st and 30th cycle over TEPA/SiO$_2$ and PEG/TEPA/SiO$_2$. A significant increase in adsorption half time was observed in both sorbents, indicating the slow uptake of CO_2. The slow CO_2 uptake could be attributed to the diffusion limitation which is shown later by the IR evidence of accumulating TEPA and PEG species on the surface of the sorbent particles. Figure 4-17 (b) shows the sharp drop of O_2 and N_2 profiles at the switching from CO_2/H_2O/air to Ar, which further confirms that their adsorption did not take place on the sorbent. The trailing CO_2 profile suggests the continuous desorption of weakly adsorbed CO_2 and gradual diffusion of the desorbed CO_2 species from TEPA/SiO$_2$.

Table 4-6 CO_2 adsorption half time during the 1st and 30th cycle over TEPA/SiO$_2$ and PEG/TEPA/SiO$_2$.

Sorbent	$\tau_{0.5}$ (s)	
	1st cycle	30th cycle
TEPA/SiO$_2$	16.8	20.4
PEG/TEPA/SiO$_2$	12.6	19.2
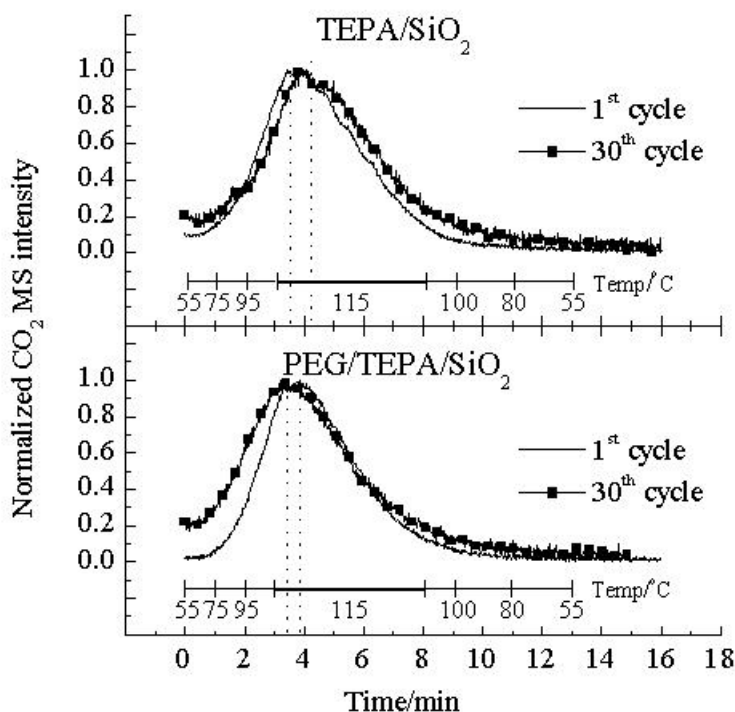
Figure 4-18 Normalized CO_2 MS profile during TPD of the 1st and 30th cycle over TEPA/SiO$_2$ and PEG/TEPA/SiO$_2$.

Figure 4-18 shows the normalized CO_2 MS profile during TPD of the 1st and 30th cycle of both sorbents. The peak of desorption falls under constant desorption temperature of 115 ^{o}C in

all cases. The desorption peak on $TEPA/SiO_2$ shifted to the right (i.e., high binding energy) as the sorbent degraded at the 30th cycle. In contrast, the CO_2 profile over $PEG/TEPA/SiO_2$ shifted to the left (i.e., low binding energy).

Table 4-7 summarizes the CO_2 capture capacity of $TEPA/SiO_2$ and $PEG/TEPA/SiO_2$ at the 1st and 30th cycle. The weakly adsorbed CO_2 was determined by CO_2 trailing after switching the flow from CO_2/air to Ar. The strongly adsorbed CO_2 was determined from the desorbed CO_2 during TPD. Weakly adsorbed CO_2 contributed roughly 20% of the total adsorbed CO_2 (weakly + strongly adsorbed) on the sorbents except those in the 1st cycle over $PEG/TEPA/SiO_2$ which weakly adsorbed CO_2 contributed only 5% of the total adsorbed CO_2.

Table 4-7 CO_2 capture capacity of $TEPA/SiO_2$ and $PEG/TEPA/SiO_2$ during the 1st and 30th cycle of CO_2 capture

| Sorbent | CO_2 capture capacity (mmol-CO_2/g-sorb.) | | | |
| | 1st cycle | | 30th cycle | |
	weakly ads.	strongly ads.	weakly ads.	strongl y ads.
$TEPA/SiO_2$	445.80	2087.46	234.73	871.85
$PEG/TEPA/SiO_2$	45.05	1110.46	99.22	445.14
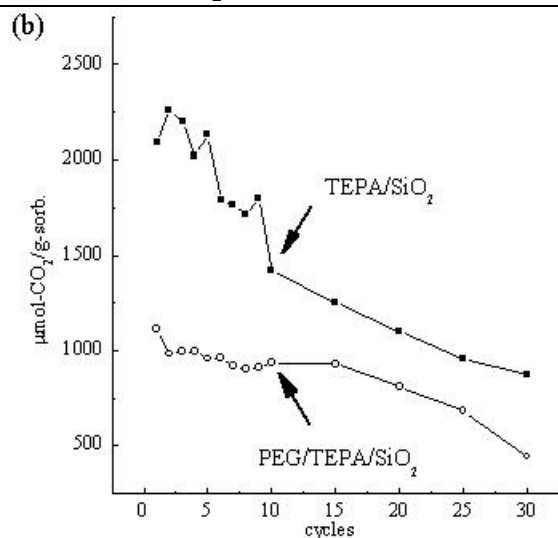
Figure 4-19 (a) provides an overall picture of CO_2 MS profile during the 30 cycles of CO_2 capture over $TEPA/SiO_2$ and $PEG/TEPA/SiO_2$. Figure 4-19 (b) plots the CO_2 capture capacity of each sorbent versus the number of cycles. It is important to note that both sorbents did not exhibited appreciable degradation in the first 5 cycles. After the first 5 cycles, $PEG/TEPA/SiO_2$ degraded significantly slower than $TEPA/SiO_2$. This observation suggests that less than 5 cycles of testing is not sufficient for evaluating the stability of the sorbent.

Figure 4-20 (a) shows single beam spectra during the 30th cycle of CO_2 over $TEPA/SiO_2$. The IR characteristic bands at the 30th cycle gave higher intensity than that of the 1st cycle shown

in Figure 4-16 (b), suggesting the accumulation of the strongly adsorbed species on the sorbent surface. Strong IR absorption in 3700 to 3000 cm^{-1} observed in all single beam spectra can be attributed to (i) the increase in the H_2O content on the sorbent and (ii) the increase in hydrogen bonding interaction between the accumulated adsorbed CO_2 species and NH_2/NH group of
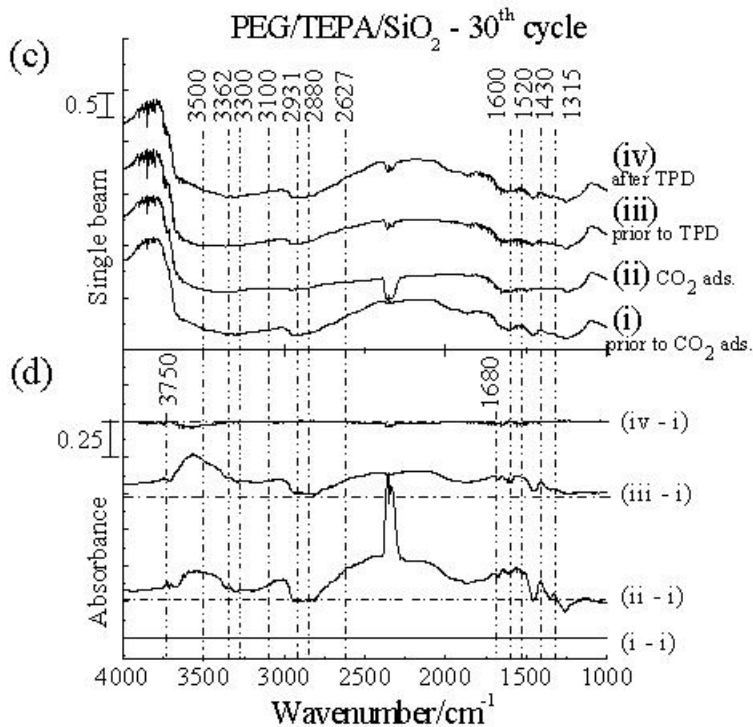
TEPA.

Figure 4-21 (a)-(d) show single beam and absorbance spectra during the 1st and 30th cycle over PEG/TEPA/SiO$_2$. The spectra produced during the 1st CO$_2$ capture cycle shown in Figure 4-21(a) resembled those obtained from TEPA/SiO$_2$ shown in Figure 4-16 (b). Addition of PEG causes (i) strong absorption in CH stretching at 2931 and 2880 cm^{-1} due to the presence of CH groups in PEG and (ii) decrease the sharpness of NH stretching at 3362 and 3300 cm^{-1} due to increase in hydrogen bonding between NH_2/NH of TEPA and OH of PEG. Absorbance spectra (ii-i) and (iii-i) of PEG/TEPA/SiO$_2$, shown in Figure 4-21 (b), exhibit lower absorbance intensities in the 3750 to 3500 cm^{-1} region than those of TEPA/SiO$_2$ in Figure 4-21 (c), suggesting that PEG may cause the reduction in H_2O content on the PEG/TEPA/SiO$_2$ sorbent.
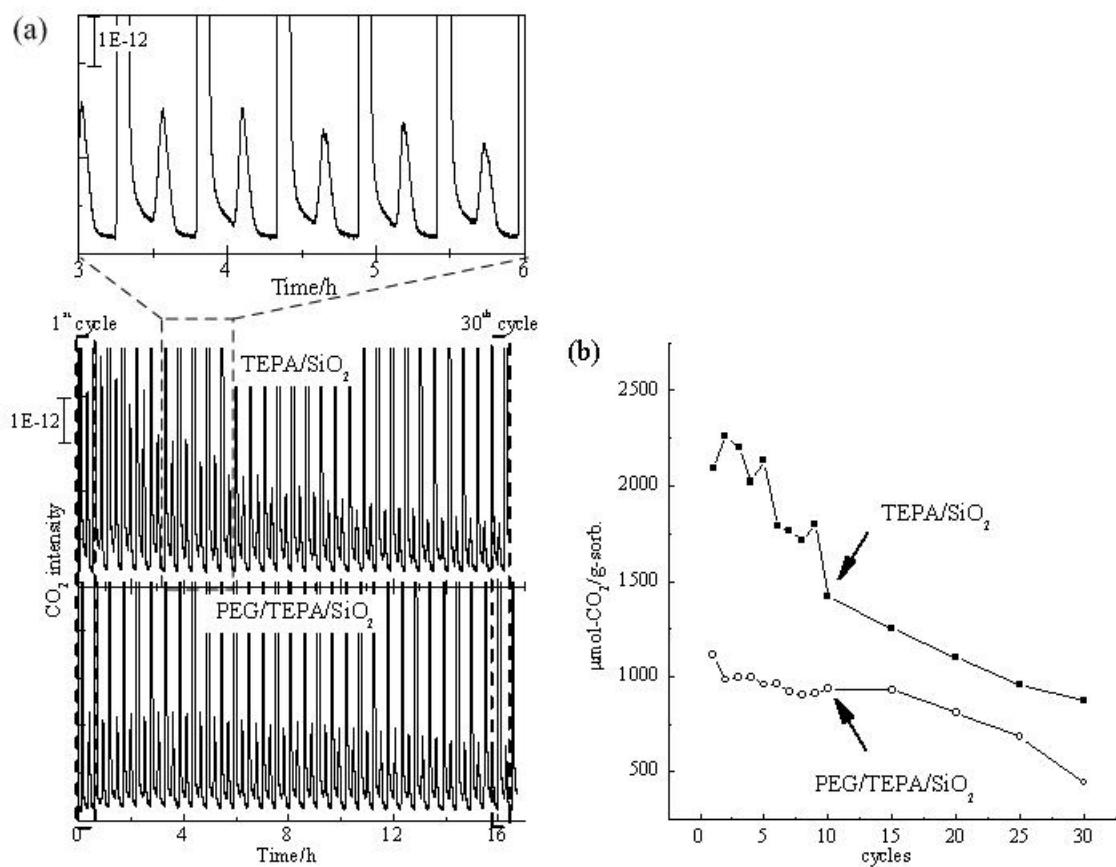
Figure 4-19   (a) CO_2 MS profile obtained during 30 cycles of CO_2 capture over TEPA/SiO$_2$ and PEG/TEPA/SiO$_2$. (b) CO_2 capture capacity of the sorbents.
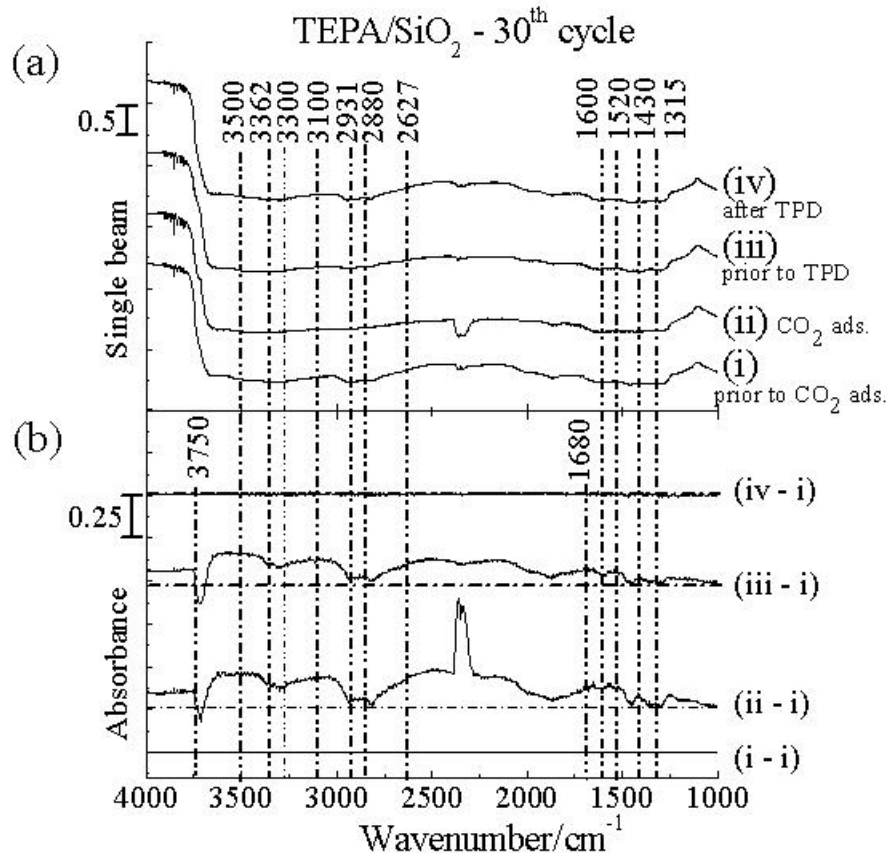
Figure 4-20   (a) IR single beam spectra and (b) IR absorbance over TEPA/SiO$_2$ during the 30th cycle of CO$_2$ capture.

Comparison of Figure 4-20 and Figure 4-21 that PEG/TEPA/SiO$_2$ produced lower intensities at 1520, 1430, and 1315 cm^{-1} than those of TEPA/SiO$_2$, indicating PEG decreases the formation of carboxylate and carbamic species.   This trend Fcan be further discerned by examining Figure 4-22 (a) and (b) which show the IR absorbance spectra obtained by subtracting single beam spectra prior to CO$_2$ adsorption at the 1st cycle from that of the 10th, 20th, and 30th cycle over TEPA/SiO$_2$. The increase in absorbance intensity at 1430 cm^{-1} can be attributed to the formation of a carboxylate species.[1,59] The inter-conversion of carbamate and carboxylate has been well established in oxidative carbonylation chemistry. Conversion of carbamate, (-NH-COOH) to carboxylate (-NH$_2$ + -COO-) would lead to the formation of NH$_2$. This step is supported by the growth of both carboxylate and N-H stretching at 3300 and 3362 cm^{-1}. The spectra in Figure 4-22 (b) are magnified 5 times for comparison with the spectra presented in Figure 4-22 (a).   The   spectra in the carbamate and carboxylate region show that PEG significantly slowed down the growth of these bands. Figure 4-22 also shows the increase in the intensity of the broad H$_2$O band at 3600 cm^{-1} on both sorbent. A separate IR study of TEPA/PEG/SiO$_2$, which compared the IR spectra of sorbent with various loading of TEPA and PEG, shows that the intensity of OH and H$_2$O bands in the 3750 - 3500 cm^{-1} region decreased

55

with increasing TEPA/PEG loading. The growth of this band may indicate the loss of TEPA/PEG species via evaporation.
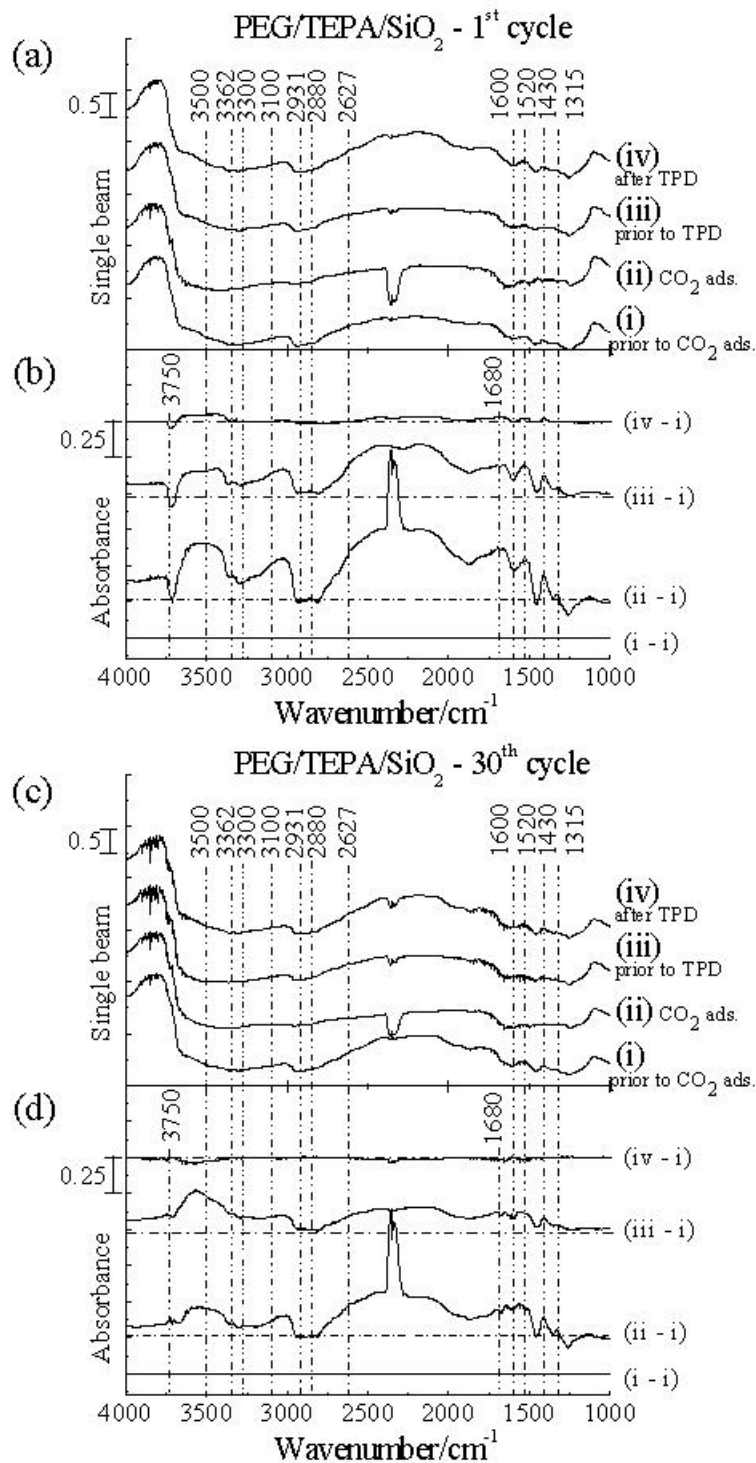
Figure 4-21 IR single beam spectra and corresponding IR absorbance over PEG/TEPA/SiO$_2$ during (a) and (b) the 1st cycle of CO$_2$ capture, (c) and (d) the 30th cycle.
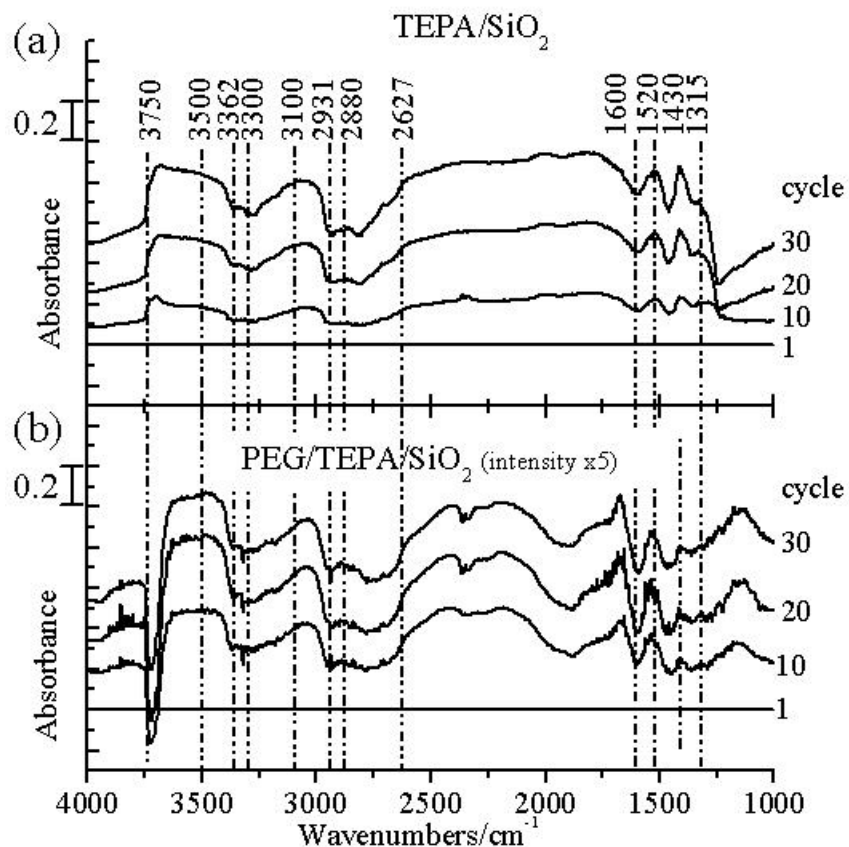
Figure 4-22 IR absorbance spectra obtained prior to CO_2 adsorption at 10th, 20th, and 30th cycle over (a) TEPA/SiO$_2$ and (b) PEG/TEPA/SiO$_2$. Absorbance is obtained by Abs. = $\log(I_0/I)$ where I is single beam taken prior to CO_2 adsorption at each cycle and I_0 is that of the 1st cycle.

Plotting CO_2 capture capacity with carboxylate intensity at 1430 cm^{-1} in Figure 4-23 (a) and (b) shows decreases in CO_2 capture capacity of TEPA/SiO$_2$ are related to increases in carboxylate intensity. The presence of PEG further slowed down the decrease in CO_2 capture capacity and the formation of carboxylate. We propose that the role of PEG can be attributed to its dilution effect. The molar ratio of PEG to TEPA of 1:6 resulted in such a dilution effect which blurred of the two distinct N-H stretching bands at 3300 and 3362 cm^{-1}, an indication of the formation of hydrogen bonding between NH of TEPA and OH of PEG. This dilution effect would isolate NH$_2$ and NH from neighboring TEPA, decreasing their interaction with CO_2 to form carbamate, a precursor to the stable carboxylate.
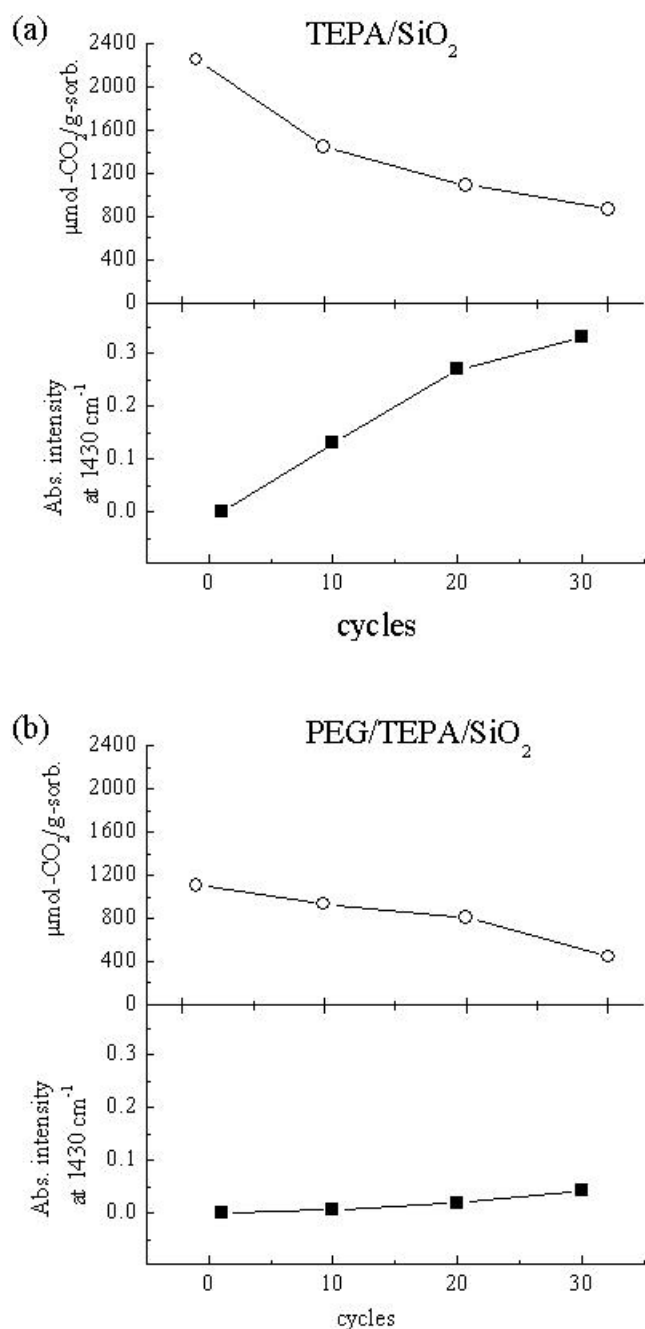
Figure 4-23 CO_2 capture capacity and absorbance intensity at 1430 cm^{-1} measured from spectra taken prior to TPD over (a) TEPA/SiO_2 and (b) PEG/TEPA/SiO_2.

4.3.2   Conclusion

The adsorbed CO_2 species produced from CO_2 capture at 55 ^oC can be classified as weakly adsorbed CO_2 and strongly adsorbed CO_2. The former is related to a hydrogen bonding species (i.e., NH_2-O) which exhibits IR absorption at 2627 cm^{-1}; the latter is associated with

carbamate at 1520 cm^{-1} and carboxylate species at 1430 cm^{-1}. PEG was found (i) to decrease the overall CO_2 capture capacity, the degradation rate of TEPA/SiO_2, and the adsorption half-time and (ii) to increase the fraction of weakly adsorbed CO_2 species.

The growth of the IR intensity of carboxylate on TEPA/SiO_2 and PEG/TEPA/SiO_2 during cyclic CO_2 processes is inversely proportional to CO_2 capture capacity. The stabilizing role of PEG on TEPA/SiO_2 can be attributed to hydrogen bonding between NH_2/NH of TEPA and OH of PEG. This hydrogen bonding interaction slowed down the formation of carbamate and its conversion to carboxylate – the species blocking amine sites for CO_2 capture.

4.4   In-situ Infrared study of the effect of HCl and H_2O on CO_2 adsorption on silica supported amine

HCl is one of the species present in the flue gas.   This study shows that HCl irreversibly adsorb on the surface of the solid amine.

4.4.1   Results and discussion

Figure 4-24(a) and (b) show the overall CO_2 MS profile and corresponding temperature over TEPA/SiO_2 during the HCl injection experiment.   Heating TEPA/SiO_2 during the pretreatment from 55 to 120 ^{o}C caused CO_2 to desorb from the sorbent. Pulsing 1 and 3 cm^3 of CO_2 for calibration resulted in small temperature spike, indicating minimal adsorption of CO_2. Switching Ar to CO_2/air during CO_2 adsorption in CO_2 cap.-1 caused the immediate rise in CO_2 MS profile and the temperature spike from adsorption temperature of 55 to 91 ^{o}C. The CO_2 MS intensity during CO_2 adsorption was not completely shown in the figure to preserve CO_2 MS profile feature during TPD. The temperature spike could be attributed to exothermic nature of the reaction between amine and CO_2. Switching the CO_2/air to Ar caused the immediate drop in CO_2 MS intensity followed by trialing. Raising the temperature of the sorbent from 55 to 135 ^{o}C during TPD caused CO_2 to desorb from TEPA/SiO_2. Desorption of CO_2 was completed before the sorbent was cooled down to 55 ^{o}C.

Injection of 10 μL HCl onto the sorbent after the CO_2 cap.-1 caused the temperature spike from 55 to 72 ^{o}C, indicating the exothermic reaction between HCl and TEPA. Subsequent CO_2 adsorption in CO_2 cap.-2 produced a smaller temperature spike compares to that observed in CO_2 cap.-1, suggesting the decrease in CO_2 adsorption activity of the sorbent. The decrease in CO_2 adsorption activity could be attributed to (i) elimination of the amine sites of TEPA due to reaction between HCl and TEPA which is further discussed in Figure 4-29. The TPD during CO_2 cap.-2 produced a smaller CO_2 desorption profile compared to that of CO_2 cap.-1, confirming the reduction in CO_2 capture capacity of TEPA/SiO_2. The second HCl injection, HCl-2, produced the similar temperature spike to that of the first injection. However, CO_2 adsorption in CO_2 cap.-3 did not produce significant temperature spike as those observed in the first 2 cycles, suggesting the majority amine sites of TEPA were reacted with HCl or removed by

H_2O from the SiO_2 surface. The TPD during CO_2 cap.-3 did not produce an observable desorbed CO_2 MS profile, indicating that TEPA/SiO_2 loss its CO_2 capture capacity after the 2nd HCl injection.

CO$_2$ MS profile and the corresponding temperature over TEPA/SiO_2 during H_2O injection experiment are presented in Figure 4-24c) and (d). The fresh sorbent underwent pretreatment and one CO_2 capture cycle similar to that during HCl injection experiment. Switching Ar to CO_2/air during CO_2 adsorption in all 3 CO_2 capture cycles produced temperature spikes which reduced with the increase in amount of H_2O injected to the sorbent. CO_2 MS profiles produced during TPD from 3 CO_2 capture cycles show the gradual decrease of desorbed CO_2 after each H_2O injection. The reduction in temperature spike during CO_2 adsorption and desorbed CO_2 during TPD were less than those observed in HCl injection experiment. Injecting 10 μL of H_2O during H_2O-1 and H_2O-2 caused the temperature of sorbent bed to drop from 55 to 44 ^{o}C and 47 ^{o}C, respectively. The decrease in bed temperature suggests the absence of exothermic reaction observed in HCl injection experiment. In comparison to HCl injection experiment, the decrease in CO_2 capture capacity in H_2O injection experiment could only be attributed to the removal of TEPA from the sorbent and sorbent agglomeration. CO_2 capture capacities of TEPA/SiO_2 from both experiments are listed in Table 4-8.
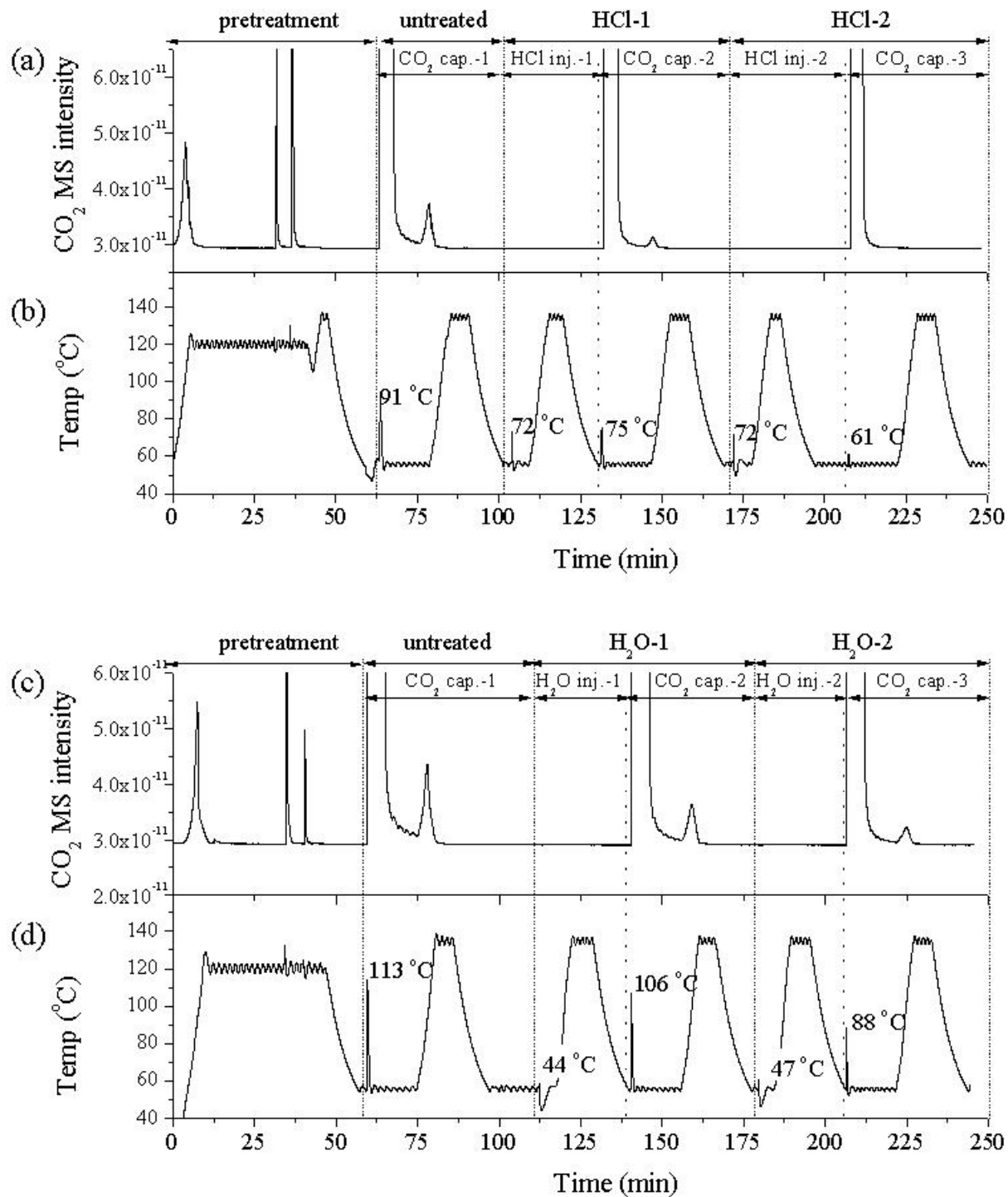
Figure 4-24. Overall CO_2 MS profile and temperature profile during HCl and H_2O injection.

Table 4-8. CO_2 capture capacity of TEPA/SiO$_2$ from HCl and H$_2$O injection experiments.

| | mmol-CO_2/g-sorb. | |
	HCl	H$_2$O
no injection	1.307	1.487
injection-1	0.310	1.019
injection-2	0.042	0.701
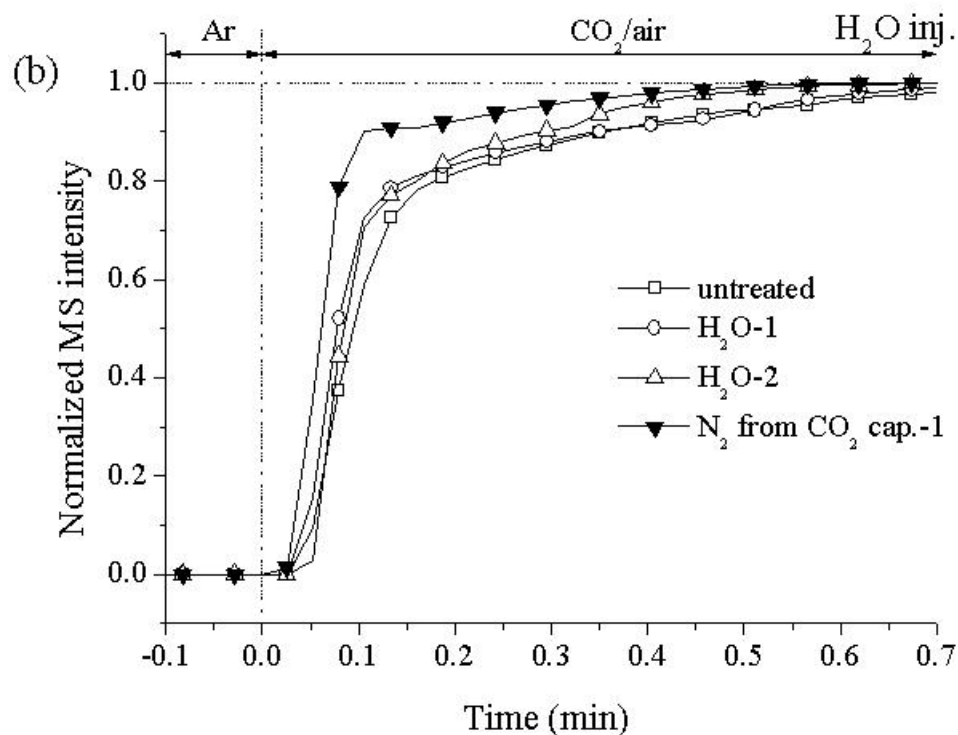
Figure 4-25(a) shows the CO_2 and N_2 MS profiles during the switching from Ar to CO_2/air over TEPA/SiO$_2$ from HCl injection experiment. CO_2 MS profiles from CO_2 cap.-1, -2, and -3 were plotted to compare the CO_2 adsorption profile between untreated and HCl treated TEPA/SiO$_2$ from HCl-1 and -2. Our previous study shows that N_2 does not adsorb on TEPA/SiO$_2$ [66], hence, N_2 MS profile can be used to represent the residence time distribution of the gas species flowing through DRIFT. N_2 MS profile during CO_2 adsorption of CO_2 cap.-1 from HCl and H$_2$O injection experiment was plotted as a reference Figure 4-25(a) and (b), respectively. CO_2 MS profiles showed in Figure 4-25 (a) quickly rise and reach the saturation after 0.7 min (42 s) upon switching from Ar to CO_2/air in all cycles. The CO_2 MS profiles gradually shift toward N_2 MS profile as amount of injected HCl increased, indicating the decrease in the CO_2 capture capacity of the sorbent Figure 4-25 (b) shows the N_2 and CO_2 MS profiles from H$_2$O injection experiment. CO_2 MS profiles show the less prominent shifting toward N_2 profile than those observed in HCl injection experiment, suggesting less decay in CO_2 capture capacity of the sorbent.

62
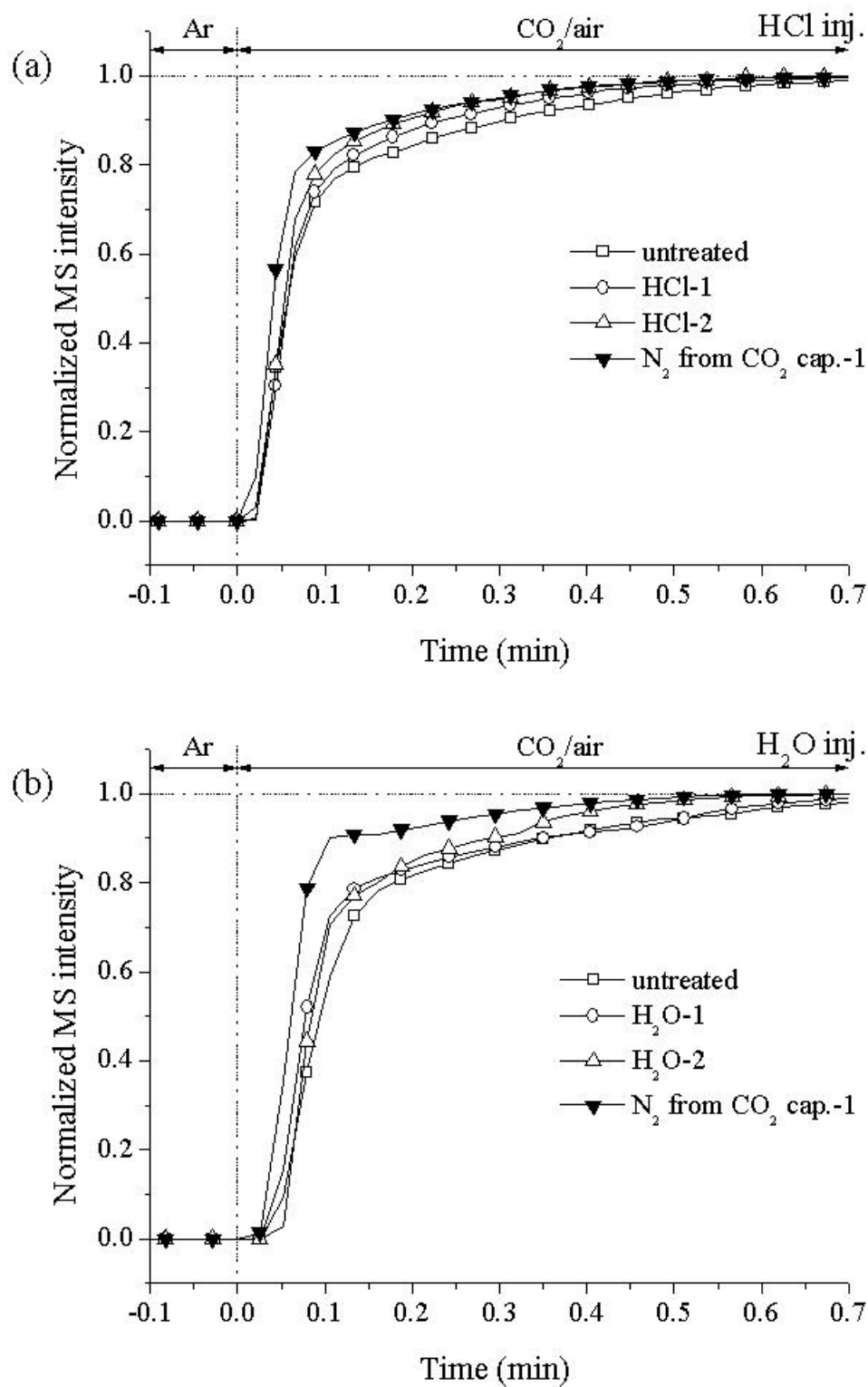
Figure 4-25. CO_2 and N_2 MS profiles during the switching from Ar to CO_2/air over TEPA/SiO_2 from (a) HCl injection and (b) H_2O injection experiments.

Figure 4-26 (a) shows the CO_2 MS profile during the TPD over the untreated TEPA/SiO$_2$, TEPA after the first HCl injection (HCl-1), and TEPA/SiO$_2$ after second HCl injection (HCl-2). CO_2 started desorbing as soon as the temperature was raise from 55 ^{o}C at the beginning of TPD in all cycles. The untreated TEPA/SiO$_2$ shows the largest desorption peak with CO_2 peak desorption temperature at 95 ^{o}C. Injecting 10 µL of HCl to the sorbent decreased the desorbed CO_2 and CO_2 peak desorption temperature of 90 ^{o}C compared to those observed from the untreated TEPA/SiO$_2$. Further injected 10 µL HCl to the sorbent reduced the desorbed CO_2 to almost unobservable with the corresponding CO_2 peak desorption temperature of 70 ^{o}C. The decrease in CO_2 desorption peak could result from the reduction in active sites for CO_2 capture from reaction between HCl and amine groups of TEPA.

Bonding energy between CO_2 and secondary amine, -NH-, is expected to be higher than that between CO_2 and primary amine, NH$_2$, as the secondary amine exhibits higher basicity (i.e., higher pKa) compares to the primary amine [67-70]. High bonding energy between -NH- group and CO_2 results in high CO_2 peak desorption temperature during TPD. The high basicity of secondary amine also causes HCl to react more rapidly with -NH- than -NH$_2$. As a result, HCl is most likely to react with -NH- groups then further react with -NH$_2$ groups of TEPA. The elimination of -NH- sites for CO_2 adsorption resulted in the decrease in CO_2 peak temperatures observed in HCl treated TEPA/SiO$_2$.

Figure 4-26 (b) shows the CO_2 MS profile during the TPD over TEPA/SiO$_2$ from H$_2$O injection experiment. The decrease in desorbed CO_2 was observed but the CO_2 peak desorption temperature remained at 100 ^{o}C for all 3 cycle, indicating that injection of H$_2$O caused the removal of TEPA in molecular form which the primary and secondary amine groups were removed simultaneously.
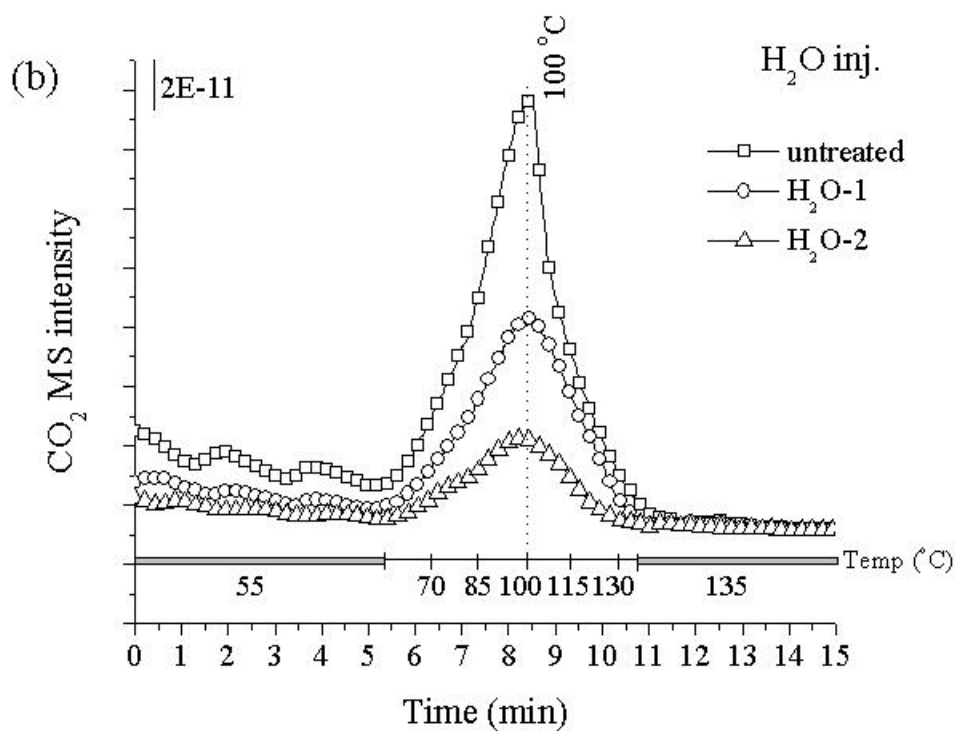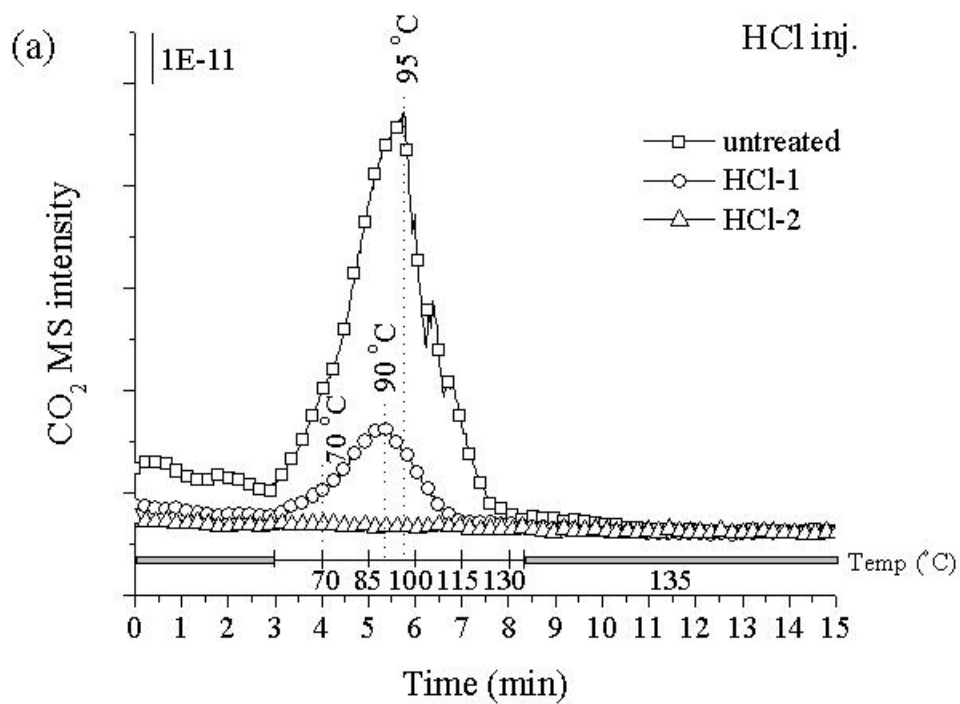
Figure 4-26. CO_2 MS profile during TPD over TEPA/SiO_2 from (a) HCl and (b) H_2O experiment.

65
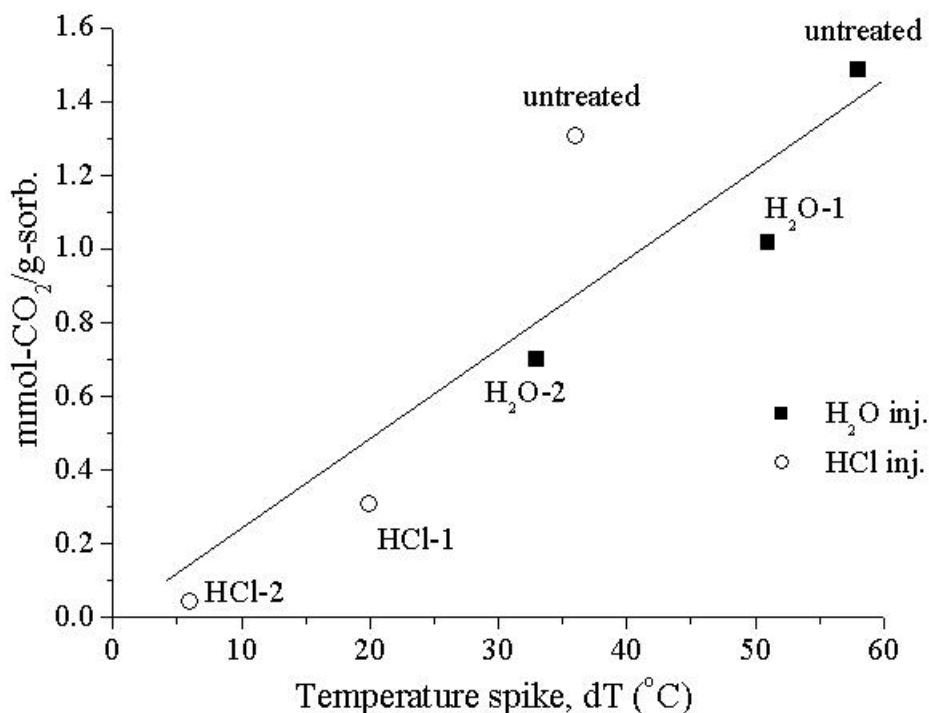
Figure 4-27. Temperature spike during CO_2 adsorption vs. CO_2 capture capacity of TEPA/SiO$_2$

Figure 4-27 shows the plot between the temperature spike, dT, during the switching from Ar to CO_2/air and CO_2 capture capacity of TEPA/SiO$_2$ from HCl and H_2O experiments. The temperature spike was determined by subtracting the maximum temperature detected at the switching from Ar to CO_2/air with the adsorption temperature of 55 ^{o}C. Temperature spike is found to be directly proportional to the CO_2 capture capacity regardless of the HCl or H_2O treatment, suggesting the temperature spike during the CO_2 adsorption can be used as an indicator of sorbent working capacity during multiple CO_2 capture cycles. The fresh CO_2 solid sorbent should exhibit high temperature spike during the initial CO_2 capture cycles. As the sorbent degrades and becomes less active, the temperature spike during CO_2 adsorption is likely to decrease. Hence, the temperature spike during CO_2 adsorption may be used as an early indicator of the sorbent degradation.
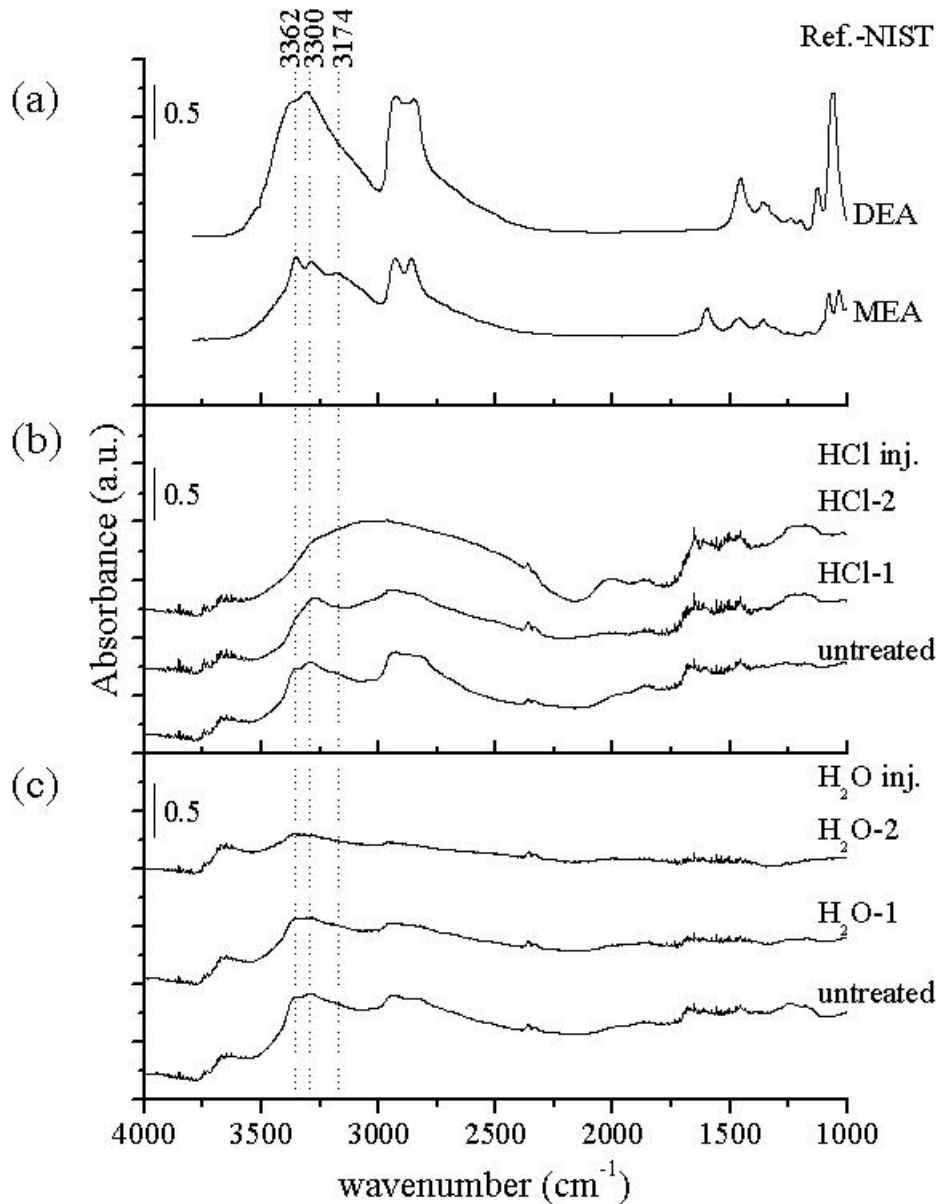
Figure 4-28. Absorbance spectra over (a) MEA and DEA, (b) untreated and HCl injected TEPA/SiO_2, (c) untreated and H_2O injected TEPA/SiO_2. Absorbance spectrum is obtained by Abs. = log(1/I) where I is single beam spectrum of interest.

Figure 4-28(a) shows the absorbance spectra over monoethanolamine (MEA) and diethanolamine (DEA) obtained from Nation Institute of Standards and Technology (NIST) for comparison of NH features in 3500-3000 cm^{-1} region with HCl- and H_2O-treated TEPA/SiO_2 in Figure 4-28(b) and (c). MEA, containing -NH_2 on one terminal group and -OH on the other, shows the strong distinct bands at 3362 and 3300 cm^{-1} and broad band centering at 3174 cm^{-1}. DEA, containing one -NH- group, exhibits only two bands at 3362 and 3300 cm^{-1}. The untreated TEPA/SiO_2 absorbance spectra in Figure 4-28(b) and (c) , exhibit two observable bands at 3362

and 3300 cm^{-1} while only weak absorption at 3174 cm^{-1}, indicating the presence of primary amine functional groups from TEPA. Injection of HCl causes the features of these two bands in HCl-1 spectrum to become more like that of the DEA, indicating the disappearance of -NH$_2$ groups while –NH- groups of TEPA remained to be seen on TEPA/SiO$_2$. Further injection of HCl caused the disappearance of 3362 and 3300 cm^{-1} and a broad band in 3300 to 2250 cm^{-1} in HCl-2 spectrum. The broad band in this region can be attributed to the formation of -NH$_3^+$ species. [71-72] Absorbance spectrum after the first H$_2$O injection, H$_2$O-1, in Figure 4-28(c) exhibits the decrease in 3362, 3300, and 3174 cm^{-1} bands. The shape of these bands remained resemble to those of the primary amine but the intensities decrease with the amount of H$_2$O injected, confirming that injecting H$_2$O causes the removal of the TEPA from surface of SiO$_2$.

Figure 4-29(a) shows the absorbance spectra obtained after each HCl injection at 55 $^{\circ}$C from HCl-1 and HCl-2. The single beam spectrum of untreated TEPA/SiO$_2$ prior to HCl injection was used as the background. The decrease in 3362 and 3300 cm^{-1} intensities after the injections indicates the removal of -NH- functional group from the sorbent. [53,56,58] The strong increase of absorbance intensity in 3200 to 2800 cm^{-1} region could be attributed to (i) increase in H-bonding interactions between the sorbent and H$_2$O from HCl solution [52-53] and (ii) formation of -NH$_3^+$ from the reaction between HCl and amine sites of TEPA. [72] Formation of -NH$_3^+$ also produced several distinct bands in 1700-1500 cm^{-1} region. [72-74] the bands at 1650 and 1610 are assigned to asymmetric deformation whereas the band at 1514 cm^{-1} is assigned for symmetric deformation of -NH$_3^+$.

Figure 4-29(b) shows the absorbance spectra after H$_2$O injection over TEPA/SiO$_2$. The increase in 3750 cm^{-1} after both H$_2$O injections indicates the increase in free surface silanol groups[52-53], suggesting the replacement of TEPA with H$_2$O on the surface of SiO$_2$. The decrease in intensity of 3362 and 3300 cm^{-1} band was observed after the first H$_2$O injection and the bands further dropped after the second injection. Similar trend was observed at 2931 and 2880 cm^{-1} which can be attributed C-H stretching of C-H groups from TEPA[21,54,64], suggesting that injection of H$_2$O causes the TEPA to be removed from surface of SiO$_2$. The 2931 and 2880 cm^{-1} bands did not show the significant decrease during HCl injection experiment in Figure 4-29(a) further confirms that HCl only react with -NH-/-NH$_2$ groups of TEPA.
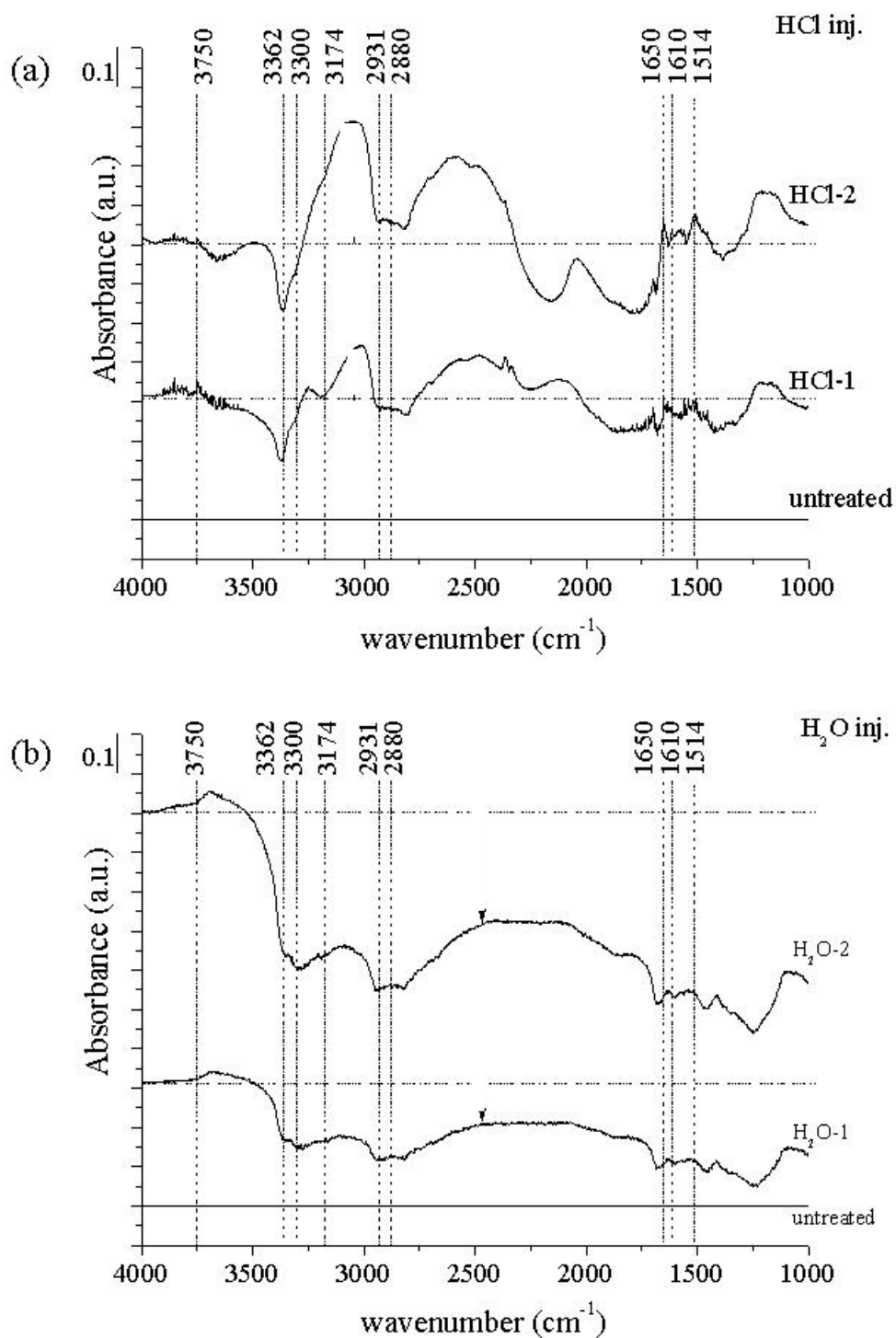
Figure 4-29. Absorbance spectra after injection of (a) HCl and (b) H_2O over TEPA/SiO_2. Absorbance spectrum is obtained by Abs. = $\log(I_0/I)$ where I is single beam taken after removing excess H_2O at each injection and I_0 is the single beam spectrum prior to injection.

69
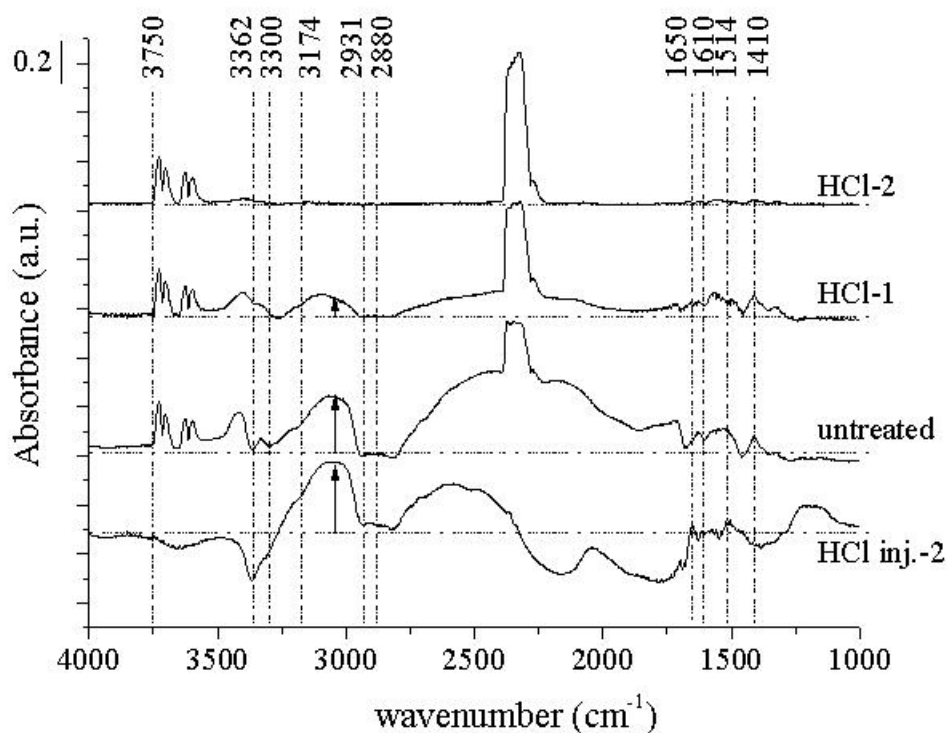
Figure 4-30. Absorbance spectra over TEPA/SiO$_2$ after the second HCl injection (HCl-2) and those obtained during the 3 CO$_2$ adsorption cycles from HCl injection experiment. Absorbance spectra during CO$_2$ adsorption are obtained by Abs. = log(I$_0$/I) where I is single beam taken during CO$_2$ adsorption and I$_0$ is the single beam spectrum prior to CO$_2$ adsorption.

The absorbance spectra over TEPA/SiO$_2$ after the second HCl is re-plotted and compared with the absorbance spectra during the CO$_2$ adsorption after each HCl injection in Figure 4-30. The single beam spectrum prior to each CO$_2$ adsorption was used as the background. The rise in 3200-2800 cm^{-1} region was observed in CO$_2$ adsorption of HCl-1 and HCl-2 spectra which resembles to that observed in absorbance spectrum over TEPA/SiO$_2$ after HCl injection, indicating the formation of -NH$_3^+$ during the CO$_2$ adsorption. The absorption in 2750 to2500 cm^{-1} may be related with the formation of the -NH$_3^+$ as both absorbance spectra exhibit the similar feature to that of HCl inj.-2 spectrum. Adsorption of CO$_2$ onto TEPA/SiO$_2$ also generates bands in 1600 to1100 cm^{-1} relating to formation of carbamate and carboxylate species. The assignment and analysis of the bands generated during the CO$_2$ adsorption can be found in our previous studies. [54,66] All of the absorbance spectra during CO$_2$ adsorption exhibit the distinct peak at 1410, evidencing in the formation of carboxylate species. The decrease in CO$_2$ adsorption activity of the sorbent after each HCl injection is reflected by the decrease in absorption of -NH$_3^+$ broad band at 3000-2800 cm^{-1} along with those carbamate and carboxylate species in 1600-1100 cm^{-1} region observed in HCl-1 and HCl-2 spectra. The IR band assignments presented in this study are summarized in Table 4-9.

70

Table 4-9. IR band assignments.

Wavenumber (cm^{-1})	Assignment	Species	Ref.
1410	COO$^-$ symmetric stretching	carboxylate	53,66,75-76
1514	NH$_3^+$ symmetric deformation	NH$_3^+$	69,72
1610	NH$_3^+$ asymmetric deformation	NH$_3^+$	72
1650	NH$_3^+$ asymmetric deformation	NH$_3^+$	72
2880	C-H stretching	TEPA	21,54,60
2931	C-H stretching	TEPA	52-54
3174	N-H stretching	NH$_2$ of TEPA	69
3300	N-H stretching	TEPA	1,21,71
3362	N-H stretching	TEPA	1-2,71
3750	Unassociated Si-OH	SiO$_2$	2,60
3600-3000	Hydrogen bonding	TEPA, SiO$_2$, H$_2$O	58,64
3200-2800	NH$_3^+$ asymmetric and symmetric deformation	NH$_3^+$	69

4.4.2   Conclusion

The CO$_2$ capture capacity of TEPA/SiO$_2$ can be severely reduced under the presence of excessive HCl and H$_2$O. HCl reacted with the amine functional groups, both primary and secondary amines, of TEPA, producing -NH$_3^+$ ion. The increase in -NH$_3^+$ absorbance intensity indicated by broad band at 3200 to 2800 cm^{-1} together with the decrease in N-H stretching absorbance intensity at 3362 and 3300 cm^{-1} suggests the formation of -NH$_3^+$ from the amine site of TEPA, resulting in the reduction of available CO$_2$ adsorption sites. HCl was likely to react with -NH$_2$ sites of TEPA and further react with the -NH- sites as evidenced by (i) reduction of CO$_2$ peak desorption temperature, (2) elimination of broad band at 3174 cm^{-1}, and (3) alteration of 3362 and 3300 cm^{-1} peak shapes after each HCl injection.

The absorbance spectra during CO$_2$ adsorption also show the rise in broad band at 3200 to 2800 cm^{-1}, suggesting the formation of -NH$_3^+$ during the adsorption. The reduction in absorbance intensity at 3362, 3300 cm^{-1} (N-H stretching) and 2931, 2880 cm^{-1} (C-H stretching) after H$_2$O injection suggests that the presence of H$_2$O causes the removal of TEPA from the surface of SiO$_2$ in molecular form.

The CO$_2$ capture capacity of the sorbent is strongly correlated with the temperature spike, caused by the exothermic reaction between CO$_2$ and amines, during the CO$_2$ adsorption. The large temperature spike indicates the high CO$_2$ capture capacity and vice versa. The decrease in temperature spike can be used as an early indicator of the degradation of the sorbent during the long-term CO$_2$ capture operation.

4.5 Sorbent Testing units

To facilitate determine the performance of the sorbent, a high throughput approach was developed and detailed in the following section.

4.5.1 High-throughput Testing

4.5.1.2 Testing Apparatus

Figure 4-31 depicts a schematic for the high-throughput adsorber which mimics a single pass shell and tube heat exchanger. 0.75 grams of 16 samples will be placed in to individual tubular sample holders and held in place with a nylon mesh supported by a second tube inside the main tube. The cores of the sample tubes are suspended in a chamber where steam can be passed to heat the tube for initial removal of CO_2 and H_2O from the sorbent. CO_2 adsorption will be carried out by passing CO_2/air/H_2O through the bottom of the adsorber, through the tubes, and through the top of the adsorber. The top of the adsorber will be made from quartz to allow monitoring by the thermal camera.
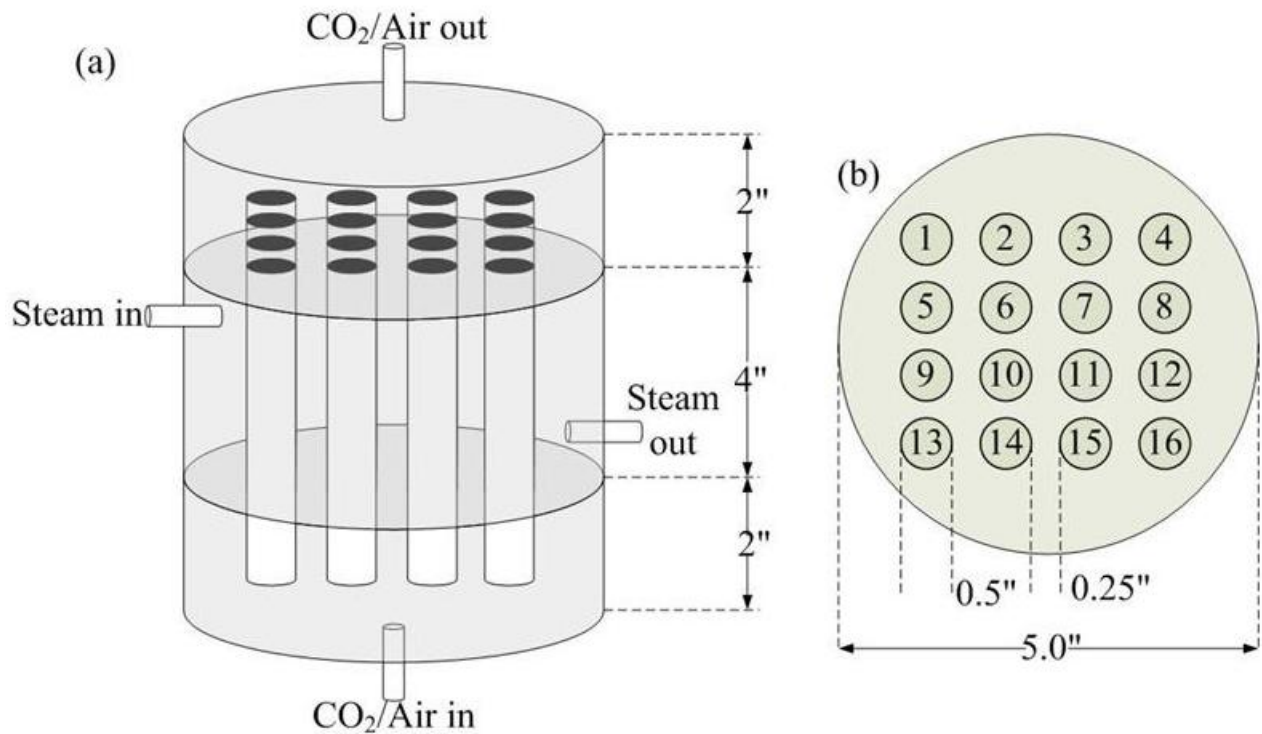
Figure 4-31:   Testing apparatus for high-throughput adsorber that can test 16 samples simultaneously.

4.5.1.2 Testing Procedure

The following is an outline of the procedure to operate the proposed DRIFTS cell:

1. Place sorbent in tubular holder – Place 1 gram of the sorbent in to the tubular sample holder. Then place the nylon mesh over the sample.
2. Attach top – place the top with the quartz window over the sample holders and tighten.
3. Check saturator - The water level of saturator should be above the plastic tube in the saturator and less than 2 inches from the bottom. Higher than 2 inches (5 cm) will flood the adsorber. Temperature of the saturator is should also be set between 50-60 ^{o}C.
4. Turn on air - Turn on the air valve and allow the system to purge
5. Check thermal camera settings – Set emissivity to 0.95, ensure R/T program is running and ready to record, set range to 1, check alignment and view of the samples.
6. Start temperature monitor – Double click the temperature monitor LabVIEW program. Enter a file and location to save the temperature data where the file name ends with a ".xls". The temperature monitor will automatically collect the time each data point.
7. Start collecting thermal data – Start collecting video from the thermal camera.
8. Heat the adsorber – allow steam to flow into the body of the adsorber. Ensure the samples do not go above 100 ^{o}C.
9. Turn off thermal camera – after the sample have been heated, turn off the thermal camera recording to save data space
10. Cool down – Turn off the steam flow and purge with air until the temperature of the sorbent equilibrates.
11. Start recording with thermal camera – turn on the thermal camera recoding
12. CO_2 saturation – Switch the purge air flow for the CO_2 gas stream using the 2-way valve and allow the CO_2 to flow for 10 minutes.
13. Stop thermal camera recording – turn off the thermal camera, this can be done before CO_2 is removed if the samples have stopped releasing heat.
14. Purge – Switch the CO_2 for the inert gas and purge the adsorber.
15. Heat the reactor – allow steam to flow into the body of the adsorber. Ensure the samples do not go above 100 ^{o}C.
16. Repeat steps 10-15 – A total of 3 adsorption cycles should be done to confirm consistency and reliability of the technique.
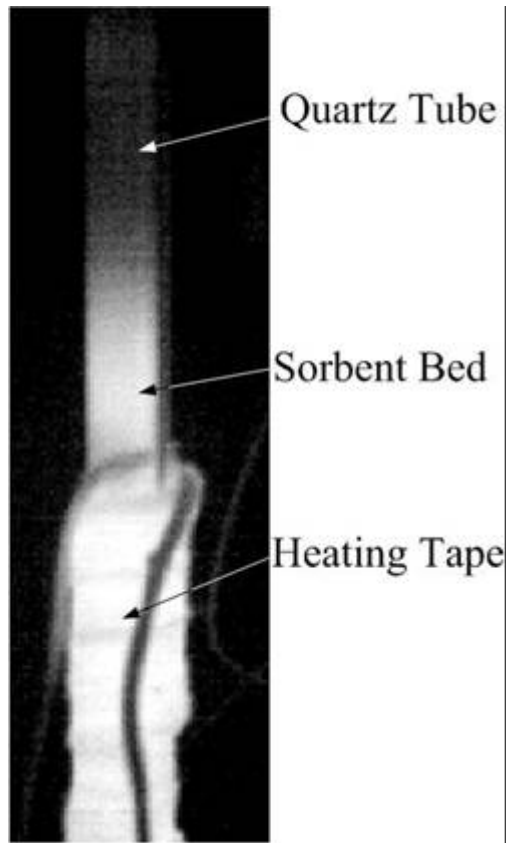
Figure 4-32   Thermal image of the tubular reactor during CO_2 adsorption. The sorbent bed temperature rose 16 $^\circ$C during adsorption.

4.5.1.3 Preliminary and Expected Results

The format of the analysis will be thermal images of 16 samples. Figure 4-32 shows a thermal image from the tubular reactor during CO_2 adsorption. The heating tape has been moved below the sorbent bed and was set to 60 $^\circ$C. This shows the CO_2 adsorption can be monitored through the thermal camera. The thermal images will be compared to the capture capacity found from the tubular system.

The sample emissivity will play a significant role in the thermal imaging of the samples. A sample with lower emissivity will appear lower temperature than its actual temperature. Samples like the activated carbon may have a higher emissivity than SiO_2 skewing the results. Emissivity can be corrected by comparing the sample to a know samples complicating the analysis. The objective of a high-throughput reactor is to screen through sorbents quickly, measuring the emissivity of each sorbent would slow the process. Evaluation of the emissivity will be considered.

The geometry of the pellet will also be a key factor in evaluating the performance of the sorbent with the thermal camera.

4.5.2 Tubular Absorber Testing

4.5.2.1 Testing Apparatus

The experimental apparatus, shown in Figure 4-33, consists of a gas manifold comprising three rotameters, two 2-way valves, the adsorber, and a transmission IR cell placed in an Nicolet 7600 FT-IR bench. The adsorber consisted of a quartz tube where 1.0 g of the sorbent was placed. The sorbent was supported by a nylon mesh attached to an aluminum tube that allowed gas flow through the tube and mesh. The aluminum tube was held and sealed by rubber tubing between the quartz tube and aluminum tube. A thermocouple was placed through the lower nylon mesh for monitoring the bed temperature. A heating tape maintained at 110 ^{o}C was placed above the bed during CO_2 adsorption and slid down to the sorbent bed to provide heat for desorption. Air with a trace amount of CO_2 and H_2O was provided to the system from an IR purge air unit.
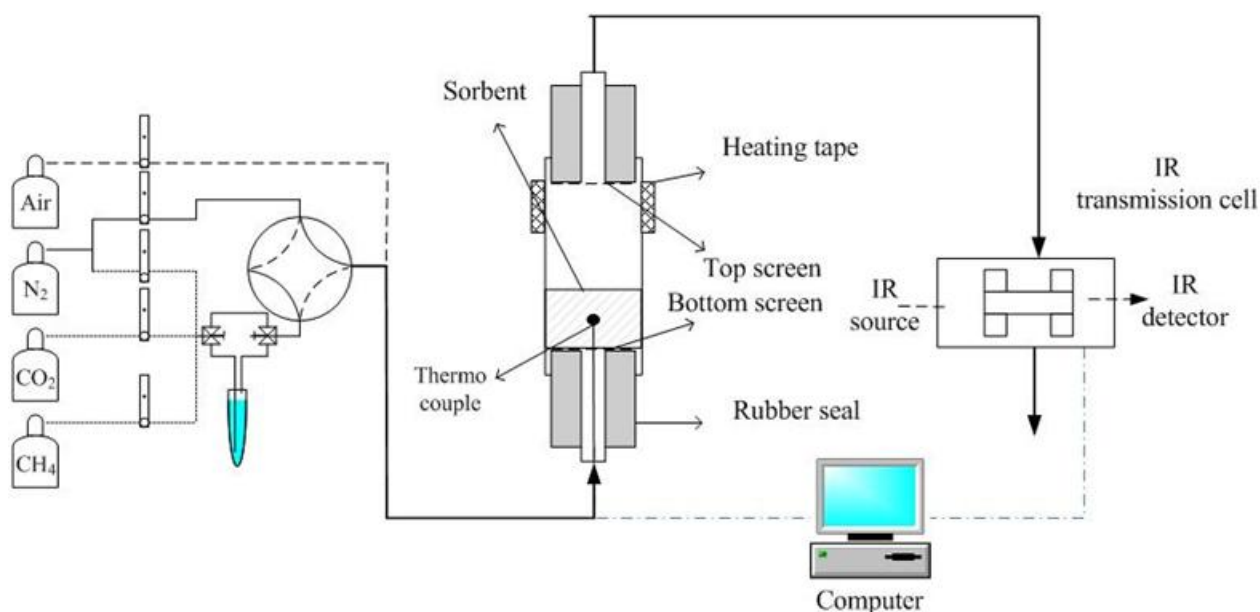
Figure 4-33   Experimental apparatus for tubular adsorber.

4.5.2.2 Testing Procedure

The following is an outline of the procedure to operate the proposed tubular adsorber:

1. Place sorbent in adsorber. - Place 0.5-1.0 grams of the sorbent in the adsorber checking the seal on both ends are sealed
2. Check saturator - The water level of saturator should be above the plastic tube in the saturator and less than 2 inches from the bottom. Higher than 2 inches (5 cm) will flood the adsorber.

3. Turn on air - Turn on the air valve and allow the system to purge. Adjust the flow rate after the transmission cell to 1 L/min.
4. Check series scans - Set the series scan time, crtl+G under the series tab and select the time allowing adjustment to the length of time the IR will scan. Time should be limited to 240 minutes because of file size.
5. Start temperature monitor – Double click the temperature monitor LabVIEW program. Enter a file and location to save the temperature data where the file name ends with a ".xls". The temperature monitor will automatically collect the time each data point.
6. Start file series –
7. Background scan – Before starting the series scan, the IR will collect a background, ensure air is flowing during this time. The start time the IR will label corresponds to the time the background is collected.
8. Start Series scan - After the background scan, a popup window will appear, before collecting, note the exact time to correlate the temperature and IR data
9. Place on hot bath - Move tube to the hot bed to remove atmospherically adsorbed H_2O and CO_2.
10. Inject calibration – After the bed temperature has reach 80 ^{o}C and CO_2 peak is not visible in the IR spectra, inject 2 cc of CO_2 through the adsorber, where the bed thermocouple comes through the bottom of the adsorber.
11. Remove heat – After the bed temperature has reach at least 80 ^{o}C and the CO_2 is no longer visible in the IR spectra, place the tube in the cool bath.
12. CO_2 saturation – Turn off the air valve and turn on the CO_2 valve. Allow the CO_2 to flow for 10 minutes..
13. Purge – Turn the CO_2 off and the air back on to purge CO_2. After CO_2 is not visible in the IR, shut off all gas to the adsorber.
14. Place on hot bath - Move adsorber to the hot bed to remove adsorbed H_2O and CO_2.
15. Purge CO_2 out – After the bed temperature has reached 80 ^{o}C, turn on the air and allow the CO_2 to be purged to the FTIR transmission cell for quantification.
16. Repeat steps 9-13 – after the bed temperature is at 55 ^{o}C, repeat steps 9-13. One injection per an IR file is sufficient to calibrate and quantify the CO_2 capture capacity.
17. Process the data – after the IR has been stopped, extract the 2349 cm^{-1} wave number profile for CO_2. Integrate the pulse area and each of the areas of the desorbed CO_2 during heating.

4.5.2.3 Preliminary and Expected Results

Figure 4-34 shows the IR intensity of the transmission cell of wavenumber 2349 cm^{-1} and bed temperature as a function of time during 6 cycles of CO_2 adsorption and desorption over TEPA/SiO$_2$. The sorbent was initially heated to remove CO_2 and water. Switching from air to CO_2/air resulted in an increase in bed temperature due to the exothermic adsorption of CO_2 on TEPA. Heating temperature in the 4th cycle was increased, which resulted in a change of color of the sorbent from pale yellow to dark yellow and in a decrease in CO_2 capturing ability of the following cycles. The initial air flow after this heating resulted in temperature drop for the first four cycles and a rise for the latter two.

Cycles 3 and 6 from Figure 4-34 have been replotted in Figure 4-35 to present more details of the process. A profile of the gas flow to the adsorber has been expressed as a function of the heating time. The heat released during CO_2 adsorption in the cycle 6 was of a significantly smaller amount, which confirms the deterioration of the CO_2-capturing properties of this sorbent. Figure 4-34 contains the results of 6 cycles of TEPA/SiO_2 and TEPA/carbon pellet. Integration of the temperature change during CO_2 adsorption resulted in a relative quantification of the heat of adsorption. The heat of adsorption on TEPA/SiO_2 indicates that a greater amount of heat was released before the sample was heated to 116 ^{o}C which also resulted in lower CO_2 adsorption capacity.
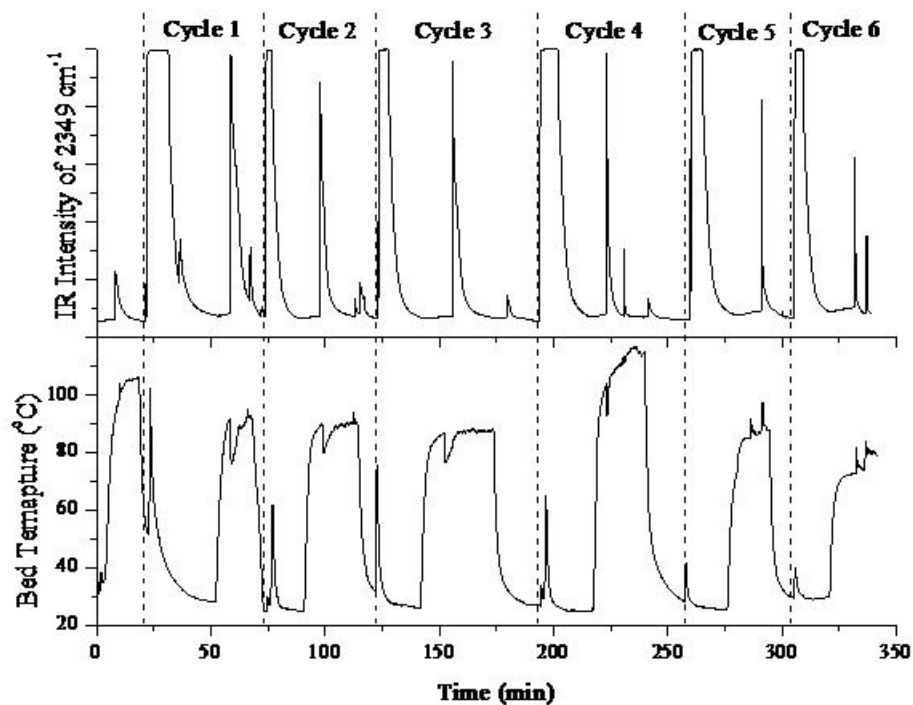
Figure 4-34   The transmission IR intensity of wavenumber 2349 cm^{-1} and bed temperature as a function of time.
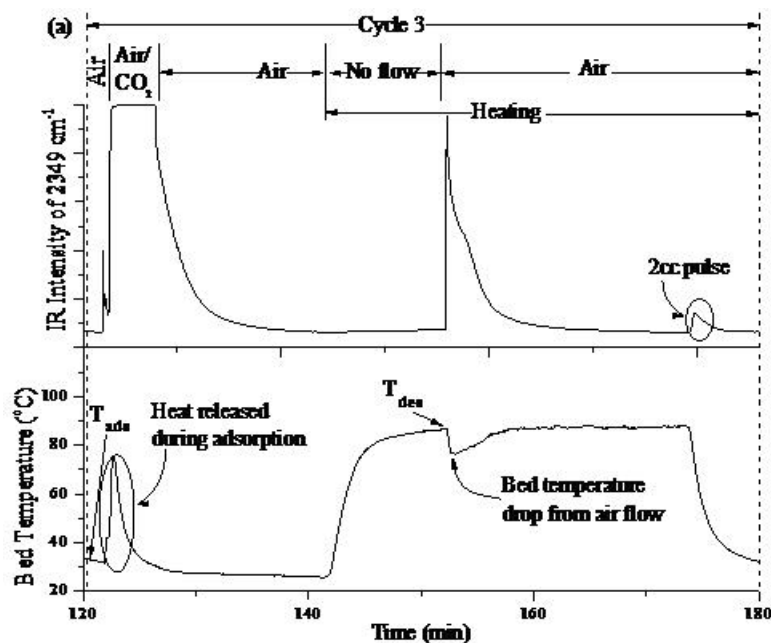
Figure 4-35   Replot of cycle 3 from Figure 4-34 were flow of air and CO_2 and heating are shown as a function of time.

Further scale up to an adsorber with a 10 g sorbent capacity, built in a similar configuration resulted in heat transfer limitations. The heating tape on the exterior of the tube was heated to 300 ^{o}C and resulted in a bed temperature of 53 ^{o}C. The outer edge of the bed was dark orange powder while the center of the bed was in the original state. Two additional CO_2 adsorption tests were performed on the TEPA/SiO$_2$. The first test shows the results of increasing the heating tape temperature to 300 ^{o}C to increase the rate of heating. The bed temperature reached to 222 ^{o}C where the sample turned dark orange and a significant decrease in CO_2 adsorption capacity occurred. The second test was done with a water saturator designed for flow rates of 1-100 cc/min. Switching from air to CO_2/air for the second cycle with a flow rate of 1 l/min resulted in flooding of the adsorber and deactivation of the sorbent.

4.5.3   DRIFT Coupled with Tubular Adsorber

4.5.3.1 Testing Apparatus

The   experimental   apparatus,   shown   in
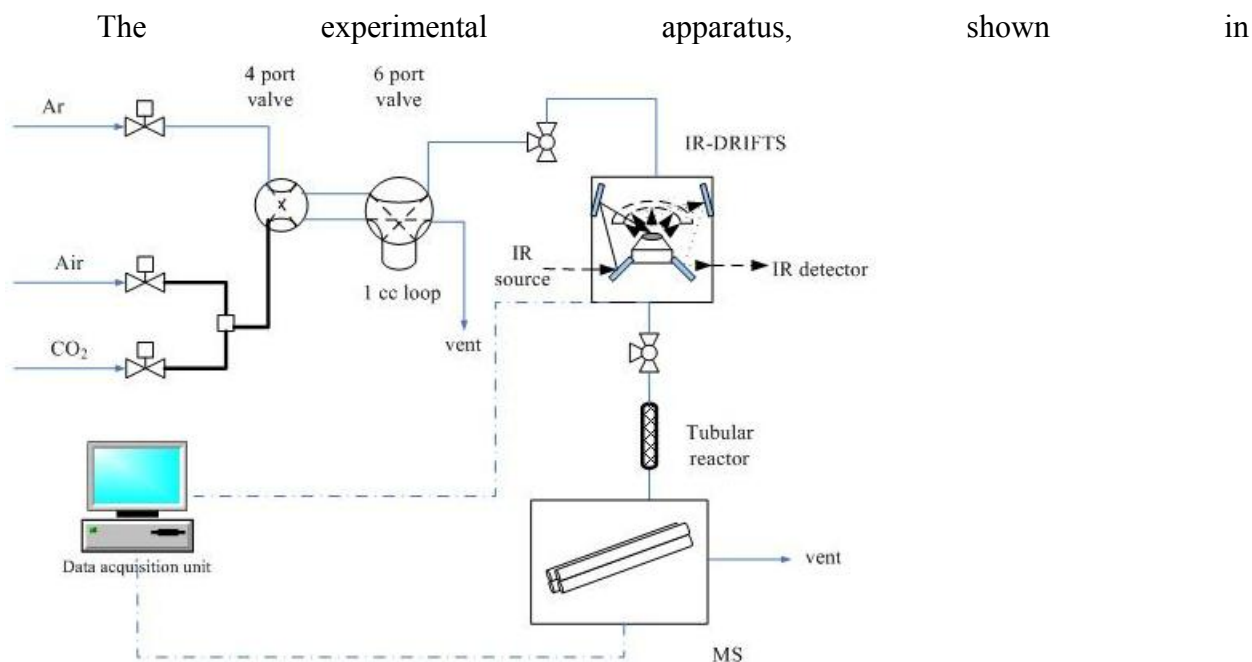
Figure 4-36, consists of (i) a gas manifold comprising three mass flow controllers, a 4-port valve, and a 6-port valve, (ii) a DRIFTS cell (Thermo Scientific) filled with 150 mg of sorbent was placed in a Nicolet 6700 FT-IR bench followed by a heated tubular adsorber with 0.5 g of sorbent (0.65 grams of sorbent total), and (iii) a Pfeiffer QMS 200 quadrupole mass spectrometer (MS) for measuring the effluent composition of the adsorbers. DRIFTS single beam spectrum of the sorbent contains characteristics of the source and sample placed in the path of the IR beam, resembling a transmission spectrum. The DRIFTS absorbance spectra are obtained by using the single beam spectrum of the sorbent in He flow before CO_2 adsorption as the background spectrum. The absorbance spectrum is given by Abs.$=-\log(I/I_0)$, where I and I_0 are the single beam spectrum of an interest and background spectrum, respectively. Difference spectra were obtained by subtraction of two absorbance spectra (i.e. Difference (1)-(2) =Abs. (1) – Abs. (2)). The difference spectra magnify changes occurred during the CO_2 adsorption and desorption processes.
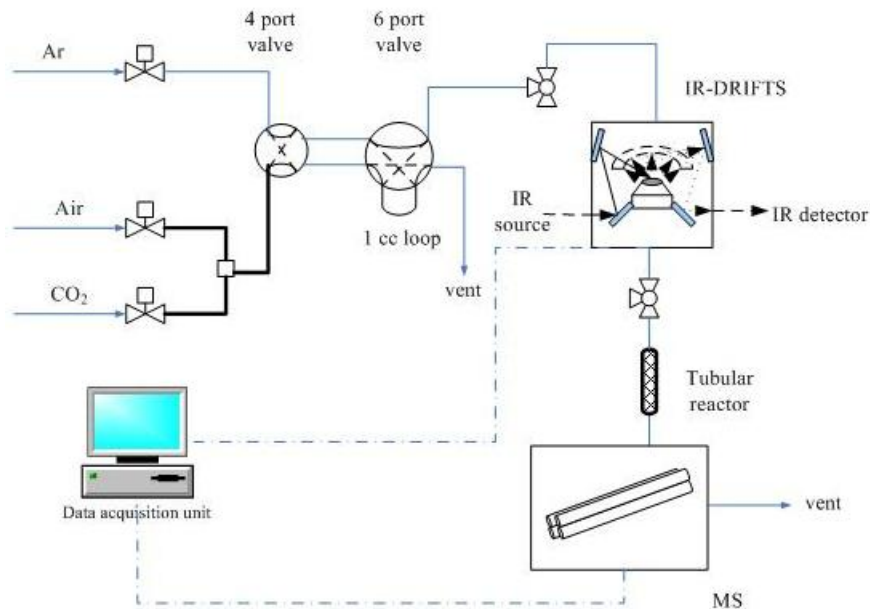
Figure 4-36   Experimental apparatus for fundamental testing of sorbents.

4.5.3.2 Testing Procedure

The following is an outline of the procedure to operate the proposed DRIFTS cell:

1. Place sorbent in DRIFTS cell – Carefully fill the DRIFTS cell from Harick with the sorbent. A glass slide should used to create a flat smooth surface on the sorbent. After the sample holder of the DRIFTS cell is full, place the dome over the cell and tighten. Place the DRIFTS cell in the reactor Praying Mantis holder inside the FTIR bench.
2. Align - Adjusting the mirrors in the Praying Mantis, maximize the signal to the detector. Alignment through the software should also be done.
3. Check saturator - The water level of saturator should be above the plastic tube in the saturator and less than 2 inches from the bottom. Higher than 2 inches (5 cm) will flood the adsorber.
4. Turn on air - Turn on the air valve and allow the system to purge
5. Check series scans - Set the series scan time, crtl+G under the series tab and select the time allowing adjustment to the length of time the IR will scan. Time should be limited to 240 minutes because of file size.
6. Start temperature monitor – Double click the temperature monitor LabVIEW program. Enter a file and location to save the temperature data where the file name ends with a ".xls". The temperature monitor will automatically collect the time each data point.
7. Start MS – Turn on the MS and monitor channels 2, 4, 18, 19, 20, 28, 32, 40, and 44.
8. Start file series –
9. Background scan – Before starting the series scan, the IR will collect a background, ensure air is flowing during this time. The start time the IR will label corresponds to the time the background is collected.
10. Start Series scan - After the background scan, a popup window will appear, before collecting, note the exact time to correlate the temperature and IR data

11. Heat the reactor – Heating the reactor to 80 ^{0}C at a rate of 20 ^{o}C/min to remove atmospherically adsorbed H_2O and CO_2.
12. Inject calibration – After the bed temperature has reach 80 ^{o}C and CO_2 peak is not visible in the IR spectra, inject 1 cc of CO_2 using the 6-port valve.
13. Cool down – After CO_2 is no longer visible in the IR spectra cool the DRIFTS reactor to 55 ^{o}C at a rate of 20 ^{o}C/min.
14. CO_2 saturation – Switch the inernt gas for the CO_2 gas stream using the 4-port valve and allow the CO_2 to flow for 10 minutes.
15. Purge – Switch the CO_2 for the inert gas and purge the DRIFTS cell.
16. Heat the reactor – Heating the reactor to 80 ^{0}C at a rate of 20 ^{o}C/min to remove adsorbed H_2O and CO_2.
17. Repeat steps 9-13 – after the bed temperature is at 55 ^{o}C, repeat steps 9-13. One injection per an IR file is sufficient to calibrate and quantify the CO_2 capture capacity.

4.6   Results from tubular adsorber
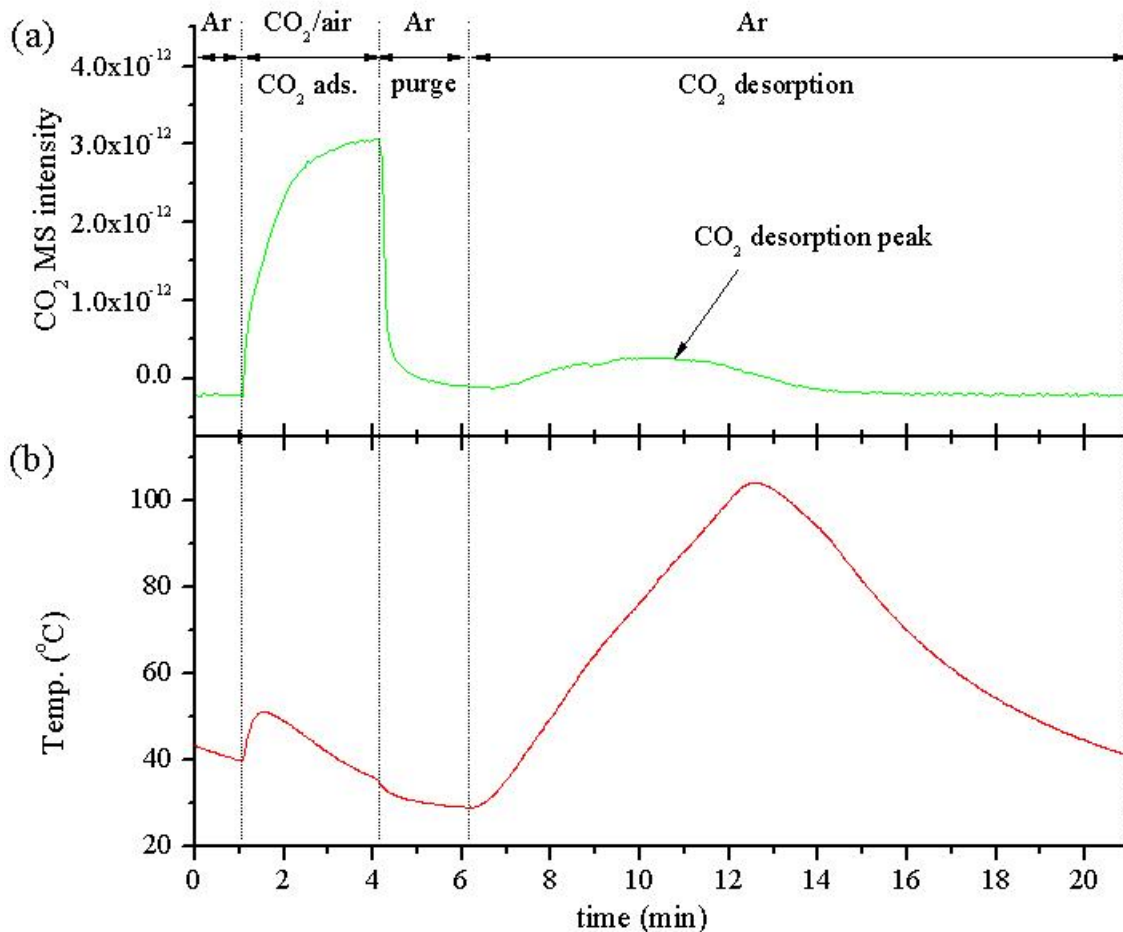
Figure 4-37(a) shows the MS profile of CO_2 during one of the CO_2 capture cycle over sorbent A. The rise in CO_2 MS intensity at the switching from Ar to CO_2/air was observed. CO_2 MS intensity leveled off after 3 min of CO_2 adsorption, suggesting the sorbent became saturated with

CO_2. Switching the inlet flow from CO_2/air back to Ar caused immediate drop in CO_2 intensity. The detail analysis of CO_2 MS intensity during the switching is presented in
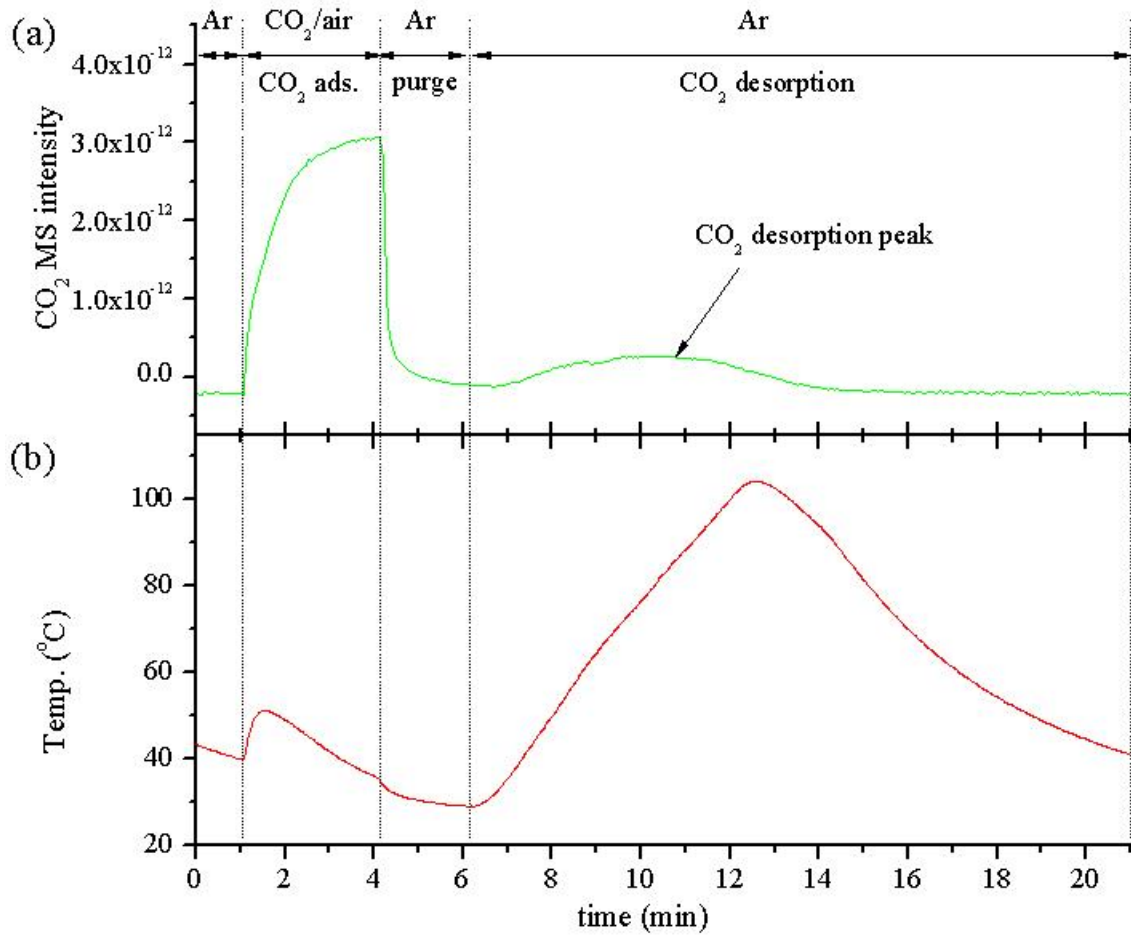
Figure   4-37   and
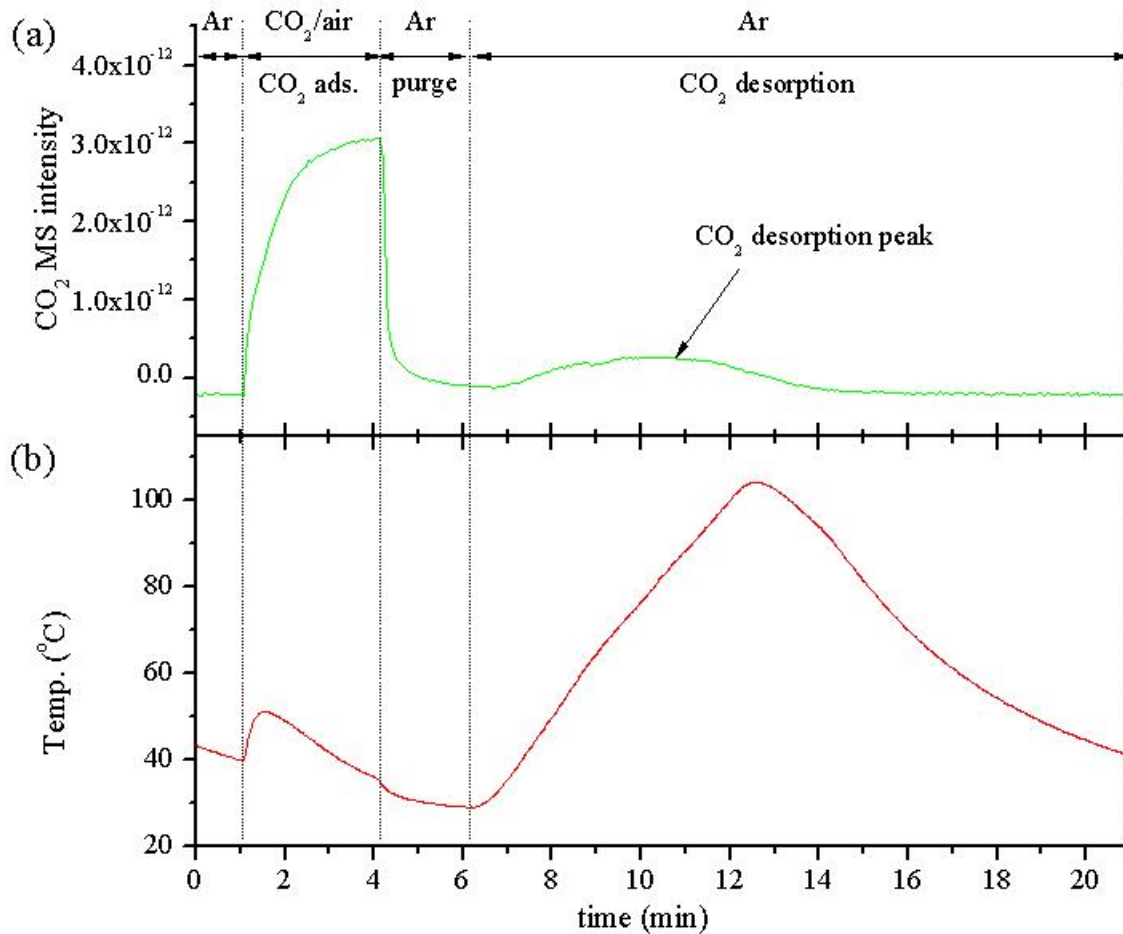
Figure 4-37 Figure 5(a) and (b) Heating the sorbent during the CO_2 desorption step caused a gradual rise in the CO_2 MS intensity which was produced from CO_2 that strongly bound to the amine site of the sorbent. The CO_2 desorption peak reached its maximum point prior to 100 ^{o}C, indicating the CO_2 was completely removed from the sorbent.
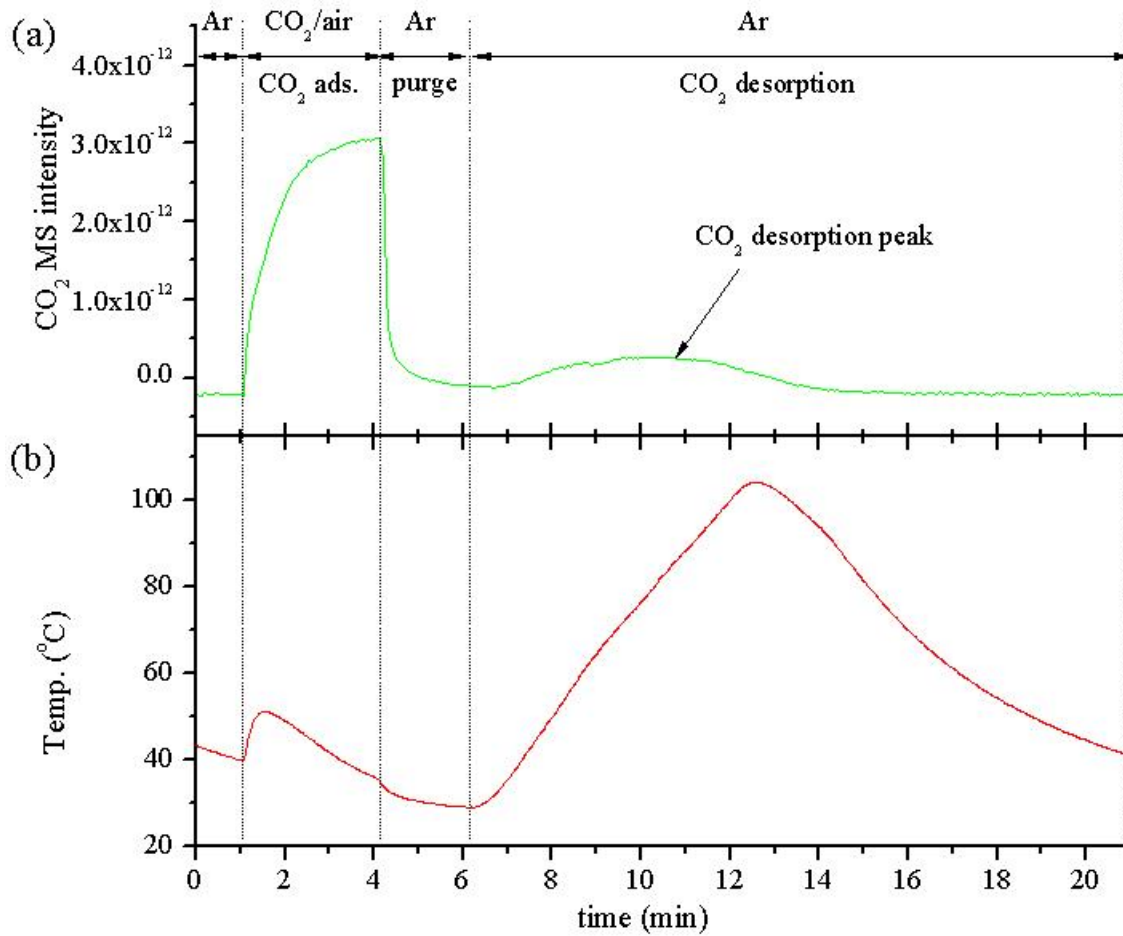
Figure 4-37(b) shows the corresponding temperature profile during a CO_2 capture cycle. The temperature rise from 40 to 50 ^{o}C at the switching from Ar to CO_2/air indicates the exothermic nature of CO_2 adsorption process that took place on the sorbent.
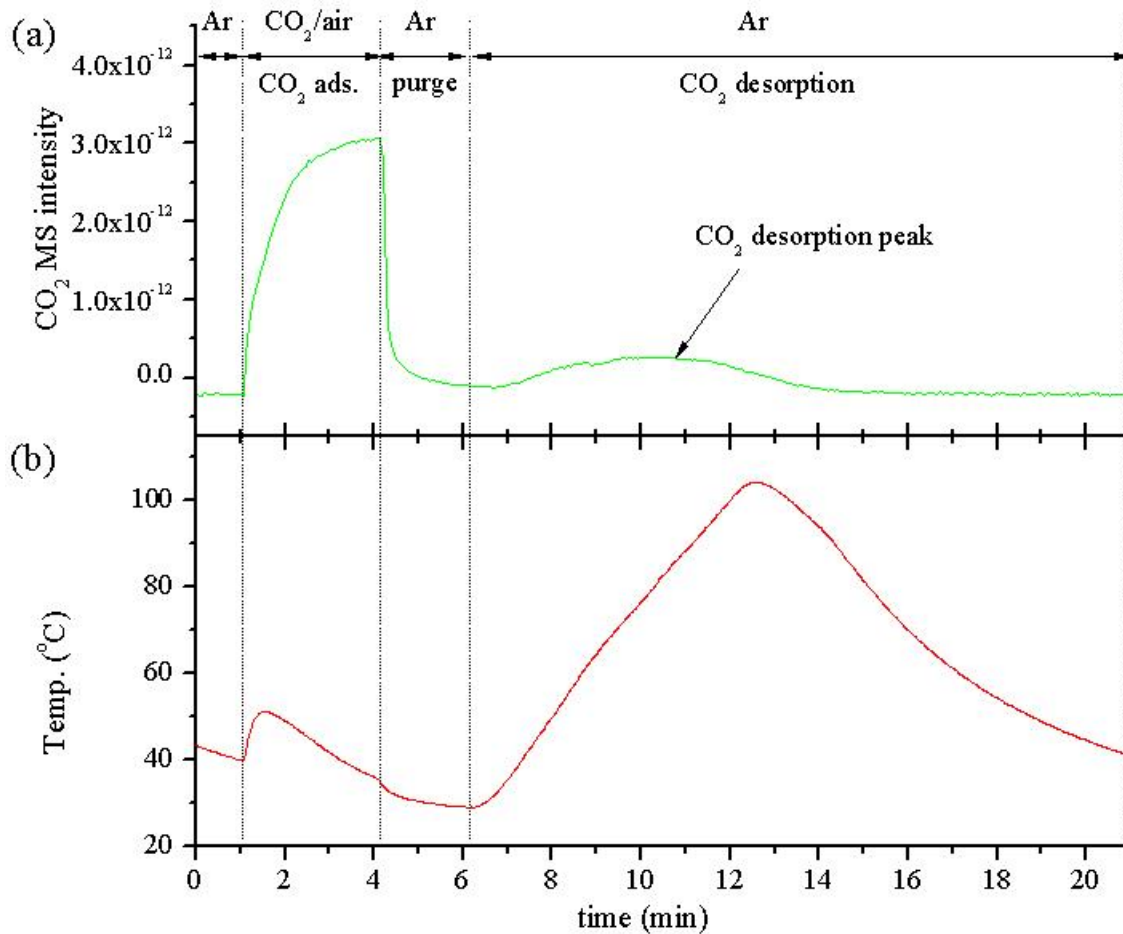
Figure 4-37 (a) CO_2 MS profile during the first CO_2 capture cycle over sorbent A. (b) corresponding temperature profile.

Figure 4-38 (a) shows the overall CO_2 MS profile during the 1,100 cycles of CO_2 capture over sorbent A with the corresponding temperature shown in Figure 4-38 (b). The CO_2 MS profile was enlarged to show the CO_2 peak produced during the CO_2 desorption and neglected the strong CO_2 MS intensity produced during the CO_2 adsorption. The line UV was drawn over the CO_2 desorption peaks to indicate the high consistency of CO_2 peaks produced from the sorbent. Increasing the desorption temperature from 100 to 110 ^{o}C from cycle 800 to cycle 899 (Time = 212 h) did not cause a significant difference in CO_2 desorption peak intensity, suggesting the high stability of the sorbent. Flowing the gas stream through the H_2O saturator at cycle 900 (Time = 410 h) caused the significant decrease in CO_2 desorption peak intensity as indicated by line XY. Inset (c) shows the consistent response of the CO_2 MS intensity and the temperature during CO_2 capture cycles 469 to 495 and inset (d) shows differences between before and after flowing the gas stream through the saturator.
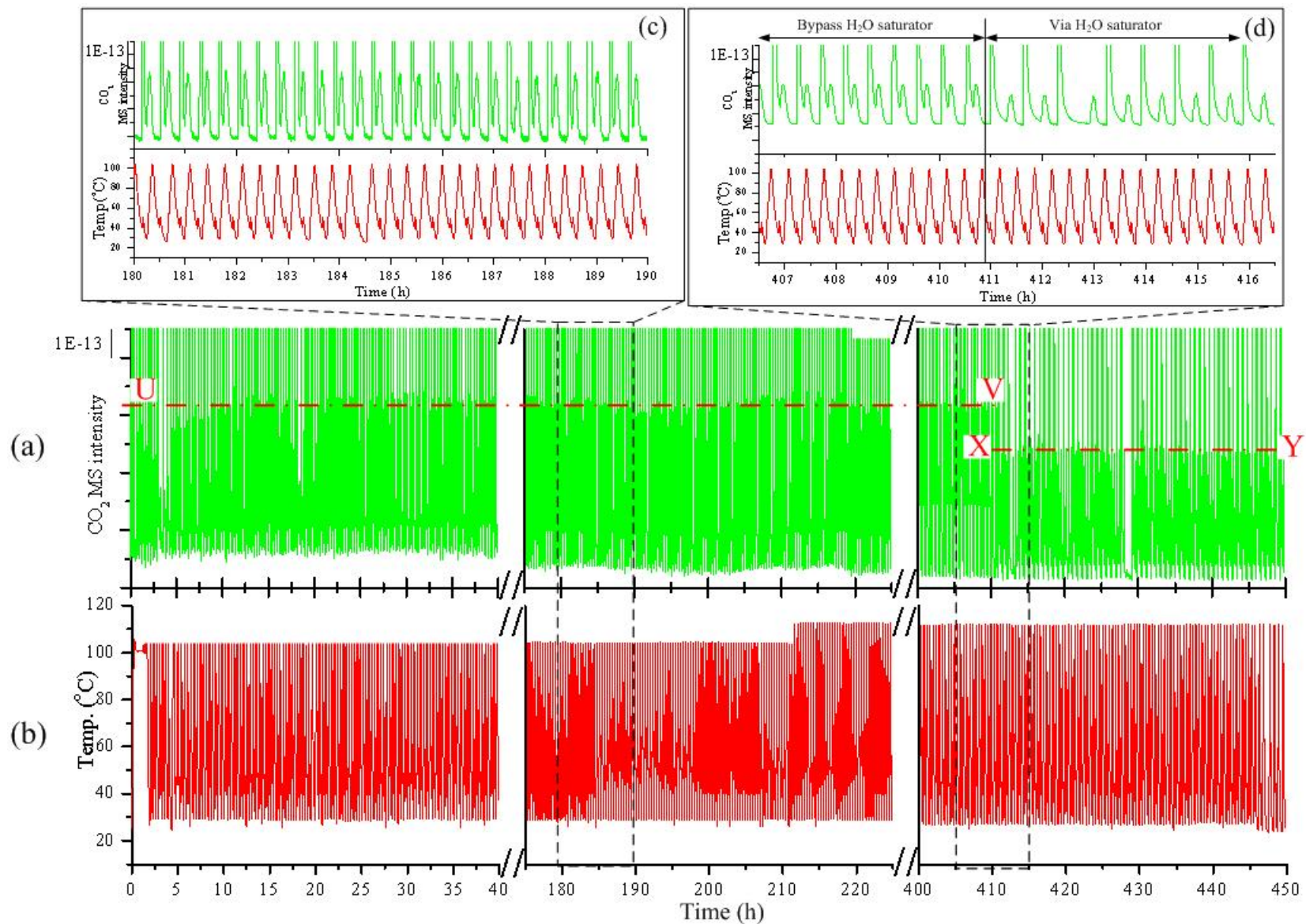
Figure 4-38. (a). CO_2 MS profile during 1,100 CO_2 capture cycles over sorbent A with (b) corresponding temperature profile. Inset (c) shows the CO_2 MS profile and the temperature during CO_2 capture cycles 469 through 495 and (d) cycles 890 through 907.

Figure 4-39 (a) shows the normalized CO_2 MS profile during the switching from Ar to CO_2/air at cycle 1, 250, 500, 750, 1000, and 1100. The N_2 MS profile from cycle 250 was plotted as the reference inert gas. The immediate rise of the N_2 profile upon switching suggests the absence of its adsorption onto the sorbent. The N_2 profile can also be the accurate representation of the residence time distribution of the species flowing through the tubular adsorber. Adsorption of CO_2 resulted in a small delay in the CO_2 MS profile. The concentration of CO_2 rose to saturation 3 min after switching for all of the selected cycles shown. The delayed rise in CO_2 intensity with respect to rapid rise of the N_2 profile indicates the saturating of the amine sites by CO_2. Flowing the gas stream through the H_2O saturator caused the significant lag in CO_2 MS profiles (i.e., cycle 1000 and 1100). Figure 4-39(b) shows the normalized CO_2 and N_2 MS profiles during the switching from CO_2/air to Ar of the same selected cycles. The N_2 MS profile immediately dropped to the baseline where the CO_2 MS profile exhibits a small trailing effect after switching. This suggests (i) the delay of CO_2 transportation through the sorbent and (ii) the continuous desorption of weakly adsorbed CO_2. [56] The significant lag was observed again from the CO_2 MS profiles of cycle 1000 and 1100. Since the N_2 MS profile is the accurate representation of the flow pattern, the weakly adsorbed CO_2 can be determined by calculating the difference in area under curve produced by N_2 and CO_2 profiles. The total CO_2 capture capacity is the summation of strongly and weakly adsorbed CO_2 of the sorbent. The percent contribution of each type of adsorbed CO_2 is also presented. Overall, sorbent A possessed the total CO_2 capture capacity in the range of 0.4 to 0.6 mmol-CO_2/g-sorb. The CO_2 capture capacity determined from strongly adsorbed CO_2 remained unchanged and shows the variation between 0.3 to 0.5 mmol-CO_2/g-sorb., indicating the high stability of the sorbent. Weakly adsorbed CO_2 increased proportionally with the number of cycles run on the sorbent. Flowing the gas through H_2O saturator significantly increased the weakly adsorbed CO_2 which resulted in the increase in total CO_2 capture capacity. This could be due to the increase in formation of carbonate species between NH_2 group of TEPA and CO_2 when the sufficient amount of H_2O is presented. [1-2,21,52-53]
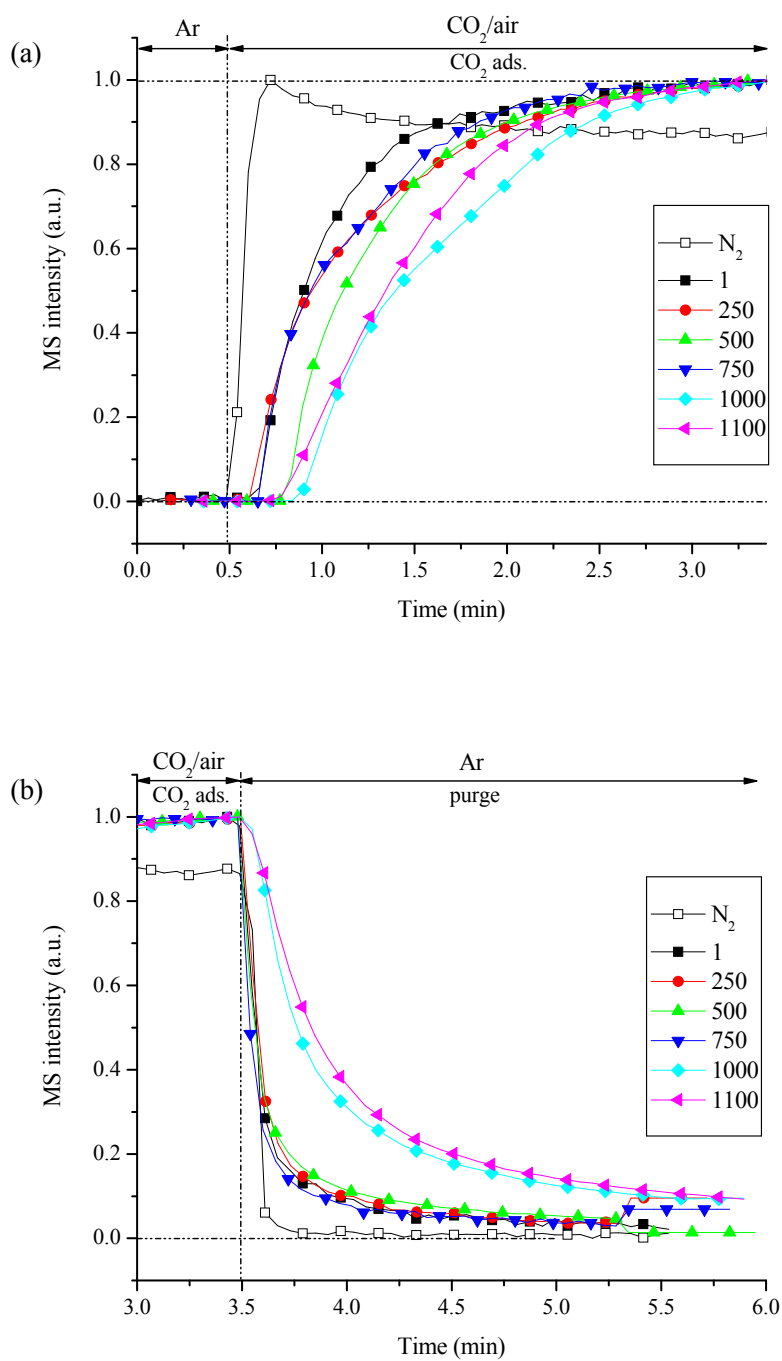
Figure 4-39   (a) CO$_2$ MS profile during the switching from Ar to CO$_2$/air at cycle 1, 2500, 500, 750, 1000, and 1100. And (b) CO$_2$ MS profile during the switch from CO$_2$/air back to Ar at the same cycles. N$_2$ MS profile of cycle 250 is included as the reference.

4.7   Results from Mini Me adsorber (5 g adsorber)

Pelletized sorbent RB-M was run for 100 cycles under dry conditions and 100 cycles under wet conditions. The majority of the cycles were performed under 100% CO_2 purging as described previously in the experimental section of this paper. The desorption peak areas were calculated for the cycles performed under the dry air purge. The temperature and CO_2 gas concentration profiles for the full 100 cycles under the wet conditions are shown in Figure 4-40. The temperature and CO_2 gas concentration profile for the 100 cycles under the dry condition is provided in Figure A-1.
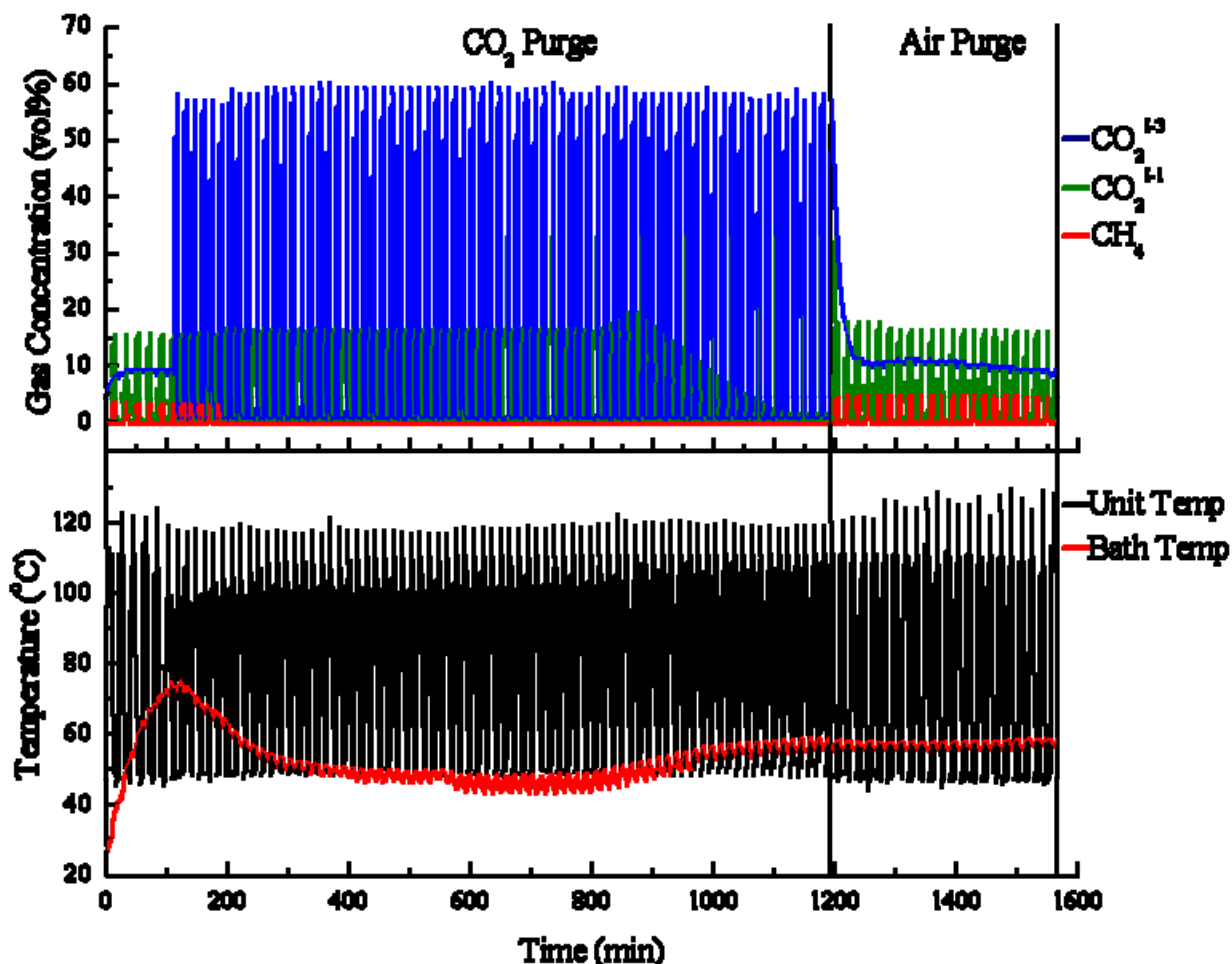
Figure 4-40. Temperature (°C) and CO_2 gas concentration (vol%) for 100 cycles under the wet condition.

4.7.1 CO_2 Breakthrough

Figure 4-41 shows the normalized gas concentration profiles for CH_4, CO_2^{dry}, and CO_2^{wet} during the adsorption cycle set. The CH_4 was used as a tracer gas for comparing the detection and stoichiometric time of both CO_2 conditions. The detection time refers to the amount of time

it takes the gas sensors to first detect an increase in the gas concentrations. The stoichiometric time refers to the amount of time it takes for the CO_2 concentration in the outlet stream to equal half of the concentration at the feed. It can be seen from the figure that the detection time and stoichiometric time of the CO_2^{wet} comes later than the CO_2^{dry}. The first detection of the CO_2^{wet} gas stream occurred 6 seconds later than the CO_2^{dry} gas stream. The stoichiometric half time of the CO_2^{wet} gas stream was not obtained until 8.5 seconds after the CO_2^{dry} profile. The increase in the detection and stoichiometric times indicate a larger amount of the CO_2 adsorption. Clearly, the higher CO_2 capture capacity was obtained through the co-adsorption of water present by running the CO_2 gas through the saturator. The mechanism explaining the enhancement in CO_2 capture capacity in the presence of water has been widely discussed in literature but the main mechanisms are considered to be as follows:

$$CO_2 + 2R_2NH = R_2NH_2^+ + R_2NCOO^- \qquad (1)$$

$$R_2NCOO^- + 2H_2O + CO_2 = R_2NH_2^+ + 2HCO_3^+ \qquad (2)$$

$$CO_2 + R_2NH + H_2O = R_2NH_2^+ + HCO_3^- \qquad (3)$$
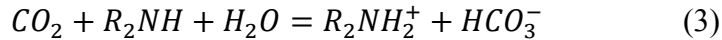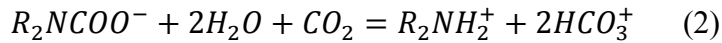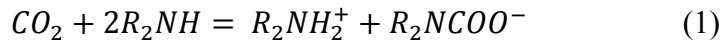
Equation 1 is the accepted mechanism of CO_2 removal by an amine in the absence of water. The reaction describes the formation of carbamate via one mole of amine with a half mole of CO_2. However, in the presence on water, as shown by equations 2 and 3, one mole of amine can react with one mole of CO_2, increasing the effectiveness of CO_2 removal. In this experiment, the presence of water has been shown to increase the amount of CO_2 adsorption by 1.6 to 1.8 times as compared to a dry gas stream. The enhanced capture capacity result was obtained with the saturator temperature held at 55°C, suggesting that the capture capacity could be further increased by optimizing the saturator temperature.
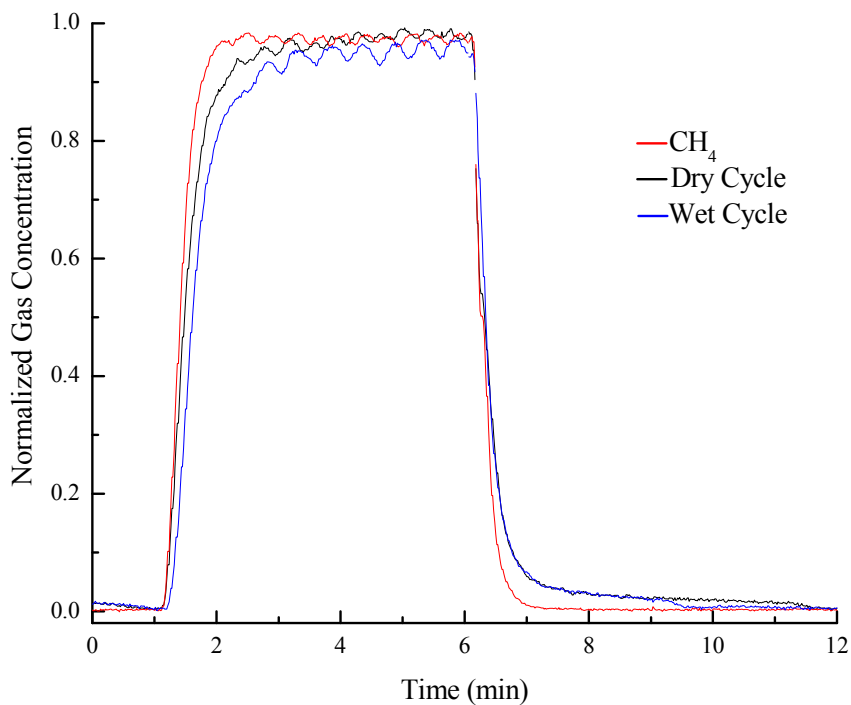
Figure 4-41. Normalized gas concentration profiles of CH_4, CO_2^{dry}, and CO_2^{wet} during the adsorption cycle step.

4.7.2 CO_2 Desorption Peak Area

Figure 4-42 shows the CO_2 gas concentration profiles of the CO_2^{dry} and CO_2^{wet} experimental runs over five cycles. The key observation taken from Figure 4-42 is the consistently larger area of the desorption peaks produced during sorbent regeneration in the presence of water. Table 4-10 provides the calculated desorption peak areas for the dry and wet cycles. The desorption peak areas from the CO_2^{dry} experiment had an average value of 2.44 with a standard deviation of 0.098. The desorption peak areas from the CO_2^{wet} experiment had an average value of 4.37 with a standard deviation of 0.162. The results of the standard deviation for both dry and wet cycles indicate that the CO_2 capture capacity of the sorbent was stable over multiple cycles.
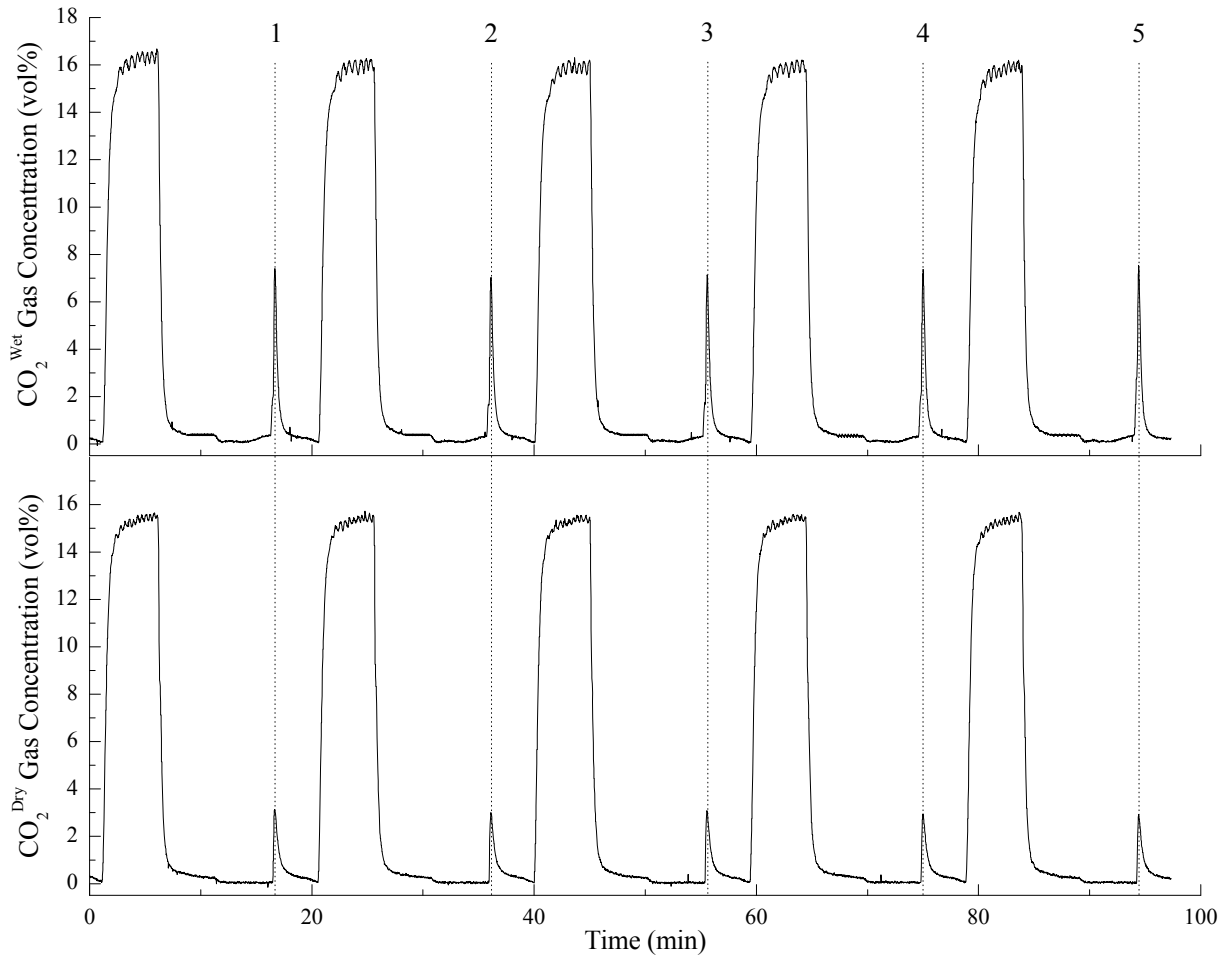
Figure 4-42. CO_2 gas profiles for five CO_2^{dry} and five CO_2^{wet} cycles.

Table 4-10. Desorption peak areas for the CO_2^{dry} and CO_2^{wet} gas profiles.

| Gas Profile | Desorption Peak Area | | | | |
	Peak 1	Peak 2	Peak 3	Peak 4	Peak 5
CO_2^{dry}	2.59	2.49	2.41	2.42	2.29
CO_2^{wet}	4.17	4.29	4.34	4.66	4.37

Figure 4-43 shows the breakthrough profile (a) and desorption peak (b) of cycle four under the dry condition overlapped with cycle four under the wet condition to provide a more complete comparison between the dry experimental condition and the wet. The benefit of the presence of water is apparent from analysis of Figure 4-43. The CO_2 breakthrough for the gas stream containing the water occurred 7.8 seconds after the CO_2 breakthrough of the dry gas stream. The most exciting piece of evidence comes from the comparison of the desorption peak areas shown in Figure 4-43(b), where the area under the peak for the wet condition cycle was 1.9 times greater than that of the dry condition cycle.
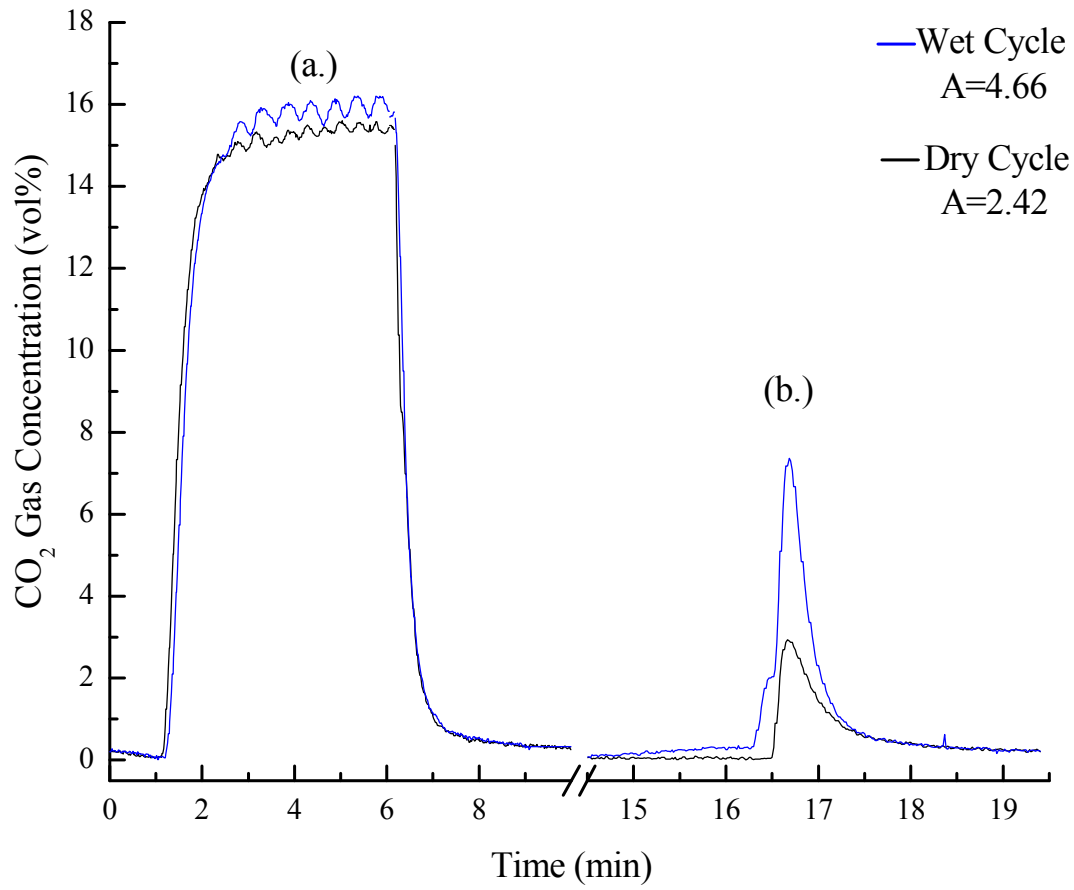
Figure 4-43. CO_2 gas profile during (a) adsorption and (b) regeneration cycle steps.
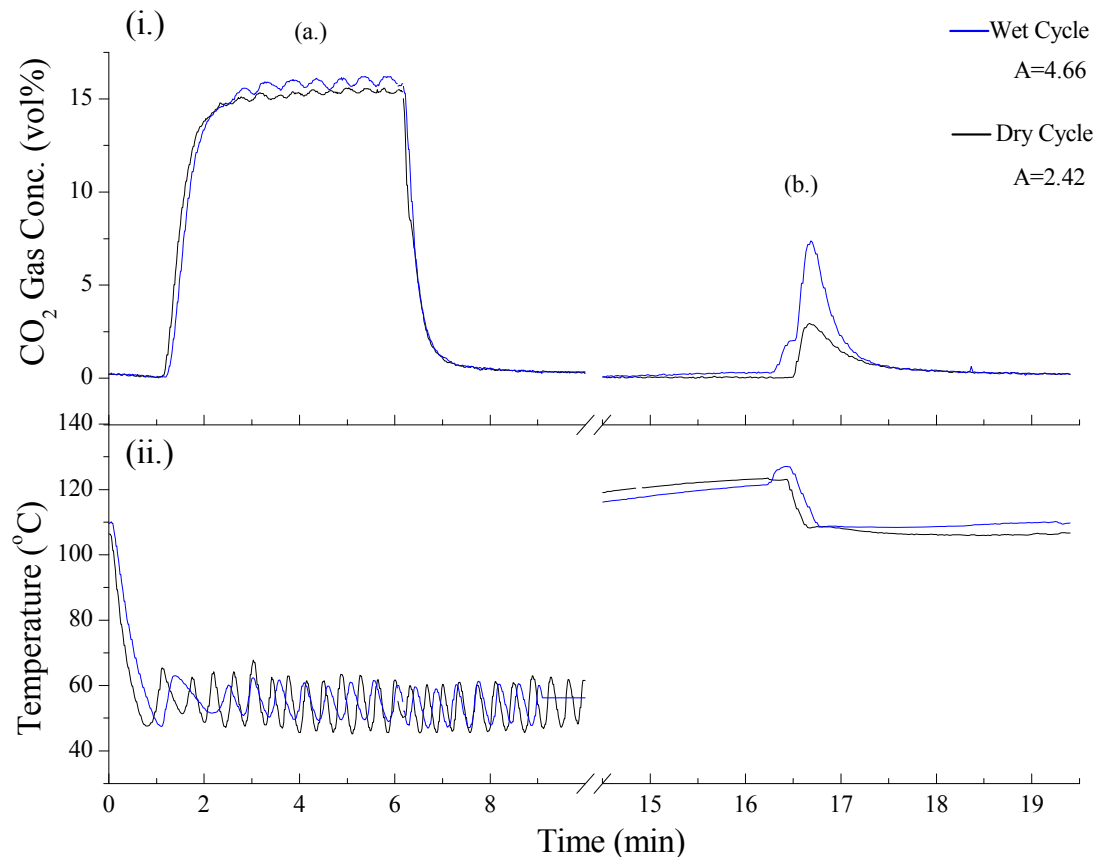
Figure 4-44 (i.) CO_2 gas and (ii.) temperature profile during (a.) adsorption and (b) desorption

4.7.3 Conclusions

Pelletized RB-M sorbent was run in the MiniMe 5 gram adsorber under two conditions; a dry condition where the presence of water in the gas stream was at a minimum, and a wet condition where the gas stream was directed through a water saturator held at 55°C. The same sorbent was cycled 100 times under each condition, starting with the dry condition and finishing with the wet condition. Therefore, the sorbent completed a total of 200 CO_2 capture cycles without interruption.

The results of the cycling experiment indicate that in the presence of water, the CO_2 capture capacity of this sorbent is enhanced by 1.6 to 1.9 times as compared to capture in the absence of water. Analysis of the CO_2 breakthrough between the two conditions shows a significant delay in the sensor response for the wet cycles in relation to the dry cycles. The sensor response for the wet cycles had an average of a 6 second delay compared to the dry cycles. The delay in sensor response has been attributed to an increase in CO_2 capture. Moreover, the desorption peak areas of the wet cycles were universally greater than the dry desorption peak areas. The sorbent captured and desorbed CO_2 with little variance under each condition. This signifies that the sorbent remained CO_2 capture stable over the 200 cycles.

4.8   Results from Pilot plant (25 Kg adsorber)

The sorbents developed from were further studied on a 25 Kg adsorber.   The results of this study indicated that fixed bed operation is not suitable for the CO_2 capture process due to slow heat transfer.

The results of the CO_2 capture cycling in the 25 kg adsorber are shown in Figure 4-25. These preliminary results provide several key pieces of information that will be used for improving the system.   First, the heat transfer into the sorbent bed is too low and slow for a practical application.   The poor heat transfer is physically shown by the temperature profile in Figure 4-45. The ideal desorption process would take place at a temperature range between 100 and 110 oC. However, in this experiment the temperature within the sorbent bed only reached a maximum temperature of approximately 60 oC. The low desorption temperature may possibly lead to water condensation to occur during the direct steam regeneration step. The condensed water would then cause a decrease in the capture efficiency of the process due to pore plugging and/or sorbent agglomeration. Moreover, the adsorber required over ten minutes to reach the maximum sorbent bed temperature. This leads to long term thermal exposure for the sorbent, which has be seen to increase the rate of CO_2 capture capacity degradation due to amine evaporation. Increasing the rate of heat transfer for the 25 kg unit is the most critical parameter needing to be improved.
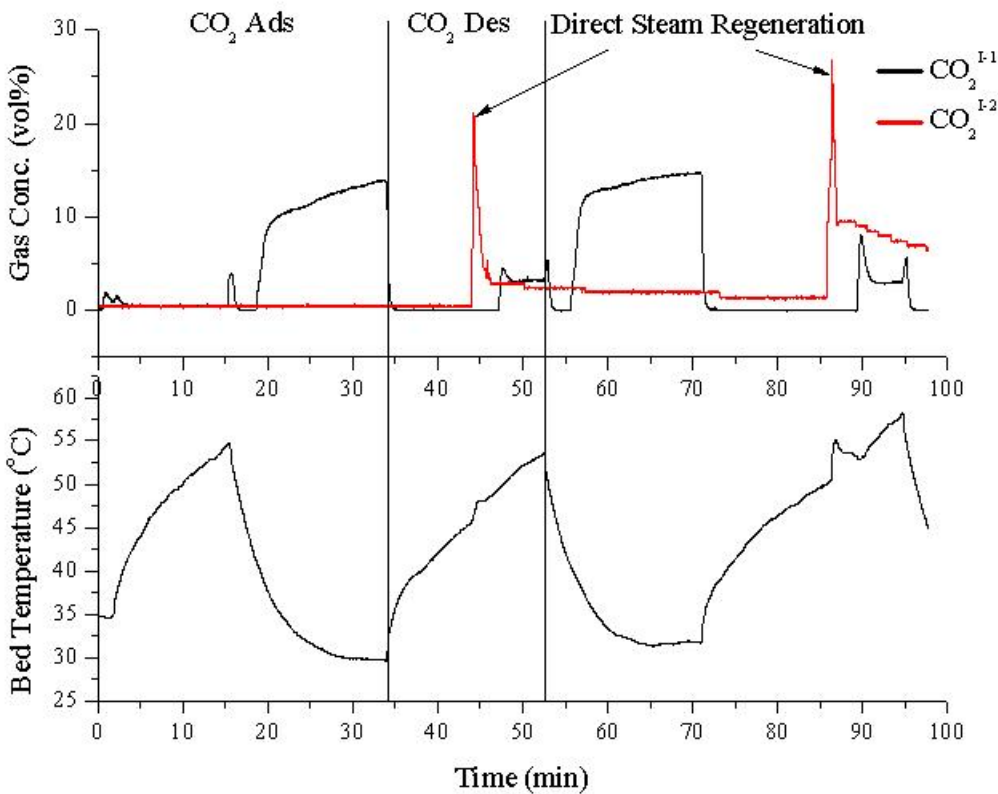
Figure 4-45   Gas and temperature profile of the 25kg adsorber over two cycles.

Despite the poor heat transfer of the adsorber, the preliminary results shown an increase in the CO_2 gas concentration (vol%) during the direct steam regeneration step. The concentration within the desorption line was also shown to increase after consecutive cycles. In this experiment, the gas concentration during the first cycle reached a maximum of 22%. After the second cycle, the gas concentration during desorption reached an increased maximum of 27%. As a preliminary set of results, this was a good result as it shows the adsorber has the potential of desorbing heightened levels of CO_2. It is believed that after the heat transfer has been improved, the gas concentration will be significantly improved. In order to get the most efficient CO_2 capture, the sorbent needs to be regenerated at 100 – 110 oC. Regenerating the sorbent at this temperature range provides enough energy to the CO_2 captured to allow it to be removed from the sorbent structure. However, if the temperature during regeneration remains low, such as in this experiment, only a small portion of the CO_2 captured will be removed. The unresolved CO_2 would then prevent any further CO_2 capture from occurring in subsequent cycles.

4.9 CO_2 Capture results with Radiator Monolith Adsorber

This study shows that metal monoliths provide an excellent means to accelerate the heat transfer for CO_2 capture processes.

4.9.1   Results and discussion

Figure 4-46 shows the CO_2 gas concentration (vol %) and monolith surface temperature profiles for 8 complete CO_2 capture cycles. One key finding in this experiment was the rate of heat transfer to the monolith/sorbent surface during both heating and cooling. The temperature profile during heating and cooling resembles that of a step function. This indicates that the rate to increase the monolith surface temperature from 20 °C to 100 °C was nearly instantaneous. The same conclusion has been made for cooling the monolith surface from 100 °C to 20 °C. This finding is very exciting, as heat transfer has been the rate determining step in our other CO_2 capture experimental apparatuses. The results of this experiment show that rapid cycling of the sorbent can be accomplished using a monolithic structure where the heat transfer comes from within the sorbent coating.
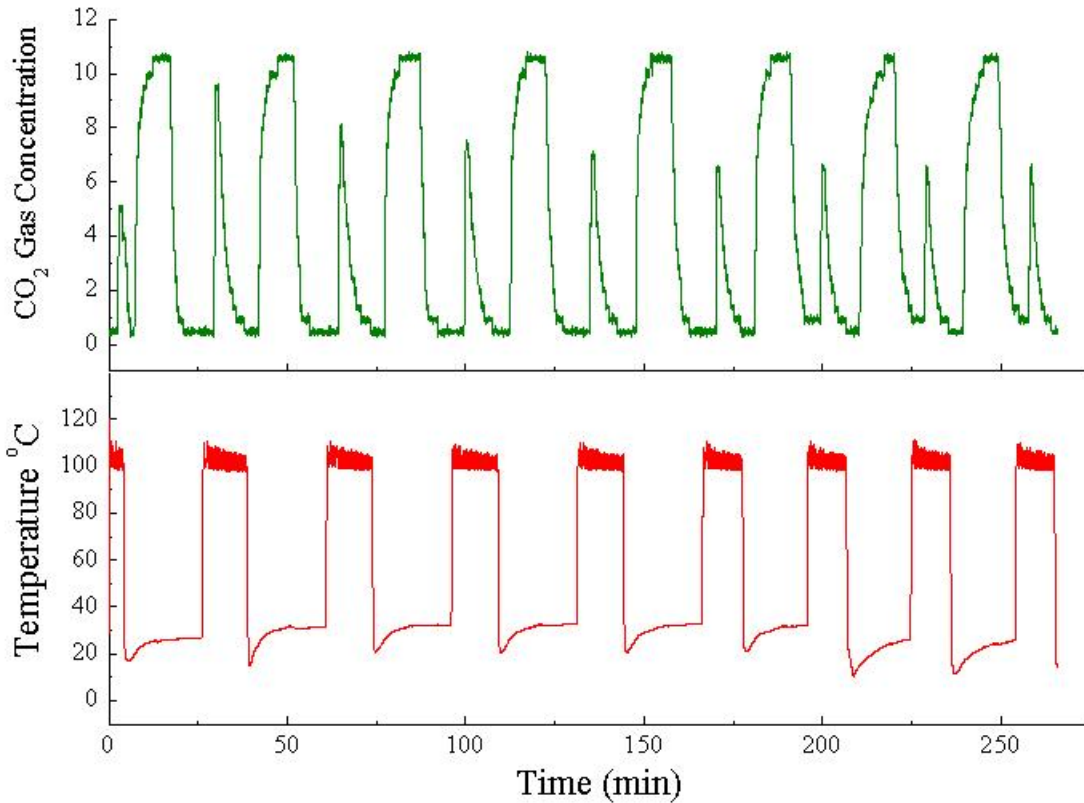
Figure 4-46. CO_2 gas concentration (vol %) and temperature profile of the radiator monolith adsorber over 8 cycles.

The CO_2 gas concentration profile in Figure 4-46 shows a slight decreasing trend in the desorption peak areas for the first 4 cycles. The desorption peak areas then remain stable for the duration of the experiment. It is assumed that the sorbent would then remain stable for any number of cycles after the first $5 - 10$ cycles. The sorbent stability observed in this experiment is attributed to the rapid cycling time attainable with this monolithic adsorber. We have seen in previous experiments, sorbent stability depends on the time duration the sorbent is exposed to elevated temperatures. The radiator construction of the present monolith adsorber is able to uniformly disperse the heat introduced to the sorbent. The stability of the sorbent CO_2 capture capacity can be further enhanced by increasing the gas flow rates into the monolith container. According to the results of this experiment, the rate limiting step for rapid cycling is the gas diffusion through the monolith structure. It follows then, that higher gas flow rates would allow the CO_2 capture cycle times to be shorted. The increase in the gas flow rate should not affect the capture efficiency of the sorbent because with the monolith structure the sorbent is spread over a large area. This allows very close contact between the sorbent and gas. The slow diffusion of the gas through the monolith may also be improved by expanding the space between the fins to allow more room for gas flow. Both approaches to shorten the CO_2 capture cycling time are currently being tested, with a report to follow.

4.10   Technological Development

One key issue to immobilizing the sorbent is the cost of binding approach available.   This section describe a low cost immobilizing approaches for preparation of durable the sorbent particles. The initial sorbent developed was in the form of particle with diameter less 100 μm. These particles are not suitable for practical applications in the fixed bed, fluidized bed, and metal monoliths.   A proper binder was developed to adhere the particles, (ii) shaping them in the pellet form and (ii) on the metal foil.

4.10.1 Sorbent evolution at UAkron

Our sorbent development efforts began in 2001 with preparation of SBA-15, high surface area mesoporous silica, grafted with γ-aminopropyltriethoxysilane (i.e., an aminosilane) and determination of this sorbent structure and CO_2 capture capacity.[60]   SBA-15 provides an excellent thermal stability and aminosilane serve as an effective precursor to graft amine functional group on the solid surface. Although this research has generated extensive interests in CO_2 capture research communities[77], soon we realized the high cost of SBA-15 mesoporous materials will make the aminosilane-grafted SBA-15 sorbent prohibitively expensive for applications in CO_2 capture. We shifted our focus on the use of a low cost silica support and low cost organic amine to serves as the active site for CO_2 adsorption. It is important to point out that the silica-based material serves as an excellent platform for immobilizing an organic amine due to its proper hydrophilicity and acidity/basicity. Oxide supports with high acidity, such as Al_2O_3,[78] strongly bind with amine function groups prohibiting them from binding with CO_2.[54]

We have also found that epoxy is an effective molecule to bind (i.e., immobilize) organic amines on the silica surface as well as between amine molecules. Development of this highly efficient and low cost CO_2 solid amine was derived from a number of key patents and our previous papers, listed in Table 4-11.

Table 4-11. Literatures contributed to our solid amine development

Patents/Papers	Key concepts or Claims	Contribution to our solid amine development
[79] U.S. Pat 5492683, Birbara and Nalette, 1994	Use of porous polymer as a support for amine-polyol	Suggest (i) the use of polymer composite as a support and (ii) the addition of polyol to amine to enhance CO_2 capture
[80] U.S. Pat 6547854B1, Gray et. al, 2003	Contact a base-treated surface a substituted amine containing alkyl and related groups	Both physisorbed and chemisorbed amines on a variety of solid surfaces are able to capture CO_2.
[60] Energy&Fuels, Chuang et. al., 2003	Graft aminosilane on mesoporous materials provides excellent thermal stability.	Grafting provides covalent bonding between amine molecules and mesoporous silica surface. The key issue is the extremely high cost of raw materials
[81] Sirwardane, U.S. Pat 6908497, 2005	Use of solid to support alkyl amine and an ether	Led to the selection of polyethylene glycol to disperse immobilized amines
[82] Gray, et. al., US Pat 7288136B1, 2007	Contact amines with phenol, formaldehyde, acrylonitrile, and combinations	Confirming that immobilization with covalent bonding which is a desired characteristic.
[83] Jones, et. al., US Pat Appl 11/637,477, 2007	A hyperbranched polymer formed from aziridines covalently bonded to surface oxygen of mesoporous silica.	Lead to search for a low cost and low toxicity.
[84] Canadian Pat Appl. 264408, Idem et. al, 2009	Inhibiting O_2- and SO_2- induced liquid amine degradation during CO_2 capture by sodium sulfite, potassium sodium tetrahydrate, EDTA, and NH_2OH	Led to development of Na_2CO_3, $NaHCO_3$, and alkali carbonate as antioxidant to solid amine sorbents.

The evolution of solid amine sorbents at UAkron is showed in flow chart below. The sorbent initially was optimized for high CO_2 capture capacity and further modified for stability. The stability of the sorbent was tested by heating the sorbent in oven at 100 ^{o}C for 18 h and the capture capacity of the sorbent after that was measured. The sorbent which showed better capture capacity and stability with the oven treatment are further optimized by addition of cross linker to immobilize amine on silica and some inorganic species are added to prevent oxidation of amine.

| TEPA/Silica | TS 50/50 3.74 mmol CO_2/g_{sorb} | → Short Cycle Life |

Add Dispersant (PEG) →

| TEPA/PEG/Silica | 10% PEG w/TEPA 2.36 mmol CO_2/g_{sorb} | → Short Cycle Life At Low Loading % |

Adjust Weight Ratios →

| TEPA/PEG/Silica | TPS 30/30/40 2.58 mmol CO_2/g_{sorb} | → Degrades After 3 Cycles Due To TEPA Agglomeration |

Immobilization of Amine Groups →

| TEPA/PEG/Silica -Linker (L_A: Linker molecule) | 0.012 L_A:5 TPS 24/36/40 2.34 mmol CO_2/g_{sorb} | → Maintained Higher Capture After 2 Days of Cycles |

L_A Ratio Optimization →

| TEPA/PEG/Silica-L_A | TPS-$0.09L_A$ 24/36/40-100 2.22 mmol CO_2/g_{sorb} | → Maintained High Capture (>2.00) Over 2 Days of Testing, Degraded On The Third Day Of Testing Due To Oxidation |

Inorganic Species To Help Resist Degradation →

| TEPA/PEG/Silica-L_A-Inorganic Species (I_A, I_B, I_C) | TPS-$0.22L_A$ 24/36/40-100-0.05 I_C 2.14 mmol CO_2/g_{sorb} |

Maintained Stability After Three Days Of Testing

Flow chart showing the evolution of sorbent at UAkron

Figure 4-47 illustrates our most recently developed solid amine preparation steps:

- Preparation of Linker/TEPA/PEG solution,
- Impregnation of the solution prepared onto silica,
- Curing the solid amine with heating treatment at 100 ^{o}C for 5 min, and
- Addition of aqueous inorganic species.

It is important to note that both inorganic speices and PEG play significant roles in inhibiting oxidative degradation. The role of PEG will be further discussed. The specific role of inorganic species is currently under investigation.

Linker exhibits C-H stretching band at 2869-3050 cm^{-1}, the C-H bending and aromatic bands in 1200-1700 cm^{-1}, and a functional group band at 920 cm^{-1}, shown in Figure 4-47(a). TEPA (tetraethylenepentamine) molecule exhibits C-H stretching at 2869-2971 cm^{-1} and NH$_2$ functional group bands at 3296, 3366, and 1601 cm^{-1} in Figure 4-47(b). Claims in a number of patents include polyol and polyethylene glycol (PEG) in solid-supported amine.[79] We found that PEG is the most effective glycols and alcohols in slowing down the degradation of the solid

amine. Our recent infrared and density functional theory studies suggest that PEG disperses the TEPA via the interaction between TEPA's NH_2, and PEG's OH.

It is important to note that the NH_2 functional group has dual functions: (i) serving as CO_2 adsorption sites and (ii) reacting with the epoxide of the Linker molecule to immobilize TEPA. Thermal treatment allows the formation of C-O-C bonding between C in TEPA and O in epoxide of linker as well as the formation of the C-O-Si bond between silica surface OH and C in epoxide of linker. The formation of the C-O-C bond at 1100 cm^{-1} and the disappearance of epoxide at 920 cm^{-1} were observed by infrared spectroscopy, as shown in Figure 4-47(c). One initial concern in the use of epoxide for immobilization is the depletion of TEPA's NH_2. The concern was eliminated by the fact that (i) the immobilized solid amine exhibit a CO_2 capture capacity of more than 2.7 $mmol_{CO2}/g_{sorb.}$ in the absence of H_2O vapor and more than 4.2 $mmol_{CO2}/g_{sorb.}$ in the presence of saturated H_2O vapor and (ii) only one of the amine functional groups in the TEPA molecule reacts with the epoxy functional group of linker, allowing 80% of NH_2 available for CO_2 capture. The broadening of the NH_2 band in TEPA-linker is a result of interaction between OH and NH_2. The OH is produced from the reaction of TEPA's NH_2 with linker's epoxide. The addition of inorganic species resulted in an enhancement of the NH_2 stretching intensity, shown in Figure 4-47(d) and increased the resistance to thermal degradation. The specific interaction between TEPA-linker-PEG and inorganic species remains to be investigated.
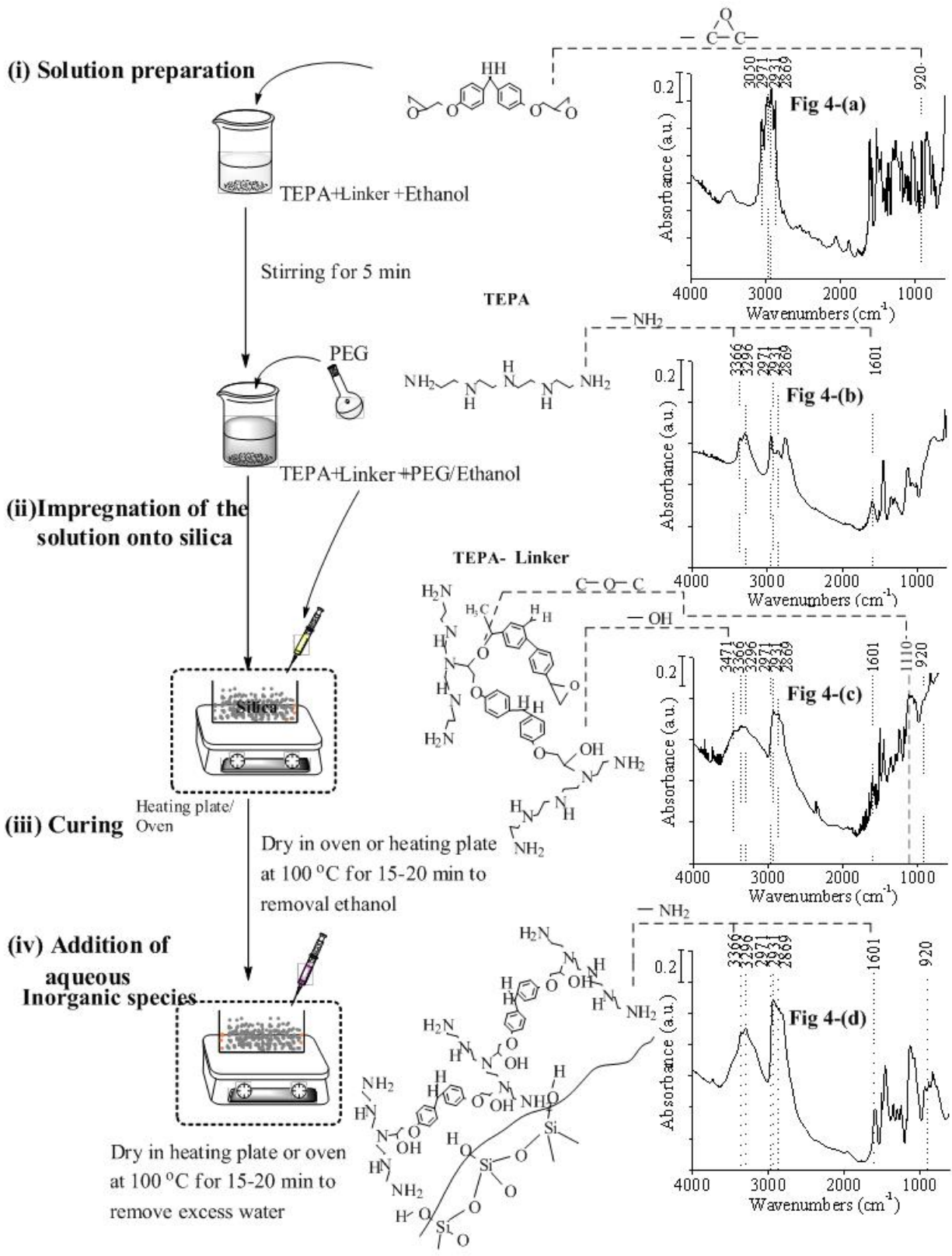
Figure 4-47   Preparation of highly efficient and low cost solid amine

4.10.2 Pellets and Metal monoliths

4.10.2.1   Pelletization and preparation of metal monoliths

CO_2 capture adsorbers use fixed, fluidized or moving bed technologies. The size and shape of the sorbent play an important role to determine the operation conditions of these equipments. Amine immobilized-Silica sorbent (TPSENa) was pelletized using a binder solution. TPSENa has an average particle size of 250µm and a CO_2 capture capacity of 2.6 mmol CO_2/g-sorb. Pellets are rods or spheres with 1 or 2 mm diameter and average CO_2 capture capacity of 2.5 mmol CO_2/g-sorb. After a 48h attrition test, spheres do not lose any appreciable weight and rods lose less than 1% of its initial weight. Pellets were grafted onto metal and stacked together to obtain monolith structures. Metal monoliths have an average CO_2 capture capacity of 1.0 mmol CO_2/g-sorb.

Figure 4-48 shows the preparation procedure for (1) TPSENa sorbent, (2) VTP binder solution, (3) pellets (rods and spheres) and (4) metal monoliths. TPSENa sorbent was prepared by impregnating TEPA, PEG, linker and inorganic species on SiO_2 support. The wet sorbent was dried at 100^oC, grounded and sieved with a 500µm mesh. VTP binder solution was prepared by dissolving binder in water at 100^oC and mixing with TEPA and PEG at room temperature.

Pellets were prepared by mixing equal amounts of TPSENa sorbent and VTP solution, producing a wet paste. The wet paste was extruded in a wet extruder with 1 or 2 mm holes die. The wet extrudate has a shape of long rods. It was dried in oven at 130^oC and cut into pieces to obtain rod pellets. Spherical pellets were obtained by coating the wet extrudate with powder sorbent and treating in spheronizer for 5min. Wet spheres were dried in oven at 130^oC. Few pellets were grounded into powder and compared to TPSENa sorbent.

Metal monoliths were prepared by (i) spreading 1g of a mixture 25% TEPA and 75% linker on 72 cm^2 of aluminum foil, (ii) covering the surface with pellets or wet extrudate and (iii) drying in oven at 130 ^oC. The resulting sheets were stacked or rolled to obtain the monolith structures.

Figure 4-49 (a) shows a schematic of the wet extruder. The wet extruder consists of a cylindrical aluminum vessel and a mobile piston. The vessel has a die with 1 or 2 mm holes to shape the wet paste into long rods (extrudate). A manual ram system provides the pressure for extrusion. A rubber O-ring reduces the clearance between the piston and the vessel to prevent back flow.

Figure 4-49 (b) shows a schematic of the spheronizer. The spheronizer consists of a 19.5cm aluminum drum equipped with a rotary disc. The clearance between the drum and the disk is less than 1mm to avoid losing or breaking pellets. The disc is propelled by a variable-speed electric motor and a funnel is used to feed the extrudate. Spheronization process does not

require cutting the extrudate, but powder sorbent must be used to coat the extrudate and avoid agglomeration.
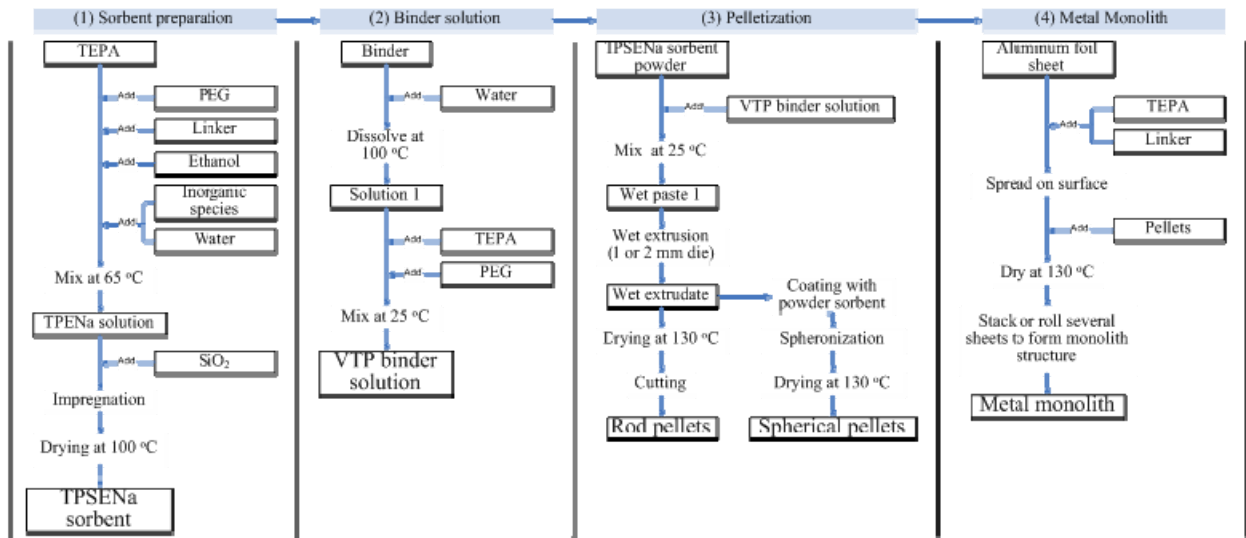
Figure 4-48   Process flow diagram for preparation of (1) TPSENa sorbent, (2) VTP binder solution, (3) pellets and (4) metal monolith structures.
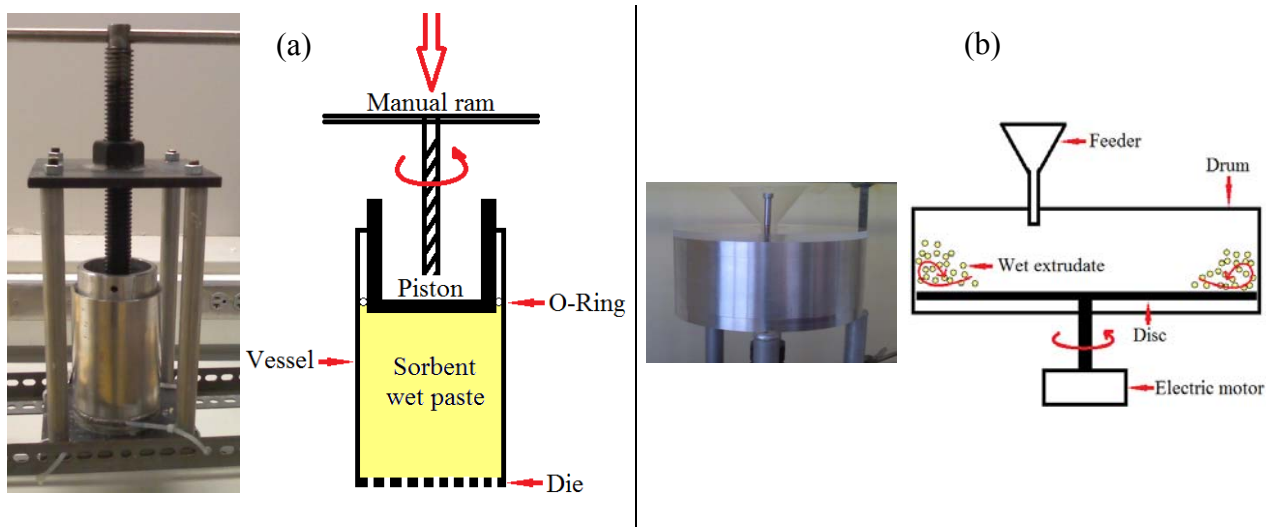
Figure 4-49: Schematic of (a) wet extruder and (b) spheronizer.

4.10.2.2 CO_2 capture capacity, degradation and Fluidization of pellets.

CO_2 capture capacity was measured by weigh method. A 1g sorbent sample was heated to $130^{\circ}C$ and held for 7 min to remove pre-adsorbed CO_2 and H_2O. After desorption, the sorbent at $25^{\circ}C$ was exposed to $50 \text{cm}^3/\text{min}$ of CO_2 for 10min. The CO_2 capture capacity was determined by the weight difference of the sorbent prior and after adsorption of CO_2. This method gives

fairly accurate measure of CO_2 capture capacity, based on the assumption that the sorbent selectively adsorbs CO_2. A degradation study was performed by continuously exposing the sorbent to $130^{\circ}C$ steam. The CO_2 capture capacity was measured every hour.

Figure 4-50 shows the experimental set up for fluidization and attrition test. Pellets were fluidized by flowing air into a 1-inch diameter glass column. The minimum fluidization velocity was determined experimentally for each set of pellets. Attrition test was performed for 48 hours on 5g of pellets by fluidization under air velocity that yields at least 1cm of bed expansion. An attrition element was placed 0.5 cm above the stagnant bed to promote collisions during fluidization. Fluidization column has a fine screen on the top outlet to collect the attrite powder. The weight of pellets and attrite powder was measured before and after the attrition test.
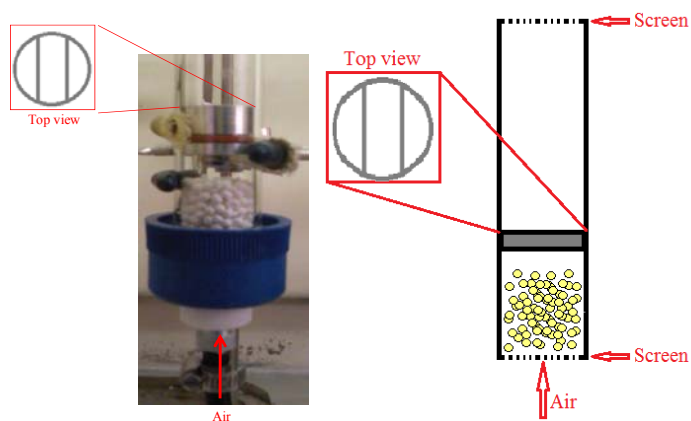
Figure 4-50: Experimental set up for fluidization and attrition test.

4.10.2.3   Results

in the presence of 4% H2O vapor which raised the average CO2 capture capacity of 3.2 mmol/g.

Table 4-12   shows the solid properties and average CO_2 capture capacity for different pellets. Small pellets had initial capture of 2.6 mmol CO_2/g-sorb and degraded 56% of after 18h. Big pellets had initial capture of 2.8 mmol CO_2/g-sorb and degraded 58% after 18 hours. The powder obtained from pellets had an initial CO_2 capture capacity of 2.6 mmol CO_2/g-sorb and presented 58% of degradation after 18 hours. There was no significant difference in CO_2 capture capacity between rods and spheres, showing that the shape has small effect on adsorption capacity. The faster degradation of pellets compared to the powder sorbent may be due to (i) plug of macropores by the binder solution, (2) hot spots into the pellets promoting thermal degradation of NH_2 sites and (3) accumulation of CO_2 on NH_2 sites (auto-poisoning) due to incomplete remotion of adsorbed species.

Figure 4-51 shows the degradation curve for powder, 1 and 2 mm rods. All the sorbents were tested under stagnant conditions; but under fluidization mass and heat transport limitations become unimportant. Without transport limitations the capture capacity of the pellets is expected to be the same as that of the powder sorbent. It is important to point out that the capacity of the sorbent was further enhanced by 40-60 % in the presence of 4% H_2O vapor which raised the average CO2 capture capacity of 3.2 mmol/g.

Table 4-12. Solid properties and CO_2 capture capacity of pellets and powder sorbent.

	Dp (mm)	ρ particle (kg/m^3)	ρ bulk (kg/m^3)	Void fraction	Packing fraction	mmolCO2/g-sorb initial	mmolCO2/g-sorb after 18 h deg.
Small rod	1.2	900	565	0.37	0.63	2.6	1.1
Small sphere	1.2	1630	613	0.62	0.38	2.6	1.1
Big rod	2.5	970	602	0.38	0.62	2.8	1.2
Big sphere	2.5	1610	481	0.70	0.30	2.7	1.2
Powder	0.1		427			2.6	1.3
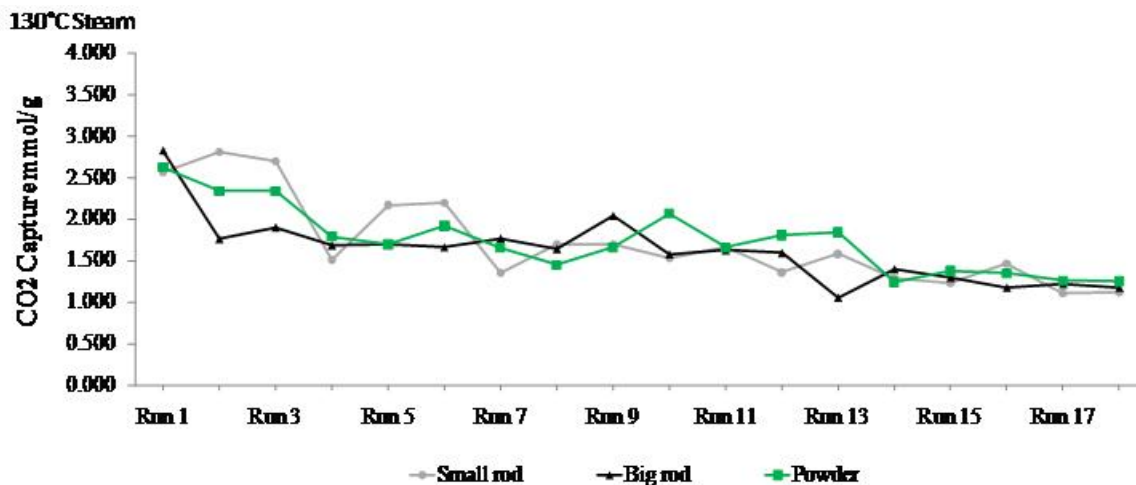
Figure 4-51: Degradation curve for powder, 1 and 2 mm rods under steam at 130°C.

Table 4-13 shows the flow rate, air velocity and estimated weigh loss during the attrition test on pellets. Big particles require higher velocity and flow rate for fluidization and bed expansion than small particles. Air velocity was held constant between sizes to evaluate the effect of the shape on the hardness of the pellet. Spherical pellets presented no evident weight loss after 48h of fluidization. Rods suffered small attrition that represented less than 1% of weight loss. Pellets with rod shape attrite more than spheres because they have sharp edges that are weaker than the plain-like surfaces of the sphere. Also, rods have bigger surface area which

106

increases the probability of collision. Figure 4-52 shows a comparison in shape and size of the pellets.

Figure 4-52 Comparison of size and shape of the pellets.

Table 4-13: Fluidization conditions and attrition test for pellets. Results based on fluidization of 5g of pellets.

	Air flow rate (L/min)	Air velocity (m/s)	Weight loss after 48 h	Experimental min fluid. velocity (m/s)
Small rod	36	1.2	< 50mg	0.56
Small sphere	36	1.2	-	0.56
Big rod	50	1.6	< 50mg	0.76
Big sphere	50	1.6	-	0.76

Figure 4-53 shows the metal monoliths prepared using powder, rods and spheres. Metal monoliths are strong structures because the blend of TEPA(1)/linker(3) crosslinks and yields to a complete cured resin. The crosslink happens at temperature as low as 25°C but is faster at higher temperatures. The average capture capacity of the sorbent in a monolith structure is 1.0 mmol CO_2/g-sorb. Monoliths have low CO_2 capture capacity because about 50% of its surface area is plugged by the TEPA/linker resin. Heat transfer is expected to be faster on this kind of structures.

Powder   1mm rods   1mm spheres   2mm rods
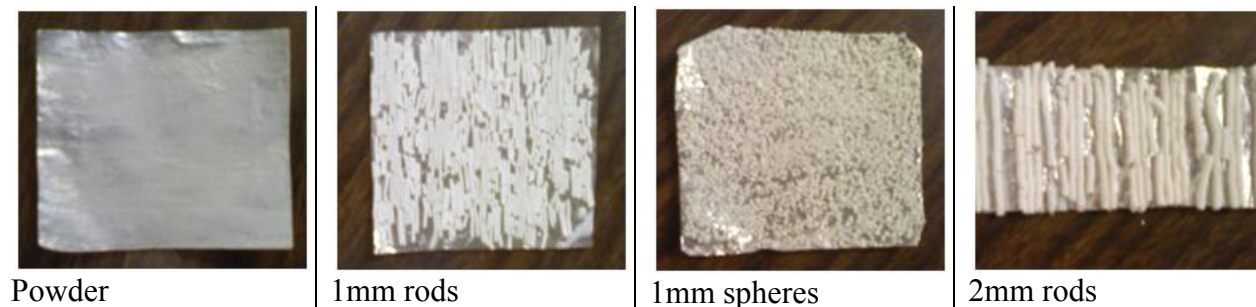
Square structure 2mm rods

Spiral structure 2mm rods

Figure 4-53 Up; sorbent metal sheets prepared with powder, rods and spherical pellets. Down; metal monolith structures prepared from the sorbent metal sheets.

4.10.2.4 Conclusions

Binder in solution is an effective binder agent to agglomerate powder sorbents into strong pellets with CO_2 capture capacity of 2.5 mmol CO_2/g-sorb.   The capacity of the sorbent was further enhanced by 40-60 % in the presence of 4% H_2O vapor which raised the average CO2 capture capacity of **3.2 mmol/g-sorb**.   The water vapor enhancement is ever higher for sorbent in the powder form as described in section 4.7.3. Wet extrusion and spheronization process allow making pellets with different shapes and sizes. Other key findings and achievements are listed below

- CO_2 capture capacity does not strongly depend on the shape of the pellets.
- Big pellets yield to a faster degradation than small pellets and powder.
- Spherical pellets are more resistant to attrition than rod shape pellets.
- Metal monoliths are strong structures, with CO_2 capture capacity of more than 1.0 mmol CO_2/g-sorb.

4.11 Techno-economic assessment of U Akron silica-based solid sorbent for CO_2 capture

DOE.NETL-2009/1336 report entitled, "Existing Plants, Emissions and Capture –Setting CO_2 Program Goal considers of a maximum increase in COE of 35% with a minimum CO_2 captured of 90% as a practical cost goal for CCS (carbon capture and storage) of existing plants. The report provides a preliminary analysis of the cost of the CO_2 capture process based on U Akron solid amine. The results of this study shows that that the overall cost of the solid amine process would be less than 45% of the liquid amine process.

CCS includes CO_2 capture, compression, transport, storage, and monitoring. System analysis have shown that current technologies for CO_2 capture and compression from flue gas impose a severe energy and economic penalty on the cost of electricity (COE) generation that could increase COE by 85% or more. The R&D goal of a maximum increase in COE of 35% with a minimum 90% of CO_2 capture was established for new and existing coal-fired power plant technologies.   This goal can be achieved through improving the efficiency of the CCS technology. A thermodynamic analysis of CO_2 capture from combustion of flue gas of a PC (pulverized coal) plant indicated that the theoretical minimum energy requirements for 90%

separation and compression would result in a 15 % increase in COE. The maximum 35% increase in COE is considered as a practical cost coal.

4.11.1 Base plant

The base plant used for comparison purposes was case 9 and case 10 in "*Cost and Performance Baseline for Fossil Energy Plants—Volume 1: Bituminous Coal and Natural Gas to Electricity" (Aug 2007).* In this report, pulverized coal (PC) plant cases are evaluated with (case 10) and without (case 9) carbon capture and storage (CCS) on a common 550 MWe net basis.

4.11.2 Solid amine CO_2 capture process

Figure 4-54 shows the block flow diagram for the proposed bubbling fluidized bed (BFB) CO_2 capture system. BFB was selected by us and our industrial collaborators for its excellent heat transfer characteristics.   Coal and air enter the boiler to produce steam which is sent to a turbine train to generate electricity. Flue gas exited from the boiler passed through the SCR (selective catalytic reduction for the NO_x removal), particulate filter, and wet limestone desulfurization (FGD) unit. Then, low NOx, particulate, and sulfur flue gas proceeds through a flue gas blower which drives the flue gas into the CO_2 capture unit (see section A in Figure 4-54).   The CO_2 adsorber unit consists of a set of adsorption towers and desorption towers.

The flue gas leaving the CO_2 capture unit must contain more than 95% CO_2. (DE-FOA-0000403, 1/31/2001). It is highly desirable that the composition of this concentrated CO_2 stream meets the specification for CO_2 TS&M (transport, storage, and monitoring): less than 300 ppm N_2, 40 ppm O_2, 10 ppm Ar, and 150 ppm H_2O.   Following CO_2 capture, the CO_2-rich solid amine from the adsorber will be transported, via a conveyor lift or a pneumatic conveyor, to desorption tower where high purity CO2 is produced and the solid amine is regenerated. The high purity CO_2 gas will be drawn off by an induced draft fan and sent to a compressor.   The regenerated solid amine will be cooled and recycled back to the adsorber and the process will be repeated. Process temperature control is critical to adsorbing and releasing CO_2. The optimal adsorption temperature is in the range of 40-57 °C which avoid use of costly heat transfer devices to control the temperature of the inlet to the adsrober unit; the optimal desorption temperature is in the range of 95-105 °C which avoid oxidative degradation of the solid amine and minimize use of excess energy for heating.   The energy required to regenerate the solid amine is less than 285 kJ/kg CO_2 on the basis of a sorbent with a 0.14 kg CO_2/1 kg (3.2 mole CO/kg sorbent) sorbent capture capacity. The heat transfer for the sorbent regeneration will be achieved by passing steam through a series of in-bed heat exchangers in the lower BFB section of the desorption tower. Material and energy flows in the proposed process are labeled on Figure 4-54.
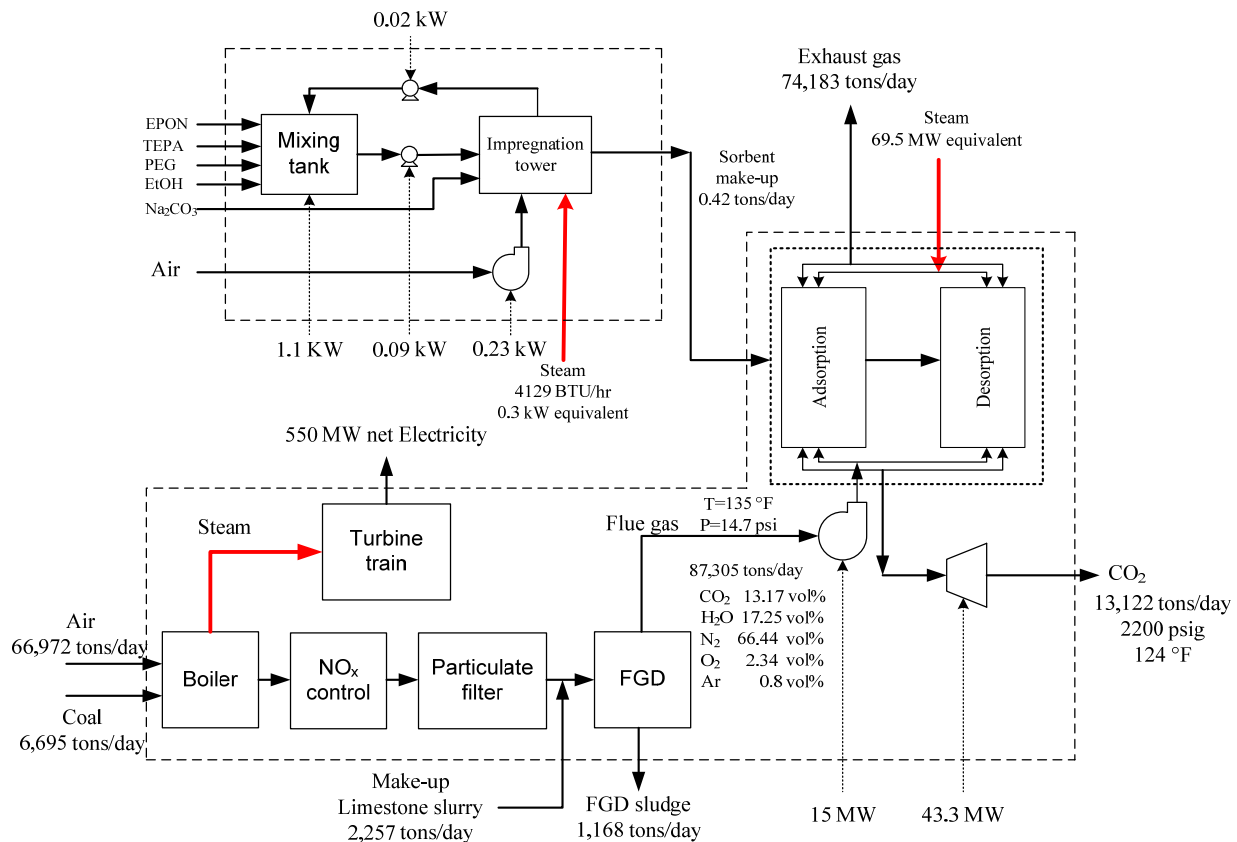
Figure 4-54   550 MW pulverized coal (PC) plant with solid sorbent CO_2 Capture Unit (74,183 tons/day of flue gas and 13,122 tons/day CO_2 for compression)

4.11.3 Methodologies

4.11.3.1   Initial sorbent charge and make up rate

The design and performance of the adsorption/desorption unit in Figure 4-54 is based on the lab scale data and our industrial partner's knowledge of the performance of bubbling fluid beds (BFB) operation using solid sorbent.   It is assumed that the bed is initially charged with 426 tons of fresh sorbent having an average of 3.2 mol CO_2/kg sorbent capturing capacity. This amount of sorbent undergoes 220 adsorption/desorption cycles every day (6.5 minutes for each cycle).   It is assumed that 0.1% of the solid sorbents need to be replaced every day due to attrition and sorbent degradation loss that accounts for 0.42 tons of sorbent make-up per day.

4.11.3.2   Regeneration heat duty

The energy required to release the CO_2 from the solid amine in the desorber is approximately 757.6 BTU/lb CO_2 (i.e., 1760.7 kJ/kg CO_2).   Detail calculations are presented in box 1. 43.3 MW is needed to regenerate the solid amine sorbent for the proposed 550 MW plant. This amount of energy is less than 45% of those for the liquid amine processes.

Box 1sorbent regeneration heat duty calculation

Sorbent regeneration heat duty calculation

$$Q_r = \Delta H_r + \left(mC_p\Delta T\right)_{CO_2} + \left(mC_p\Delta T\right)_{Sorbent}$$

ΔH_r	Heat of regeneration reaction	

Regeneration heating cycle:

T1	**50** C	
T2	**100** C	
ΔT	50 C	

ΔH_r=	**52** kJ/mol CO_2	=	1181.82 kJ/kg CO_2

$C_p(CO_2)$	0.8640 kJ/K/kg
$C_p(sorbent)$	1.50 kJ/K/kg

Calculation basis: **1** kg of sorbent

Captured CO_2 by 1 kg of sorbent =	0.14 kg CO_2/kg sorbent

Heat of regeneration	165.45 kJ/kg sorbent
CO_2 $\boxed{mC_p\Delta T}$	6.05 kJ/kg sorbent
Sorbent $\boxed{mC_p\Delta T}$	75.00 kJ/kg sorbent

Heat requirement based on captured CO_2=	**1760.7 kJ/kg CO_2**	=	**757.6 BTU/lb CO_2**

4.11.3.3   Capital cost estimation

Direct cost are the capital and operating cost associated with each step of the CCS.; the indirect cost include costs associated with the modification of the existing processes at the plants, including the energy penalty cost. In this report, the required capital for building a PC plant with solid amine sorbent CO_2 capture system is estimated by comparing the equipment prices for such plant and an existing pulverized coal (PC) plant that employ other CO_2 capture technologies. To achieve this, case 10 in "*Cost and Performance Baseline for Fossil Energy Plants—Volume 1: Bituminous Coal and Natural Gas to Electricity*" *(Aug 2007)* was used in the analysis as another data point to scale costs. The variation in capital cost, material flow rates, and auxiliary power of common equipment was assumed to be linear between different sizes of power plants, where appropriate. The linear assumption was proposed by our industrial partner on the basis of their experience. The capture system capital cost was based on costs for equipment similar to the equipment being used in this process. The similar equipment was from a 515 MW plant which is based on previous study performed by our industrial partner so that the costs were escalated to a 550 MW plant. The CPI index was used to convert the equipment cost from Jan 2011 dollars back to Dec 2006 dollars. Finally, process and project contingencies were added to the cost using the same ratio as the liquid amine system from Case 10. The auxiliary power for the capture system was estimated on the basis of the auxiliary power for the liquid amine system from Case 10 using a ratio of the regeneration energy between the solid amine and the liquid amine. Estimates were made for the cost of the solid amine and the attrition rate. The initial

charge of solid amine was included in the capital cost and the makeup cost for the solid amine was included in the variable O&M costs.

The compression system used after the solid amine CO_2 capture system will be similar to that used for liquid amine systems. Therefore, the capital cost and auxiliary power values for the compression system from Case 10 were used in this techno-economic analysis. Table 4-14 indicated that the capital cost for the solid amine is expected be less than 50% of liquid amine (Case 10) because (i) the absence of corrosion issues allows the use of low cost of steel, (ii) the use of blower decreases the cost as compared with the use of pump to transport the liquid amine between absorption and desorption tower, and (iii) further saving from the packing materials for the adsorption tower. Analysis in Table 4-16 shows that the capital and fuel cost is less than 45% of the liquid amine. The use of low quality steam with proper heat integration could further decrease the cost of the solid amine process.

4.11.4 Conclusions

Our preliminary economic analysis indicated that the overall cost of the solid amine process would be less than 45% of the liquid amine process. Further cost reduction to 35% increase in COE requires the improvement of the efficiency of compression.

Table 4-14. Capitals cost breakdown for base cases (case 9 and 10) and proposed solid amine process.

Item/Description	Total Plant Cost ($/kW)*			Incremental Increase in Cost of Electricity (mills/kWh)*		
	Base Case (Case 9)	Base Case w/ Capture (Case 10)	Solid Amine	Base Case (Case 9)	Base Case w/ Capture (Case 10)	Solid Amine
Utility Costs (UC)						
Coal Handling	69	88	83	1.51	2.06	1.96
Coal Prep & Feed	32	42	40	0.71	0.98	0.93
Feed water & Misc. BOP Sys.	128	183	170	2.82	4.29	3.99
Boiler (incl. NOx Control)	461	606	572	10.16	14.23	13.44
Flue Gas Cleanup (PM & SO$_x$)	246	323	305	5.42	7.58	7.16
Total UC	936	1242	1170	20.62	29.14	27.48
Carbon Dioxide Recovery (CDR)						
CO$_2$ Capture System		792	468		18.59	8.00
CO$_2$ Compression System		89	89		2.09	2.09

Total CDR Cost		881	558		20.69	10.09
Equipment and Handling Costs (EH)						
Ducting & Stack	68	76	74	1.50	1.77	1.73
Steam Turbine Generator	197	228	221	4.34	5.35	5.18
Cooling Water System	68	119	107	1.49	2.80	2.52
Ash Handling	23	28	27	0.50	0.66	0.63
Accessory Electric Plant	88	139	127	1.94	3.26	2.99
Instrumentation & Control	37	44	42	0.81	1.03	0.99
Site Improvements	24	28	27	0.54	0.65	0.63
Buildings & Structures	108	111	110	2.38	2.61	2.59
Total EH Cost	613	773	735	13.5	18.13	17.26
Total Plant Capital Cost	$ 1,550	$ 2,896	$ 2,463	34*	68*	55*

* These incremental increases in the COE are also found in the first row of Table 4-16.

Table 4-15. Carbon capture and storage (CCS) specific costs.

CCS Specific Costs	Base Case w/ Capture (Case 10)		Solid Amine	
	Incremental COE (mills/kWh)	Percent of Total	Incremental COE (mills/kWh)	Percent of Total
CCS Direct Costs				
Total CO_2 TSM Direct	2.9	5.3%	3.1	8.3%
In Plant Direct Costs				
CO_2 Capture Direct Capital	12.6	22.9%	8.0	21.4%
CO_2 Compression Direct Capital	1.4	2.6%	1.5	4.0%
Direct Fixed Operating	1.4	2.5%	1.0	2.7%
Direct Variable Operating	3.5	6.3%	2.6	7.0%
Total In-Plant Direct	18.9	34.3%	13.2	35.1%
Total CCS Direct Costs	21.8	39.6%	16.2	43.4%
CCS Indirect Costs				
Make-Up Power	33.2	60.4%	21.1	56.6%
Total CCS Indirect Costs	33.2	60.4%	21.1	56.6%
Total CCS Costs	55.0	100%	37.4	100%

Table 4-16. Cost of Electricity breakdown.

Cost of Electricity (COE) (mills/kWh)*		Base Case (Case 9)	Base Case w/ Capture (Case 10)	Solid Amine
Total Plant Capital Cost	CO_2 Capture System		18.59[*]	8.00[*]
	Other Plant Capital Costs	34.1	49.41	47.0
Operating	Fixed Operating	3.9	5.9	5.2
	Variable Operating	5.9	11.0	9.4
Fuel	CO_2 Regeneration		6.4	3.8
	CO_2 compression		3.3	3.3
	Electricity generators	20.2	20.2	20.2
CO_2 TSM		0	4.3	4.3
Total (mills/kWh)		64	119	101.2
Percent Increase in COE		-	86%	58%

* Capital costs associated with CO_2 capture systems only. Refer to Table 4-14 for the other plant capital costs. Table 4-16 shows the comparison between the proposed solid amine sorbent CO_2 capture process, MEA process, and base case without CO_2 capture technology. The proposed CO_2 capture process by solid amine sorbents would result in a 58% increase in COE as compared to the 86% increase caused by the MEA process. Further analysis of the capturing processes reveal that proposed solid amine process has a significantly lower capital and fuel costs. The lower costs can be attributed to the regeneration energy needed for the solid amine sorbent and low capital cost.

4.12   Conclusions

The solid amine sorbent for CO_2 capture process possesses advantages of simplicity and low operating cost compares to MEA process. The reported solid amine sorbent suffered from low CO_2 capture capacity and stability.   This project involves (i) investigation of the interaction between CO_2 and amine functional groups of the solid amine sorbents, (ii) fabrication of high performance solid amine sorbent pellets and metal monoliths, (iii) evaluation of the solid amine sorbent in fixed, fluidized bed, and metal monoliths units, and (iv) preliminary economic analysis of the solid amine process.

The results of this study led to the development of a high performance solid amine sorbent under simulated gas flow condition in a fixed bed, a fluidized bed, and a metal monolith unit. This study showed heat transfer could become a major technical issue in scaling up a fixed bed adsorber. The use of the fluidized bed and metal monoliths can alleviate the heat transfer issue. The metal monolith could be suitable for small scale applications due to the high cost of manufacturing; the fluidized bed mode would be most suitable for large scale applications. Preliminary economic analysis suggested that the Akron solid amine process would cost 45% less than that of MEA process.

References

(1)   Khatri, R. A.; Chuang, S. S. C.; Soong, Y.; Gray, M. *Industrial & Engineering Chemistry Research* 2005, *44*, 3702.

(2)   Khatri, R. A.; Chuang, S. S. C.; Soong, Y.; Gray, M. *Energy & Fuels* 2006, *20*, 1514.

(3)   Skoog, D. A.; Holler, F. J.; Crouch, S. R. *Principles of Instrumental Analysis*; 6th ed.; Thomson Brooks/Cole: Belmont, 2007.

(4)   Colthup, N. B.; Daly, L. H.; Wiberley, S. E. *Introduction to Infrared and Raman Spectroscopy*; 2nd ed.; Academic Press: New York, 1975.

(5)   Battjes, K. P.; Barolo, A. M.; Dreyfuss, P. *Journal of Adhesion Science and Technology* 1991, *5*, 785.

(6)   Hiyoshi, N.; Yogo, K.; Yashima, T. *Microporous and Mesoporous Materials* 2005, *84*, 357.

(7)   Baisch, U.; Dell'Amico, D. B.; Calderazzo, F.; Labella, L.; Marchetti, F.; Merigo, A. *European Journal of Inorganic Chemistry* 2004, 1219.

(8)   Aresta, M.; Quaranta, E. *Tetrahedron* 1992, *48*, 1515.

(9)   Chisholm, M. H.; Extine, M. W. *Journal of the American Chemical Society* 1977, *99*, 792.

(10)   Little, L. H. *Infrared Spectra of Adsorbed Species*; Academic Press: London, 1966.

(11)   Kazarian, S. G.; Vincent, M. F.; Bright, F. V.; Liotta, C. L.; Eckert, C. A. *J. Am. Chem. Soc.* 1996, *118*, 1729.

(12)   Moroi, Y.; Motomura, K.; Matuura, R. *Bulletin of the Chemical Society of Japan* 1972, *45*, 2697.

(13)   Huang, H. Y.; Yang, R. T.; Chinn, D.; Munson, C. L. *Industrial & Engineering Chemistry Research* 2003, *42*, 2427.

(14)   Yoshitake, H.; Koiso, E.; Horie, H.; Yoshimura, H. *Microporous and Mesoporous Materials* 2005, *85*, 183.

(15)   You, J. K.; Park, H.; Yang, S. H.; Hong, W. H.; Shin, W.; Kang, J. K.; Yi, K. B.; Kim, J.-N. *Journal of Physical Chemistry B* 2008, *112*, 4323.

(16)   Yue, M. B.; Chun, Y.; Cao, Y.; Dong, X.; Zhu, J. H. *Advanced Functional Materials* 2006, *16*, 1717.

(17)   Powell, C. E.; Qiao, G. G. *Journal of Membrane Science* 2006, *279*, 1.

(18)   Ma, X.; Song, C. Preprints - American Chemical Society, Division of Petroleum Chemistry 2006, 51, 100.

(19)   Sass, B.; Monzyk, B.; Ricci, S.; Gupta, A.; Hindin, B.; Gupta, N. Carbon Dioxide Capture for Storage in Deep Geologic Formations--Results from the CO2 Capture Project 2005, 2, 955.

(20)   Hiyoshi, N.; Yogo, K.; Yashima, T. *Chemistry Letters* 2004, *33*, 510.

(21)   Zheng, F.; Tran, D. N.; Busche, B. J.; Fryxell, G. E.; Addleman, R. S.; Zemanian, T. S.; Aardahl, C. L. *Industrial & Engineering Chemistry Research* 2005, *44*, 3099.

(22)   Arenillas, A.; Smith, K. M.; Drage, T. C.; Snape, C. E. *Fuel* 2005, *84*, 2204.

(23)   Chen, B.; Chuang, S. S. C. *Green Chemistry* 2003, *5*, 484.

(24)   Kim, C. J.; Savage, D. W. *Chemical Engineering Science* 1987, *42*, 1481.

(25)   Agnew, J.; Hampartsoumian, E.; Jones, J. M.; Nimmo, W. *Journal of the Energy Institute* 2005, *78*, 81.

(26)   Garcia, B.; Takarada, T. *Fuel* 1999, *78*, 573.

(27)   Konttinen, J. T.; Zevenhoven, C. A. P.; Hupa, M. M. *Industrial & Engineering Chemistry Research* 1997, *36*, 2340.

(28)   Maes, I. I.; Gryglewicz, G.; Yperman, J.; Franco, D. V.; D'Haes, J.; D'Olieslaeger, M.; Van Poucke, L. C. *Fuel* 2000, *79*, 1873.

(29)   Wang, X.; Jia, J.; Zhao, L.; Sun, T. *Applied Surface Science* 2008, *254*, 5445.

(30)   Yrjas, P.; Iisa, K.; Hupa, M. *Fuel* 1996, *75*, 89.

(31)   Wang, X.; Ma, X.; Sun, L.; Song, C. *Green Chemistry* 2007, *9*, 695.

(32)   Yang, J.; Zhou, Y.; Wang, H. J.; Zhuang, T. T.; Cao, Y.; Yun, Z. Y.; Yu, Q.; Zhu, J. H. *Journal of Physical Chemistry C* 2008, *112*, 6740.

(33)   Yun, Z.-Y.; Xu, Y.; Xu, J.-H.; Wu, Z.-Y.; Wei, Y.-L.; Zhou, Z.-P.; Zhu, J. H. *Microporous and Mesoporous Materials* 2004, *72*, 127.

(34)   Tuazon, E. C.; Winer, A. M.; Graham, R. A.; Schmid, J. P.; Pitts, J. N., Jr. *Environmental Science & Technology* 1978, *12*, 954.

(35)   Hadjiivanov, K. I. Catalysis Reviews - Science and Engineering 2000, 42, 71.

(36)   Wang, J.; Koel, B. E. *Surface Science* 1999, *436*, 15.

(37)   Nakamoto, K. IR and RAMAN Spectra of Inorganic and Coordination Complexes; Wiley: New York, 1985.

(38)   Nakamoto, K. IR and RAMAN Spectra of Inorganic and Coordinated Complexes, Part A: Theory and Applications in Inorganic Chemistry; 5th ed.; Wiley: New York, 1997.

(39)   Sakaki, S.; Sato, H.; Imai, Y.; Morokuma, K.; Ohkubo, K. *Inorganic Chemistry* 1985, *24*, 4538.

(40)   Davydov, A. Molecular Spectroscopy of Oxide Catalyst Surfaces; Wiley: Sussex, 2003.

(41)   Goodman, A. L.; Li, P.; Usher, C. R.; Grassian, V. H. *Journal of Physical Chemistry A* 2001, *105*, 6109.

(42)   Usher, C. R.; Al-Hosney, H.; Carlos-Cuellar, S.; Grassian, V. H. *J. Geophys. Res., [Atmos.]* 2002, *107*, ACH16/1.

(43)   Isaev, R. N.; Ishkov, A. V. Journal of Analytical Chemistry (Translation of Zhurnal Analiticheskoi Khimii) 2002, 57, 794.

(44)   Lunvongsa, S.; Takayanagi, T.; Oshima, M.; Motomizu, S. *Analytica Chimica Acta* 2006, *576*, 261.

(45)   Li, X.-G.; Duan, W.; Huang, M.-R.; Yang, Y.-L.; Zhao, D.-Y.; Dong, Q.-Z. *Polymer* 2003, *44*, 5579.

(46)   Wade, L. G. *Organic Chemistry*; 4th ed.; Prentice Hall: New Jersey, 1999.

(47)   Sirita, J.; Phanichphant, S.; Meunier, F. C. *Analytical Chemistry (Washington, DC, United States)* 2007, *79*, 3912.

(48)   Sakata, T.; Okai, T.; Sugimoto, H.; Tsubomura, H. *Bulletin of the Chemical Society of Japan* 1975, *48*, 2945.

(49)   Oelkrug, D.; Uhl, S.; Gregor, M.; Lege, R.; Kelly, G.; Wilkinson, F. *Journal of Molecular Structure* 1990, *218*, 435.

(50)   Choudhary, V. R.; Mantri, K. *Langmuir* 2000, *16*, 7031.

(51)   Hair, M. L. Infrared Spectroscopy in Surface Chemistry, 1967.

(52)   Knofel, C.; Martin, C.; Hornebecq, V.; Llewellyn, P. L. *Journal of Physical Chemistry C* 2009, *113*, 21726.

(53)   Wang, X.; Schwartz, V.; Clark, J. C.; Ma, X.; Overbury, S. H.; Xu, X.; Song, C. *Journal of Physical Chemistry C* 2009, *113*, 7260.

(54)   Fisher, J. C., II; Tanthana, J.; Chuang, S. S. C. *Environmental Progress & Sustainable Energy* 2009, *28*, 589.

(55)   Lee, S. C.; Chae, H. J.; Lee, S. J.; Choi, B. Y.; Yi, C. K.; Lee, J. B.; Ryu, C. K.; Kim, J. C. *Environmental Science and Technology* 2008, *42*, 2736.

(56)   Li, P.; Ge, B.; Zhang, S.; Chen, S.; Zhang, Q.; Zhao, Y. *Langmuir* 2008, *24*, 6567.

(57)   Singh, P.; Niederer, J. P. M.; Versteeg, G. F. *International Journal of Greenhouse Gas Control* 2007, *1*, 5.

(58)   Li, P.; Zhang, S.; Chen, S.; Zhang, Q.; Pan, J.; Ge, B. *Journal of Applied Polymer Science* 2008, *108*, 3851.

(59)   Pokrovski, K.; Jung, K. T.; Bell, A. T. *Langmuir* 2001, *17*, 4297.

(60)   Chang, A. C. C.; Chuang, S. S. C.; Gray, M.; Soong, Y. *Energy & Fuels* 2003, *17*, 468.

(61)   Guzman, F.; Chuang, S. S. C. *J. Am. Chem. Soc.* 2010, *132*, 1502.

(62)   Bossa, J.-B.; Borget, F.; Duvernay, F.; Theule, P.; Chiavassa, T. *Journal of Physical Chemistry A* 2008, *112*, 5113.

(63)   Khanna, R. K.; Moore, M. H. Spectrochimica Acta, Part A: Molecular and Biomolecular Spectroscopy 1999, 55A, 961.

(64)   Jackson, P.; Robinson, K.; Puxty, G.; Attalla, M. *Energy Procedia* 2009, *1*, 985.

(65)   Coleman, M. M.; Lee, K. H.; Skrovanek, D. J.; Painter, P. C. *Macromolecules* 1986, *19*, 2149.

(66)   Tanthana, J.; Chuang, S. S. C. *ChemSusChem* 2010, *3*, 957.

(67)   Clayden, J.; Greeves, N.; Warren, S. *Organic Chemistry*; 1 ed.; Oxford University Press, 2005.

(68)   Lide, D. R., ed. *CRC Handbook of Chemistry and Physics*; 86 ed.; CRC Press LLC 2005: Boca Raton, FL, 2005.

(69)   Silverstein, M. R.; Webster, X. F.; Kiemle, J. D. *Spectrometric Identification of Organic Compounds*; 7 ed.; John Wiley & Sons, Inc., 2005.

(70)   Wade, L. G. Organic Chemistry, 4th Edition, 1998.

(71)   McMurry, J. *Organic Chemistry*; 5 ed.; Brooks/Cole, 2000.

(72)   Shimizu, I.; Okabayashi, H.; Taga, K.; Nishio, E.; O'Connor, C. J. *Vibrational Spectroscopy* 1997, *14*, 113.

(73)   Rostovshchikova, T.; Smirnov, V.; Kiseleva, O.; Yushcenko, V.; Tzodikov, M.; Maksimov, Y.; Suzdalev, I.; Kustov, L.; Tkachenko, O. *Catalysis Today* 2010, *152*, 48.

(74)   Trunschke, A.; Hunger, B. *Topics in Catalysis* 2002, *19*, 215.

(75)   Li, Y.; Xiao, F.; Wong, C. P. Journal of Polymer Science, Part A: Polymer Chemistry 2006, 45, 181.

(76)   Shang, H.; Ouyang, T.; Yang, F.; Kou, Y. *Environmental Science and Technology* 2003, *37*, 2596.

(77)   Choi, S.; Drese, J. H.; Jones, C. W. *ChemSusChem* 2009, *2*, 796.

(78)   Refczynska, M.; Skompska, M. *Journal of Physics: Conference Series* 2009, *146*, No pp given.

(79)   Birbara, P. J.; Nalette, T. A.; (United Technologies Corp., USA). Application: WO
WO, 1994, p 25 pp.

(80)   Gray, M. L.; Soong, Y.; Champagne, K. J.; (The United States of America as Represented by the United States Department of Energy, USA). Application: US
US, 2003, p 10 pp.

(81)   Sirwardane, R. V.; (The United States of America as Represented by the Department of Energy, USA). Application: US
US, 2005, p 17 pp.

(82)   Gray; McMahan L., C. K. J., Soong; Yee, Filburn; Thomas; Patent, U. S., Ed. USA, 2005; Vol. 7,288,136.

(83)   Jones, C. W.; Hicks, J. C.; Fauth, D. J.; Gray, M.; (Georgia Tech Research Corp., USA). Application: US
US, 2007, p 17 pp.

(84)   Idem, R.; Supap, T.; Tontiwachwuthikul, P.; Saiwan, C.; Pitipuech, P.; (The University of Regina, Can.). Application: CA
CA, 2009, p 41pp.